This is the peer-reviewed, final accepted version for American Mineralogist, published by the Mineralogical Society of America.
The published version is subject to change. Cite as Authors (Year) Title. American Mineralogist, in press.
DOI: https://doi.org/10.2138/am-2021-7934. http://www.minsocam.org/

Revision 1, 2-2021

Immiscible metallic melts in the upper mantle beneath Mount Carmel, Israel: Silicides, phosphides and carbides

William L. Griffin[1], Sarah E.M. Gain[1,2], Martin J. Saunders[2], Jin-Xiang Huang[1], Olivier Alard[1], Vered Toledo[3] and Suzanne Y. O'Reilly[1]

[1]*ARC Centre of Excellence for Core to Crust Fluid Systems (CCFS) and GEMOC, Earth and Environmental Sciences, Macquarie University, NSW 2109, Australia; bill.griffin@mq.edu.au*

[2] *Centre for Microscopy, Characterisation and Analysis, The University of Western Australia, WA 6009, Australia*

[3]*Shefa Gems Ltd., Netanya 4210602, Israel*

Abstract

Xenolithic corundum aggregates in Cretaceous mafic pyroclastics from Mount Carmel contain pockets of silicate melts with mineral assemblages (SiC (moissanite), TiC, Ti_2O_3 (tistarite), Fe-Ti-Zr silicides/phosphides) indicative of magmatic temperatures and oxygen fugacity (fO_2) at least 6 log units below the Iron-Wüstite buffer (ΔIW≤-6). Microstructural evidence indicates that immiscible, carbon-rich metallic (Fe-Ti-Zr-Si-P) melts separated during the crystallization of the silicate melts. The further evolution of these metallic melts was driven by the crystallization of two main ternary phases (FeTiSi and $FeTiSi_2$) and several near-binary phases, as well as the separation of more evolved immiscible melts.

Reconstructed melt compositions fall close to cotectic curves in the Fe-Ti-Si system, consistent with trapping as metallic liquids. Temperatures estimated from comparisons with experimental work range from ≥1500 °C to ca 1150 °C; these probably are maximum values, due to the solution of C, H, P and Zr. With decreasing temperature (*T*), the Si, Fe and P contents of the Fe-Ti-Si melts increased, while contents of Ti and C decreased. The increase in Si with declining *T* implies a corresponding decrease in fO_2, probably to *ca* ΔIW-9. The solubility of P in the metallic melts declined with *T* and fO_2, leading to immiscibility between Fe-Ti-Si melts and (Ti,Zr)-(P,Si) melts. Decreasing *T* and fO_2 also reduced the solubility of C in the liquid metal, driving the continuous crystallization of TiC and SiC during cooling. The lower-T metallic melts are richer in Cr, and to some extent V, as predicted by experimental studies showing that Cr and V become more siderophile with decreasing fO_2.

These observations emphasise the importance of melt-melt immiscibility for the evolution of magmas under reducing conditions. The low fO_2 and the abundance of carbon

in the Mt Carmel system are consistent with a model in which differentiating melts were fluxed by fluids that were dominated by CH_4+H_2, probably derived from a metal-saturated sublithospheric mantle. A compilation of other occurrences suggests that these phenomena may commonly accompany several types of explosive volcanism.

Keywords: Mt Carmel, oxygen fugacity, metallic melts, immiscibility, mantle methane

Introduction

The oxygen fugacity (fO_2) of Earth's lithospheric mantle typically lies within the range defined by the QFM (quartz-fayalite-magnetite) and IW (iron-wüstite) buffer reactions, and broadly decreases relative to these buffers with depth (Frost and McCammon, 2008; Yaxley et al., 2012). There are indications that the sublithospheric upper mantle, and the lower mantle, are saturated in Fe metal or Fe-Ni-S melts, constraining fO_2 to near the IW buffer (Frost and McCammon, 2008; Zhang et al., 2016). However, there also is evidence that some volumes of the upper mantle have experienced much more reducing conditions, defined by minerals such as moissanite (SiC), which commonly occurs in kimberlites (Huang et al., 2020; Shiryaev et al., 2011) and requires fO_2 at least 6 log units below the IW buffer (ΔIW-6) at lithospheric pressure (P) and temperature (T) (Ulmer et al., 1998). Another example is the super-reduced mineral association (native elements, carbides, silicides) described from chromitites and peridotites in the ophiolites of the Yarlung-Zangbo suture of southern Tibet, and similar bodies in the Polar Urals (Griffin et al., 2016b; Yang et al., 2015). Others include unusual basalt-borne xenoliths (Liu et al., 2015) and a possibly kimberlitic beach pebble (Di Pierro et al., 2003) whose origins are unclear.

These occurrences raise the question of how such reduced conditions could be imposed, at least locally, on the more oxidized upper mantle, and how the resulting mineral assemblages could be preserved from oxidation through reaction with the surrounding mantle (Schmidt et al., 2014). Unfortunately, most of the ophiolitic and kimberlitic occurrences are known from mineral separates, which provide little context for understanding processes (Pujol-Solà et al., 2018; Zhang et al., 2016). However, similar mineral associations have been recognized in melt pockets trapped in xenolithic corundum aggregates in Cretaceous mafic pyroclastic deposits from the Mount Carmel area of northern Israel (Fig. SD1; Griffin et al., 2018d; Xiong et al., 2017). This remarkable

occurrence provides new insights into the localized development of super-reducing conditions within the upper mantle or lower crust, with implications for the nature of mantle-derived C-O-H fluids and their significance in magmatic processes.

Over the last decade, the Shefa Yamim Ltd (now Shefa Gems Ltd) exploration project, focused on placer gem deposits, has recovered abundant xenocrysts of corundum as single crystals (sapphire, ruby) and as aggregates of skeletal and hopper-shapped crystals of corundum (trademarked as "Carmel Sapphire") as well as moissanite (SiC) from pyroclastic vents and tuffs on Mt Carmel (primarily the Rakefet Magmatic Complex; Fig. SD1), and related alluvial deposits (Griffin et al., 2018d; Toledo et al., 2015; Xiong et al., 2017). Crystals of moissanite can be over 4 mm long; sapphire crystals are up to 2 cm (5.7 carats), while ruby crystals are typically smaller, but may contain up to >35 wt% Cr_2O_3 (Griffin et al., 2021). Pieces of "Carmel Sapphire" up to 12.2 carats in weight (ca 18 x 10 mm) have been available for this study, and stones of >33 cts have been recovered.

The mineral parageneses of the melts trapped in the corundum aggregates are complex; over 130 phases have been identified, of which ca 50% are previously unreported; others are until now known only from meteorites (Bindi et al., 2019; Griffin et al., 2019a; Griffin et al., 2020a; Griffin et al., 2020b; Griffin et al., 2018c; Griffin et al., 2018d; Huang et al., 2020). This paper discusses another important aspect of the Mount Carmel corundum-moissanite association: the separation and evolution of immiscible, carbon-rich Fe-Ti-Zr-Si-P melts during the crystallization of the silicate melts. Our aim is to document these parageneses, and to compare the phase relationships among the melts and their crystallization products with data from experimental metallurgy, to constrain the conditions prevailing within the magmatic system prior to eruption.

Geological setting

The material described here is derived from Cretaceous volcanic centers and related alluvial deposits in the Mt Carmel-Kishon River area of northern Israel (southern Galilee; Fig. SD1). This region experienced mafic volcanism during and following the Permo-Triassic rifting related to the opening of the Neo-Tethys ocean (Segev and Rybakov, 2011). Geophysical anomalies and the distribution of zircon xenocrysts in the Cretaceous pyroclastic deposits suggest the existence of a large volume of mafic rocks buried beneath

Mt Carmel, perhaps near the crust-mantle boundary (Ben-Avraham and Hall, 1977; Griffin et al., 2018c; Gvirtzman et al., 1990).

The relatively sparse Early Cretaceous continental magmatism in Israel (137-139 Ma; Segev, 2005, and references therein) comprises subalkaline to alkaline basalts, nephelinites, basanites, picrites and microgabbros with hotspot/mantle plume geochemical and isotopic signatures (Garfunkel, 1989; Laws and Wilson, 1997; Stein and Hofmann, 1992; Stein and Hofmann, 1994).

The Late Cretaceous (94-98 Ma, Turonian-Cenomanian) volcanic activity in northern Israel took place across a heavily faulted area of ca 150 km^2 in the Mount Carmel-Umm El Fahm area (Fig. SD-1b), and produced pyroclastic deposits of mafic to ultramafic composition in vents and layered deposits (Sass, 1980). The explosive volcanism took place in a shallow marine environment, during the deposition of marine carbonates and other sediments. In addition to the corundum aggregates discussed here, the pyroclastic deposits carry mantle-derived xenoliths (spinel peridotites, garnet ± spinel pyroxenites, garnet websterites), lower-crustal xenoliths (garnet-ilmenite granulites), megacrystic Mg-ilmenite, amphibole, and clinopyroxene, and a suite of xenocrysts (olivine, orthopyroxene, Cr-diopside, pyrope garnet) derived from mantle peridotites and pyroxenites in a subcontinental lithospheric mantle ca 100 km thick (Apter, 2014; Esperança and Garfunkel, 1986; Kaminchik et al., 2014; our unpublished observations; Mittlefehldt, 1986).

Assertions that the highly reduced assemblages from Mt Carmel area are of anthropogenic origin (Litasov et al., 2019a; Litasov et al., 2019b) are untenable on the basis of detailed geological evidence (Griffin et al., 2020c; Griffin et al., 2019b). In brief: (1) all of the mineral assemblages described in this and previous papers are found *in situ* in the Cretaceous pyroclastic rocks; (2) the associated alluvial deposits do not come from the bed of the modern Kishon River, but from paleoplacers resting on bedrock at the base of Pliocene-Pleistocene terraces well above the current drainage, and overlain by 4-10 meters of undisturbed sediments; (3) much of the heavy-mineral assemblage, including abundant moissanite, also is found in lithified Miocene beach placers, deposited during a marine incursion that spread surface materials across the Yizra'el valley. All of these deposits predate human occupation. Contrary to statements by Litasov et al., the area is pastoral, rather than industrial, and the main primary sources (the volcanoes) lie on Mt Carmel, well above the Kishon valley, and in an extensive nature reserve. The same geological facts make

This is the peer-reviewed, final accepted version for American Mineralogist, published by the Mineralogical Society of America.
The published version is subject to change. Cite as Authors (Year) Title. American Mineralogist, in press.
DOI: https://doi.org/10.2138/am-2021-7934. http://www.minsocam.org/

it unlikely that the super-reduced phases have formed by lightning strikes (Griffin et al., 2018a).

Background: The Mount Carmel magmatic system

Most Carmel Sapphire comprises aggregates of skeletal to hopper-formed corundum crystals; this morphology indicates rapid crystallization from Al_2O_3-supersaturated melts or fluids (Figures 1, SD2; Griffin et al., 2016a). Melt pockets trapped within and between the corundum crystals contain mineral assemblages (tistarite (Ti_2O_3), SiC (moissanite), TiC, Fe-Ti-Zr silicides/phosphides) indicative of high *T* and low fO_2 (down to ΔIW ≤-6). Even lower fO_2 (ΔIW-9 to -10) is required by the precipitation of a coarse-grained hibonite-grossite-vanadium assemblage (Griffin et al., 2019a; Griffin et al., 2020b), also found in the volcanic debris.

The major questions relate to (1) the genesis of melts that could rapidly precipitate large volumes of corundum; (2) the processes that ultimately could produce fO_2 comparable to that of the early solar nebula. There is much yet to learn about this magmatic system, but basic paragenetic studies (Griffin et al., 2016a; Griffin et al., 2019a; Griffin et al., 2020a; Griffin et al., 2018b; Griffin et al., 2020b; Griffin et al., 2020c; Griffin et al., 2018d) and the abundance of carbon in the xenoliths (see below) suggest that the low fO_2 reflects the interaction of evolved magmas with mantle-derived (CH_4+H_2) at high fluid/melt ratios. An overview of the different parageneses in the melt pockets (Griffin et al., 2016a; Griffin et al., 2018d; Xiong et al., 2017) recognises four general types: silicate glasses that crystallize oxides and silicates (Type S); Ti-oxynitrides and Ti-borides (Type N; Griffin et al., 2020a); desilicated, fluoride-rich assemblages (Type DF; hibonite-grossite; Griffin et al., 2019a); Fe-Ti-Zr silicides and phosphides, associated with TiC and SiC (Type A, this work);.

The ejected material probably represents snapshots of individual melt-fluid subsystems, sampled by the eruptions at different stages of their evolution. However, if all of the material is treated as samples of a single system defined by declining fO_2, we can identify several stages of a proposed idealized process.

1. Precipitation of vesicular, Mn-rich wüstite, found in large (mm-to cm) fragments, which may reflect fO_2 near the magnetite - wüstite (MW) buffer.

This is the peer-reviewed, final accepted version for American Mineralogist, published by the Mineralogical Society of America.
The published version is subject to change. Cite as Authors (Year) Title. American Mineralogist, in press.
DOI: https://doi.org/10.2138/am-2021-7934. http://www.minsocam.org/

2. Precipitation of Mg-rich calcite (large zoned crystals with resorbed Sr-rich cores, $^{87}Sr/^{86}Sr$ = 0.70334±13; our unpublished *in situ* analyses) probably occurred near the EMOD buffer (ΔIW+1.5), taking up CO_2 released by the partial oxidation of introduced CH_4.

3. Separation of immiscible melts of Fe metal (Fe^0), Fe-oxides and Ti-oxides, with minor silicate components; these occur as abundant, commonly vesicular spherules up to a few mm across (Xiong et al., 2017). Their mineralogy suggests fO_2 equivalent to the iron-wüstite (IW) buffer. The low Ni contents (<1 wt%) of the Fe^0 melts suggest a mafic, rather than an ultramafic, parental melt.

4. Separation of immiscible, carbon-rich Fe-Ti-silicide melts, from which TiC and SiC crystallized (Huang et al., 2020; this work). This would lead to rapid desilication of the magma, producing Al_2O_3-supersaturation in the residual magma.

5. Rapid growth of skeletal/hopper corundum crystals, trapping pockets of Ca-Al-Si oxide melt (Oliveira et al., 2020). Continued crystal fractionation and reduction in fO_2 led to further immiscibility, producing many of the alloy assemblages described here.

6. Precipitation of coarse hibonite+grossite+spinel aggregates, and immiscible separation of vanadium (V^0) melts, from late low-Si oxide melts that are not clearly related to the corundum aggregates (Griffin et al., 2020b).

The important role of CH_4 in the evolution of this system is reflected in the precipitation of abundant SiC and TiC, the obvious presence of abundant volatiles (stages 1, 3) and the abundance of amorphous carbon in networks of breccia veins through the corundum aggregates, injected during or shortly before explosive eruption (Fig. SD4). The occurrence of native vanadium (V^0) and vanadium dihydride (VH2; Bindi et al., 2019) implies a coexisting fluid phase dominated by H_2, at least at late stages (Griffin et al., 2019a).

Quench-textured dmisteinbergite (a polymorph of anorthite) in the melt pockets reflects the peritectic reaction Liq + Crn → An, equivalent to the incongruent melting of anorthite (An → Liq + Crn). This well-studied reaction is experimentally constrained to pressures (*P*) >0.9 GPa and temperatures (*T*) of ca 1450 °C (Goldsmith, 1980). Thermodynamic modelling in the CaO-Al_2O_3-SiO_2 system (Ottonello et al., 2013) suggests that grossite is not stable at P >1 GPa. The same modelling shows that the trapped silicate melts would not be in equilibrium with corundum at P <1 GPa. These *P-T* estimates place the proposed site of fluid-melt interaction in the uppermost mantle; the crust-mantle boundary in the area has been geophysically defined at ca 25 km depth (Segev and Rybakov,

2011). Numerical modelling of zoning patterns in the corundum aggregates indicates that corundum initially grew in open systems that closed as crystallization proceeded, and that this happened on geologically short timescales (days to years; Oliveira et al., 2020).

Sampling and Methods

The field sampling and laboratory processing procedures, designed to exclude contamination, have been described in detail by Griffin et al. (2021).

The corundum aggregates and the included phases have been characterized using optical microscopy, scanning electron microscopy (SEM, FE-SEM) and energy-dispersive Xray spectroscopy (SEM-EDS), electron microprobe analysis (EMP-WDS), cathodoluminescence (CL), 3D-CT scanning, LA-ICP-MS analysis (trace elements), FIB-TEM (imaging, crystallography, TEM–EDS, EELS) and Raman spectroscopy,. The details of methods are given in the Supplementary Data.

Table 1 includes both SEM-EDS and EMP-WDS analyses, because in some cases phases large enough to be analyzed by SEM were too small to analyze with the available conventional EMP. Where the two types of data can be compared, the results show good correspondence, even though the averaged data for each phase are not necessarily from the same grains (see Table 1). TEM-EDS analyses are given in Table 2.

Results

Petrography

Corundum and melt pockets

Most fragments of the Carmel Sapphire are yellow-orange to dark brown in colour. Nearly all are irregular in shape, but some are rectangular prisms with depressed faces consistent with hopper growth (Fig. SD2a). Transparent fragments (Fig. SD2b) reveal intricate 3-dimensional networks of darker or brighter material. These represent pockets of silicate melts (darker in Fig. SD2c) and metallic melts (brighter) trapped between and within crystals. Strong CL correlates negatively with Ti contents (high Ti = darker CL) and outlines growth zoning and skeletal growth (Fig. 1); Ti contents typically rise toward melt pockets (Oliveira et al., 2020). Many larger specimens are cut by veins consisting mainly of carbon, and one of the largest specimens is a breccia of corundum fragments and minor SiC in a

carbon matrix. Raman spectroscopy, EBSD spectra and TEM analysis all indicate that the carbon is amorphous.

The corundum aggregates represent a complex, rapidly evolving mesh of growing crystals, melts and fluids, in which the sizes and shapes of trapped melt volumes were continuously changing (Oliveira et al., 2020). An important part of this evolution, as discussed below, was the multistage immiscibility between silicate melts, silicide melts and a fluid phase that was dominated by CH_4 and H_2 (Griffin et al., 2019a; Huang et al., 2020). High-resolution 3D-µCT images (Figure SD2) show that a single "melt" volume may contain silicate melts (glasses) in one branch, silicide melts ("alloys") in another, and fluids (seen as "voids" in these images) in a third one. This can make it difficult to identify coexisting phases in 2D images. However, most aggregates contain many trapped melt pockets, and an overview of these can identify the coexistence of certain phases and help to recognize immiscibility relationships, even when these features may not be directly observable in a given pocket.

The mineral associations recognized in the petrographic study are summarized below.

Native Iron (Fe^0)

Spheres of native iron (Fe^0) occur as isolated inclusions in corundum, and more rarely in pockets of Ca-Al-Si oxide glass (Fig. 2). The slightly irregular borders and apparent intergrowth with the phenocryst phases ($TiAl_2O_5$, tistarite and spinel in this example) suggest that the Fe^0 melt was in equilibrium with the oxide melt.

Silicides and phosphides

Many of the silicide and phosphide phases occur in rounded balls of Fe-Ti-silicides enclosed in the silicate glasses and intergrown with oxide and silicate phases, or isolated in corundum. Some of these relationships are shown in Figure 3, where balls and irregular masses of FeTiSi are enclosed in an unknown Mg-Ti-Al oxide together with tistarite (Ti_2O_3), carmeltazite ($ZrAl_2Ti_4O_8$) and Ca-Al-Si oxide glass. The FeTiSi contains many small euhedral grains of TiB_2. On closer inspection by TEM (Fig. 3c), the FeTiSi appears to be breaking down into three distinct silicides, enriched in Fe, Ti and Cr, respectively. The irregular boundaries among these phases suggest that this unmixing occurred in the molten state. Figure 3c also shows that euhedral TiB_2 crystallized from the silicide, probably before the unmixing (Griffin

et al., 2020a), and the silicide is associated with TiS. The hexagonal structure (P6_3mc) of this sulfide, as measured by TEM-ED, distinguishes it from wassonite (rhombohedral, R3m), found in the Yamato 691 enstatite chondrite (Nakamura-Messenger et al., 2012).

The Fe-Ti silicides contain euhedral crystals of TiC (khamrabaevite) that indicates crystallization of TiC directly from the silicide melts. The microstructures (Fig. 4) suggest that growing corundum crystals trapped and overgrew early TiC crystals, while expelling the host Fe_3Si melt into progressively smaller interstitial pockets. TEM imaging shows a narrow zone of $(Zr,Ti)_2P$ along the contact between the two phases; this may have formed as Zr and P were expelled from one or both phases on cooling. Similarly, isolated grains of Fe_3Si commonly are rimmed by grains of TiC, TiB_2 and/or Ti(N,O) (Fig. 5). Silicide melts within glass pockets, apparently coexisting with tistarite and/or carmeltazite, may show similar concentrations of TiC, but in these cases it is not clear how much of the TiC has crystallized from the metallic melt, or from the oxide melt (Fig. 6).

The coexistence of immiscible silicide and oxide melts implies that similar major phases should be found in both types of melts, though at different abundances and with small differences in composition. The first phase to crystallize from many oxide melts is a Mg-Al spinel, and similar spinels are found in some silicide melts (Fig. 7), intergrown with a Ca-Al-Ti oxide phase ($(Ca,Mg)_2(Al,Ti,Zr)_{10}O_{17}$) and TiC. The same Ca-Al-Ti oxide occurs intergrown with carmeltazite in a nearby pocket of Ca-Al-Si oxide glass. The irregular outlines of the spinel grains in the silicides suggest that they crystallized against the melt phase, but after TiC. In this case a phosphide phase ($(Fe,Ti)_2(Si,P)$) with straight edges also appears to have crystallized from the original silicide melt, leaving an FeTiSi phase in the liquid state. This occurrence of Fe-Ti-Si-P phases is relatively common (Fig. 8). However, in many of the Fe-Ti silicide melts that show breakdown to ≥2 phases, as in Figure 3, the microstructures suggest the separation of immiscible melts. The most common minor, apparently exsolved, melts are richer in Ti and/or P than the original bulk silicide (Fig. 9).

A spectacular example of melt immiscibility is shown in Figure 10; spheres consisting of intergrown Zr-Ti-U phosphides and Ti-Zr-Fe silicides are embedded in a Ca-Al-Si oxide glass that also has crystallized Mg-Al spinel and hibonite ($CaAl_{12}O_{19}$). More commonly, the Zr-Ti silicides and phosphides are found as isolated inclusions in the corundum, many associated with TiC (Fig. 11). The fluidal contacts revealed in TEM images suggest that the silicides and phosphides in Figure 11 separated as melts, while the Zr-Ti-U phosphide

crystallized from the silicide melt (cf. Fig 10). Other examples of these phases and their relationships to TiB_2 and TiC are shown in Griffin et al. (2020a).

Relationship to SiC

Moissanite (SiC) is a rare phenocryst in the Ca-Al-Si oxide melt pockets; most of the abundant moissanite recovered from the ejecta and alluvial deposits occurs as single grains. A study of the inclusion assemblages in such grains (Huang et al., 2020) shows that the SiC crystallized from a silicon-rich melt with minor contents of Fe, Al and Ca; some of the inclusion phases are identical to those found in the Fe-Ti silicide assemblages in the corundum aggregates. One sample (Fig. 12) illustrates some of these relationships. In an inclusion in corundum, a large TiC crystal has crystallized from a Ti-Fe silicide melt, along with a crystal of the undescribed phase Ti_3SiC_2 (a natural "MAX phase"). The latter crystal is separated from the silicide matrix by a zone of TiSi, from which abundant SiC has crystallized. These relationships are consistent with immiscibility between the oxide and silicide melts in the corundum, and the metallic melts that crystallized the bulk of the SiC in the overall magmatic system.

Mineral chemistry

Fe-Ti Silicides

Most of the phases described here show a range of solid solution. Where individual analyses are plotted in the Fe-Ti-Si ternary (Fig. 13a), clusters of data can be identified (Fig. 13b). Average analyses for each cluster are given in Table 1, and Table 2 gives TEM-EDS analyses of some individual phases found in FIB foils. Analyses plotted in Figure 13 may contain up to 6 wt% Zr and/or 5 wt% P, as well as small amounts of Mn, Ni, Cr, Al and V (Table 1); these minor elements have been grouped with the major elements (Mn and Ni with Fe; Cr, Al and Zr with Ti; P with Si). The presence of such minor elements may distort the apparent relationship between the plotted compositions and the phase boundaries as defined in the simple ternary system. However, at these low levels the distortions are not expected to affect the conclusions drawn here.

Cluster 1. The mean composition is near Fe_2Si_5 (Table 1, #1); all are drop-shaped blebs, or occasionally euhedral crystals, within inclusions of metallic Si (Si^0) in crystals of SiC, some

enclosed in corundum aggregates. A series of other analyses, also from inclusions in SiC (Huang et al., 2020), extends toward the composition of cluster 3.

Cluster 2. All analyses are from a single melt pocket enclosed in corundum; a crystal of Ti_3SiC_2 (Table 1, # 16) is separated from a matrix of zangboite ($FeTiSi_2$) by a reaction zone of $Ti_{1-x}Si_2$+x and SiC (Fig. 12; Table 2, #8). This phase, with a mean composition of $(Ti,Fe)Si_2$ (Table 1, #2), also occurs as irregular dark areas within the zangboite matrix. However, TEM-EDS analyses of inclusions in the matrix (Table 2, #6, 7) have less Fe and compositions closer to Ti_2Si_3.

Cluster 3. The mean composition corresponds to zangboite ($FeTiSi_2$; Table 1, #3), which includes the main phase in the melt inclusion shown in Figure 12 (Table 2, #5). It is found as isolated 5-10 μm inclusions in both corundum and moissanite (Huang et al., 2020) and in one case coexists with $(Fe,Ti)_3Si_2$ (cluster 4). Zangboite is also found in heavy-mineral separates from chromitites in the Luobusa ophiolite of southern Tibet (Xiong et al., 2017; Xu et al., 2015). It corresponds to the liquidus phase τ_1 in the synthetic Fe-Ti-Si system (Weitzer et al., 2008); Fig. 13a).

Cluster 4. The mean composition is close to $(Fe,Ti)_3Si_2$ (Table 1, #4). The analyses represent small rounded inclusions in corundum; one surrounds a rectangular grain of zangboite. This phase has been found in spinel-peridotite xenoliths from the Avacha volcano on Kamchatka (Ishimaru et al., 2009), but has no formal name.

Cluster 5. Ten analyses have a mean composition corresponding approximately to the mineral xifengite (Fe_5Si_3; Table 1, #5). One is enclosed in a Ca-Al-Si glass together with carmeltazite ($ZrAl_2Ti_4O_{11}$), Ti(N,O) and TiC (Fig. 6). Others form the cores of inclusions in corundum, with irregular, apparently exsolved blebs of $(Fe,Ti)_2(Si,P)$ and/or $(Fe,Ti)_{11}Si_5$ (Fig. 9a). Xifengite has been found in placers in the Yan mountains of Hebei Province, China, and in the Is River in the Middle Urals region of Russia (Yu, 1984).

Cluster 6. This large cluster can be divided into three more homogeneous subgroups, with mean compositions corresponding to gupeiite (Fe_3Si), Fe_5Si_2 and $(Fe,Cr)_3(Si,P)$ (Table 1, # 6-8). The first typically occurs as irregular masses interstitial to corundum crystals, associated with abundant TiC (Figs 4a, 4b,5). A FIB section across the contact between a TiC crystal and gupeiite (Fig. 4c) shows they are separated by a zone of $(Zr,Ti)_2P$ (Table 2, # 9). The second type (Fe_5Si_2) also occurs as large irregular pockets, typically associated with crystals or irregular blebs of Fe-Ti-Si-P phases (Table 1, #6, 9). A TEM image shows a sharp

contact between the two phases (Fig. 8), with zoned inclusions of $(Fe,Ti)_3(Si,P)$ (cf. Table 1, # 10). The third, more Cr-rich type ($(Fe, Cr)_3(Si, P)$); Table 1, #8) typically occurs as small grains/droplets, associated with carmeltazite, Ti(N,O) and TiB_2, either enclosed in corundum, or in melt pockets with Ca-Al-Si oxide glass. Gupeiite is found in alluvial deposits in the Yan Mountains (China) together with xifengite (Yu, 1984). It also occurs with xifengite, FeSi, $FeSi_2$, SiC and TiC in soils of the Alpine foreland (Hiltl et al., 2011).

Cluster 9. This small group of analyses (Table 1, #9) has a mean composition near $(Fe,Ti)_{11}Si_5$; they all represent small, apparently exsolved volumes in Fe_5Si_3.

Cluster 10. Three SEM analyses represent small isolated inclusions in corundum. Two TEM-EDS analyses represent inclusions in $(Fe,Ti)_2Si$ (Fig. 8); one is zoned toward a rim enriched in Fe and depleted in Ti. The compositions range from $(Ti, Fe)_3Si$ to $(Fe,Ti)_7(Si,P)_3$ (Table 1, #10; Table 2, #14,15).

Cluster 11. Most of these analyses make up the cores of complex zoned inclusions in corundum, surrounded by the grains gathered in cluster 12 (see below), and by shells consisting of the unknown phase $MgTi_2Al_4(Si,Zr)O_{10}$ and several other phases (Fig. 3a). The mean composition of the cores (Table 1, #11) is FeTiSi, which corresponds to the τ_2 phase of Weitzer et al. (2008), with some Cr in solid solution. The spread of the analyses corresponds to the known range of solid solution in FeTiSi at T ≥1100 °C (Weitzer et al., 2008). However, TEM imagery (Fig. 3b, 3c) shows that the FeTiSi in at least one case now comprises three distinct Ti-Fe-Cr silicides, which appear to have unmixed on cooling. One is dominated by Ti, another by Fe, and the third by Cr; this unmixing on the micron scale probably accounts for the high standard deviation on the mean SEM-EDS analyses (Table 1, #11).

Cluster 12. This is a sub-horizontal array of points with a mean composition near $FeTi_2Si_2$ (Table 1, #12) but with a wide range in Ti/Fe, and significant but variable levels of Cr, V and Mn. Some of these analyzed grains occur with FeTiSi in zoned inclusions in corundum, but show straight edges suggestive of crystal forms. Others occur as rectangular crystals in a matrix of Ca-Al-Si-O glass inclusions in corundum. The mean composition corresponds to the τ_6 phase of Weitzer et al. (2008) but it may not represent a single phase.

Cluster 13. Nine analyses all represent small isolated inclusions in corundum (one with $TiSi_3$); the mean composition is Ti_5Si_4 with ca 5 at.% Fe in solution (Table 1, #13).

This is the peer-reviewed, final accepted version for American Mineralogist, published by the Mineralogical Society of America.
The published version is subject to change. Cite as Authors (Year) Title. American Mineralogist, in press.
DOI: https://doi.org/10.2138/am-2021-7934. http://www.minsocam.org/

Cluster 14. Three analyses with a mean composition near (Ti, Fe)$_3$Si (Table 1, #14) represent small blebs grouped around TiC crystals in 10-µm inclusions, or coexisting with Fe$_3$Si, (Fe,Ti)$_2$Si, Ti(N,O) and TiB$_2$ (Fig. 5). The mean composition is also close to that of the subsolidus phase Ti$_5$Si$_3$ (Fig. 13b).

Cluster 15. A small group of analyses corresponding to Ti$_3$Si (Table 1, #15) represents lamellae in complex inclusions with TiC, TiSi and other phases, and in balls of silicide-phosphide phases (Table 2, #3). C is not visible in the EDS spectra. Ti$_3$Si is a subsolidus phase that appears below ca 1170 °C (Fig. 13b).

Miscellaneous individual analyses

A number of analyses, mostly of small isolated inclusions in corundum, fall outside the obvious clusters in Figure 13b; most have compositions that cannot be expressed as rational formulae. Many of these lie on or near cotectic lines in Figure 13a, suggesting that they represent trapped melts rather than distinct phases. However, one analysis represents a high-Ti alloy (Ti$_{84}$V$_5$Cr$_{1.5}$Fe$_6$Si$_{2.5}$), which occurs as a small rectangular crystal in Fe$_3$Si. A series of analyses extending from the (Fe+Mn+Ni) corner lies along the edge of the field of Fe solid solution in Figure 13b; all of these are individual inclusions in corundum.

Fe-Ti Phosphides, Silicide/Phosphides

Analysis 17. A single 10-µm sphere of (Cr,Ti,Fe)P (Table 1, #17) occurs in a pocket of Ca-Al-Si glass, together with early-crystallizing tistarite and carmeltazite.

Cluster 18. Four irregular grains associated with Ti(N,O) and TiB$_2$ have a mean composition of (Fe,Ti)$_3$P (Table 1, #18). There is only minor solid solution toward (Fe,Ti)$_3$Si.

Cluster 19. A relatively common phase, with mean composition (Fe,Ti)$_2$(Si,P) (Table 1, #19). All occurrences are enclosed within balls or irregular masses of Fe$_3$Si, either as triangular to rhomb-shaped areas suggestive of crystals, or as irregular blebs suggesting liquid immiscibility (Fig. 14). There is significant solid solution; Si/P (at.%) ranges from 1.0 to 4.2.

Zr-Ti Phosphides, Silicides (Figure 15)

This is the peer-reviewed, final accepted version for American Mineralogist, published by the Mineralogical Society of America.
The published version is subject to change. Cite as Authors (Year) Title. American Mineralogist, in press.
DOI: https://doi.org/10.2138/am-2021-7934. http://www.minsocam.org/

Cluster 20. (Zr,Ti)P (Table 1, # 20) is found as a 5-µm triangular crystal coexisting with Mg-Al spinel and hibonite interstitial to corundum, and in the irregular cores of silicide balls. It also occurs as a rim between TiC and Fe_3Si in Figure 4c.

Cluster 21. Four grains of relatively uniform composition, with a mean of (Zr,Ti)(P,Si) (Table 1, #21) These are closely associated with TiC, $TiSi_2$ and other Zr-Ti silicides (Fig. 11); some appear to have crystal forms.

Analysis # 22. $Zr_3Ti_7(Si,P)_8$ is found as subhedral grains intergrown with $(Zr,Ti)Si_2$ and $(Zr,Ti)_2P$ in a 30µm ovoid inclusion in corundum that also contains a large crystal of TiC and a grain of a U-rich Zr-Ti-P-Si phase (Fig. 11d; Table 2, #9-12).

Clusters 23-25. These phases occur in spherical aggregates embedded in Ca-Al-Si glass within a melt pocket in corundum (Fig. 10a). TEM imaging reveals an equilibrated equigranular microstructure with open voids (Fig. 10b). One of the phases identified by SEM-EDS is $(Ti,Zr,Fe)(Si,P)_2$ (Table 1, # 23). Analysis #24 (Table 1) is the mean of 13 analyses with relatively constant Si, but a range in Ti/Zr (at.%) from 0.6 to 1.5. The mean composition can be expressed as $(Ti, Zr)Si_2$ (see also Table 2, #11). This phase also occurs as inclusions in TiC, and coexisting with TiC and/or $FeTiSi_2$ in isolated inclusions; these grains tend to have the highest Ti/Zr. The third component of the spherical crystalline aggregates has a mean composition of $(Ti,Zr)Si_7$ (Table 1, # 25); a TEM-EDS analysis (Table 2, # 1) has the composition $(TiZr)_3Si_7$, within the range of variation in the SEM analyses.

TEM analysis also identified a uranium-rich phase (18-23 wt% U; Fig. 10c). The mean of two grains in two different samples fits an approximate empirical formula of $(Zr,Ti,U)_5(P,Si)_3$ (Table 2, #2 and #12).

DISCUSSION

Comparison of observations with experimental studies

Fe-Ti silicides

Nearly all experimental work relevant to the phases described here has been done at one atm pressure, in the course of metallurgical research. However, given the relatively shallow conditions (near 1 GPa) estimated for the crystallization of the corundum-SiC system at Mt Carmel (Griffin et al., 2016a; Griffin et al., 2018d), the determined phase relationships are likely to be relevant, while the temperatures of crystallization may be slightly underestimated. The melting curve of Fe provides a possible reference point

(Sinmyo et al., 2019); at 1 GPa the melting point is only 100 °C higher than at 1 atm. On the other hand, the presence of minor elements (Mn, Ni, Cr, Al, V) and the presence of H_2 in the fluid phase (see below) may lower liquidus temperatures by at least this much, relative to the simple system.

The liquidus phases along the Fe-Si join (Fig. 13a) are (1) the β_2 phase, which represents solid solution of Si in Fe, and crystallizes as Fe_3Si from 1215 °C to a eutectic with (2) Fe_2Si, with a narrow field of crystallization just above 1200 °C, leading to a eutectic with (3) FeSi which crystallizes from 1412 °C to 1215 °C , ending in a eutectic with (4) Fe_2Si_5, which crystallizes over a narrow *T* range near 1215 °C, to a eutectic with Si. With the addition of Ti, there is a small field in which Fe_5Si_3 is on the liquidus from ca 1175 to 1150 °C.

On the Ti-Si join, Ti_5Si_3 is the dominant phase, crystallizing on the Ti-rich side from ca 1920 °C to a eutectic with Ti at 1330 °C, and on the Si-rich side through a series of peritectics that crystallize Ti_5Si_4 from 1920 to 1570 °C, then TiSi from 1570 to 1487 °C, a eutectic with $TiSi_2$. $TiSi_2$ also crystallizes down to a eutectic with Si at ca 1330 °C.

The Fe-Ti join is relatively simple. Fe_2Ti is on the liquidus from ca 1400 °C to eutectics with Fe at ca 1300 °C and FeTi at ca 1320 °C; FeTi is on the liquidus down to a eutectic with Ti at ca 1050 °C (Fig. 13c).

The center of the Fe-Ti-Si liquidus diagram (Fig. 13a) is controlled by two ternary phases: $FeTiSi_2$ and FeTiSi (τ_1 and τ_2 of Weitzer et al., 2008). These two phases melt congruently above 1500 °C and 1700 °C respectively, and crystallize from ternary melts along a complex series of cotectics and peritectic points that fall from temperatures of ca 1660 to 1263 °C on the Ti-rich side of the phase diagram, and from ca 1530 to 1150 °C on the Fe-rich side.

The subsolidus phase relationships at 900 °C (Fig. 13b) have been constructed by Weitzer et al. (2008); they note that these relationships are also valid at 1000 °C. A reconstruction by Stein et al. (2005) at 1150 °C (Fig. 16) shows the transition between the liquidus and the high-T subsolidus situation, while a section at 800 °C (not shown) extends the subsolidus to lower T. The most important differences between the liquidus situation and the isothermal section at 900 °C are: the disappearance of Fe_2Si and its replacement by Fe_5Si_3 with solid solution toward Ti_5Si_3; the extensive solid-solution fields of "Fe_3Si" toward Fe, and of Fe_2Ti (the Laves phase) toward Si; the appearance of Ti_3Si coexisting with Ti and

Ti_5Si_3; and the appearance in the 900 °C section of several ternary phases, none of which have been found in this study.

These relationships allow some evaluation of the origin of some of the clusters of data shown in Figure 13b. It should be kept in mind that these melts were evolving in individual, separated pockets of trapped melt. The ongoing growth of corundum was continually changing the size, shape, and connectivity of these pockets (Oliveira et al., 2020), and this would influence the evolution of single volumes of melt, for example by overgrowing and isolating crystals and melt droplets (Fig. 4). It is also probable that individual ejecta, especially from different vents, may represent samples of similar, but not identical, systems at different stages of their cooling histories.

Figure 17 shows tie lines between apparently coexisting phases, as based on petrographic relationships. Green tie lines connect Fe_3Si-type phases (clusters 6-8) with compositions near FeTiSi; these tie lines are consistent with subsolidus equilibration, as is the zoning of the inclusion shown in Fig. 8. However, most of the tie lines (red in Fig. 17) have negative slopes and cross-cut the subsolidus tie lines in this part of the phase diagram, and the pairs of phases joined by these tie lines cannot be in equilibrium at subsolidus conditions. Most of these analyses lie on or near cotectic curves; this and the microstructures (e.g. Figs 7,9,14) suggest that these represent mutually immiscible melts. Unfortunately we have found no experimental data on immiscibility in the Fe-Ti-Si system with which to test this interpretation.

On the basis of this type of analysis and petrographic observations, it is possible to assign the analysed grains to liquidus phases (crystallizing from the melt), trapped melts modified to various degrees by fractional crystallization, or subsolidus phases representing recrystallization of earlier-crystallized phases, or of solidified melts (Table 1). The phases identified as crystallizing directly from melts have moderately high concentrations of Cr and V (Table 1), and these two elements show a broad positive correlation, suggesting that most liquidus phases concentrated Cr and V relative to the residual liquids. In contrast, xifengite (a subsolidus phase?) has high V but low Cr. Cluster 8 represents a Cr-rich version of Fe_3Si, and on that basis also may represent a liquidus phase.

Within the limitations noted above, these phase assemblages give a basis for estimating the temperatures under which the corundum-SiC system was crystallizing. The crystallizing phases and melts on the Ti-Si side of Fig. 13c imply temperatures in the range

1660-1280 °C. The temperatures of first crystallization for the three important phases Ti_5Si_3 (>2100 °C), FeTiSi (ca 1700 °C) and (Fe,Ti)Si_2 (ca 1500 °C) are much higher, but each can crystallize down to 1300-1400 °C along the cotectics that surround their fields of primary crystallization. The assemblages on the Fe-Si side of Fig. 13c imply lower crystallization temperatures ranging down to 1175-1150 °C.

These *T* estimates probably are maximum values. Such melts may take up significant amounts of hydrogen from the ambient fluids, lowering liquidus temperatures by hundreds of degrees (Fukai, 2006); the addition of carbon to the Fe-Si system also strongly depresses the liquidus of Fe-Si alloys (Vander Kaaden et al., 2017). However, it is significant that few of the trapped melts have crystallized into the various 2- and 3-phase assemblages illustrated in the isothermal sections at 1150 and 1000-900 °C. This suggests that the temperatures in the corundum-SiC system had not dropped much below 1150 °C by the time crystallization was interrupted by the explosive eruption of the host magma.

Fe-Ti phosphide-silicides

We have not been able to access experimental data on the liquidus configuration of the Fe-Ti-P(Si) system. An isothermal section of the Fe-Ti-P system at 800 °C (not shown) is dominated by the ternary phase FeTiP, which has not been identified in this study. Binary diagrams show that FeTiP is a liquidus phase from T>1500 °C, so its absence is unexpected. (Fe,Ti)$_2$P (cluster #18) shows a significant solid solution toward FeTiP. Analysis #18 (Table 1) and cluster #19 may represent mixtures of two or more phases.

Zr-Ti silicides, phosphides

The analyses of Ti phosphides define two clusters, one between Ti_3P and Ti, the other between Ti_3P and Ti_2P. The latter would correspond to mixtures of Ti_2P and liquids crystallizing that phase from ca 1920-1760 °C in the experimental system., while the former could represent Ti_3P and coexisting liquids from ca 1760-1495 °C (Ohtani et al., 2006). These temperatures would be lowered by solid solution with both Si and hydrogen. The points around the mean composition (Zr,Ti)P (cluster 21) do not represent obvious subsolidus phases, and are tentatively interpreted as trapped melts. However, several of the individual analyses taken from FIB-TEM foils (Table 2) lie close to recognized subsolidus phases, which is consistent with their microstructural appearance.

The Ti-Zr-Si plot (Fig. 15a) shows a nearly continuous series of analyses on the Ti-Si join; some of these contain several at.% P as well (Table 1). The spread of analyses corresponds to a sequence of peritectic reactions on the binary liquidus from ≥2000-1550 °C, and may represent crystals, reaction products and trapped melts. These temperatures also probably represent maximum estimates, and would be lowered by solid solution of Si, Fe and H. The spread of points in clusters 23 and 24 represents extensive solid solution approximately along the $TiSi_2$-$ZrSi_2$ join. An isothermal section of this ternary at 500 °C (Zhan et al., 2009) shows ca 10% solid solution along this join from each end member; the present data suggest higher temperatures, but with no real constraints. The phase represented by analysis #25 in Table 1 is consistent with a eutectic melt (*T* ca 1300 °C) which would be crystallizing both Si (observed as inclusions in SiC) and a (Ti, Zr)Si_2 phase. Cluster 21 (Fig. 15b) lies in a 3-phase field at 1200°C, and may represent mixtures, or a liquidus melt composition inherited from higher *T*.

SiC relations

SiC is on the liquidus in Si-rich melts from ca 2720 to 1520 °C (Kawanishi et al., 2009). At 1500-1450 °C (Fig. 18), SiC can coexist with a range of Fe-Si melts, but if the system is carbon-saturated, SiC coexists with carbon and a melt of Fe_3Si composition, which can dissolve several percent C. At 1300-1250 °C, this assemblage is still stable, but the content of C in the Fe_3Si is lower. The reconstructed melt inclusions in the SiC can coexist with SiC at 1450°C, but not at temperatures as low as 1250 °C (Fig. 18b;) (Huang et al., 2020). In more Si-rich melts SiC can coexist with Fe_3Si + FeSi, or FeSi +Si; FeSi has not been observed in the samples studied by Huang et al. (2020). Takahashi et al. (2013) have shown that as fO_2 decreases (to < ΔIW-4.8), the solubility of carbon in Fe-rich melts decreases, and the solubility of Si increases. The low contents of carbon in the Fe_3Si samples analysed here (Table 1) thus are consistent with both carbon saturation and very low fO_2. However, the carbon content of the Fe_3Si will also be affected by the crystallization of TiC (Fig. 4) and there are not enough data to use the reconstructed C content of the alloy phase to estimate temperatures.

At subsolidus temperatures (1200 °C, 0.24 GPa) the phase relations are consistent with the petrographic relationships. SiC coexists with Ti_3SiC_2 and $TiSi_2$ (Fig. 12b), and Ti_3Si can coexist with TiC.

This is the peer-reviewed, final accepted version for American Mineralogist, published by the Mineralogical Society of America.
The published version is subject to change. Cite as Authors (Year) Title. American Mineralogist, in press.
DOI: https://doi.org/10.2138/am-2021-7934. http://www.minsocam.org/

567

568 **Composition and evolution of Fe-Ti-Si-P-C melts**

569 To follow the evolution of the metallic melts the bulk compositions of six large,
570 complex Fe-Ti-Si-P-C inclusions (e.g. Figs 4, 8, 9 and others) have been reconstituted, based
571 on point-counting of phase abundances in BSE images and EDS maps (Table 3). This
572 procedure is subject to the uncertainties inherent in using 2D images to estimate phase
573 distributions in 3D objects, but in this case the results appear to carry useful information.
574 The reconstructed melt compositions fall close to cotectic curves In the Fe-Ti-Si
575 ternary liquidus diagram (Fig. 19), suggesting they were trapped as metallic melts. Apparent
576 temperatures range from ca 1600 °C (Table 3, #41) to ca 1150 °C; these probably represent
577 maximum values, as noted above. During cooling, the Si and Fe contents of the Fe-Si melts
578 increase, while Ti and C decrease. The textural relationships (Fig. 4) indicate large-scale
579 crystallization of TiC early in the evolution of the melts, while TiC is less abundant in the
580 more Fe-rich melts. The distribution of the reconstructed melts on Figure 19 indicates that
581 they cannot all represent sequential stages in the evolution of a single parental melt.
582 Instead, it seems probable that several different sub-systems have been sampled, with
583 different parental melt compositions and consequently different melt-evolution paths.
584 The solubility of Si, Ti and C in Fe-rich melts is strongly dependent on fO_2 (Corgne et
585 al., 2008; Gessmann et al., 2001; Putter et al., 2017). In the case of the earliest melts, we
586 can assume fO_2 was around ΔIW-7, since Ti_2O_3 (tistarite) is an early-crystallizing phase in the
587 silicate melts coexisting with the metallic melts (Griffin et al., 2016a). The Si content (8 wt%)
588 in the highest-*T* melt (#41 in Table 3) is broadly consistent with the experimental data of
589 Gessman et al. (2001) at projected conditions of ΔIW-7, 1 GPa and 1600 °C; lower *P* or *T*
590 would decrease the level of Si expected in the melt, but the available experiments do not
591 account for the potential solubility of H_2 in Fe melts and its effects on melting points (Fukai,
592 2006).
593 The lower-*T* reconstructed melts have Si contents up to >20 wt%; this is not consistent
594 with the decrease in Si expected with declining *T* (Fig. 20). An isobaric increase in Si content
595 (with decreasing *T*) thus requires a large decrease in fO_2. This is consistent with other
596 evidence that the fO_2 of the idealized system dropped during the evolution of the melts,
597 first to ΔIW-6 (appearance of SiC), then to ΔIW-7 (stability of Ti_2O_3) and then to ΔIW-9
598 (appearance of V^0) (Griffin et al., 2019a; Griffin et al., 2020b); the presence of TiB_2 (Griffin et

al., 2020a) may indicate even lower fO_2. A decrease in both *T* and fO_2 also will reduce the solubility of C in the metal liquid (Takahashi et al., 2013) (Fig. 20), driving the more or less continuous crystallization of TiC (and possibly SiC) during the evolution of the melt. The depletion of C from the metallic melts relatively early in their evolution may explain the apparent absence of Fe_3C (cohenite) in the melt pockets.

The lower-*T* metallic melts are richer in Cr, and to some extent V (Table 3); this is predicted by experimental studies showing that these elements become more siderophile with decreasing fO_2 (Corgne et al., 2008; Putter et al., 2017). The maximum Cr content (3.5 wt%) is reached in inclusion #9b (estimated T = 1300°C) and drops again in the two lower-*T* inclusions. This may indicate that all Cr has been sequestered in the metallic melt by this stage; alternatively, it could reflect a change in $D_{Cr}^{metal/silicate}$ at very low fO_2 (Putter et al., 2017). However, a 2D sampling effect cannot be excluded.

With the exception of melt 9a (Table 3), the content of P increases with declining *T*. Experimental data (Gu et al., 2019; Putter et al., 2017; Steenstra et al., 2017) predict that P becomes more siderophile with declining *T* and decreasing fO_2, which is consistent with the pattern shown in Figure 19, but is less siderophile in high-Si melts. The exsolution of phosphide-rich melts from some Fe-Si melts (Figs 8, 9) therefore may reflect the increasing levels of Si in the lower-T melts (Table 3), leading to immiscibility despite the higher solubility of P in metallic melts at low *T* and low fO_2.

A generalized picture of the evolution of the metallic melts in the corundum aggregates, emphasizing the observed role of successive episodes of liquid immiscibility with decreasing fO_2, is shown in Fig. 21. The early stages of the reduction process, prior to the crystallization of corundum, are assumed to be responsible for the immiscible separation of abundant spheroids of native Fe (Fe^0), some of which are surrounded by shells of stoichiometric wüstite (FeO) (Xiong et al., 2017). These are accompanied by, and often attached to, spheres of Fe-oxide melts and Ti-oxide melts, both with minor Si and Ca. The separation of these metal and metal-oxide melts from the silicate melt is interpreted to have occurred near fO_2 = IW.

The next stage of immiscibility ((2) in Fig. 21a) produced the separation of C-rich silicide melts, from which SiC crystallized. These melts may have in turn exsolved into complementary fractions with higher and lower Si/(Fe+Ti). The microstructures in the melt inclusions in SiC suggest that the more Fe,Ti-rich fraction crystallized $FeTiSi_2$ (τ_1 in Fig. 13) as

a liquidus phase, and then $FeTiSi_2$ + SiC from cotectic melts (Huang et al., 2020). These melts included in SiC may in turn provide a link to the metallic melts in the corundum aggregates (Fig. 20; Table 4). The maximum Si contents of the reconstructed Fe-Ti-Si melts in the corundum aggregates are ca 25 wt%, while the minimum values of the Fe-Ti-Si melts included in SiC are ca 52 wt%; Fe/Ti (wt%) is 2.7 and 1.9 in the respective melts. We suggest that the most Fe,Ti-rich melts in the SiC and the most Si-rich metallic melts in the corundum aggregates may be conjugate immiscible melts; both would be C-saturated and both have crystallized SiC and $FeTiSi_2$, but in different proportions, consistent with equilibrium between immiscible melts.

The continued separation of such silicide melts ((3) in Fig. 21b) would desilicate the coexisting silicate melts, inducing supersaturation in Al_2O_3 and the rapid crystallization of the hopper/skeletal corundum at fO_2 *ca* ΔIW-7 to -9, and leaving a complex, Si-depleted oxide melt (Fig. 21b). The separation of the Fe-Ti silicide melts appears to have removed essentially all remaining Fe from the coexisting silicate melts; none of the oxide or silicate phases crystallized from the trapped silicate melts contain Fe. Crystallization of abundant TiC (Fig. 4) suggests that the metallic melts also were saturated in C; subtraction of TiC decreased melt volume and concentrated minor components, until Zr,Ti-rich phosphide/silicide melts became immiscible in the dominant Fe-Ti-Si melts, and Fe-Ti-Zr phosphide/silicide phases crystallized (Tables 1, 2), some with SiC and other carbides (Fig. 12; (4) in Fig. 21b). The end point of this idealized process might be the low-Si oxide melts that crystallized the coarse-grained hibonite-grossite assemblages, coexisting with vanadium- and vanadium-alloy melts (Griffin et al., 2019a, 2020b; Fig. 21a). The phase relationships discussed above suggest that this evolution spanned a range of temperature from ca 1500-1150 °C, before being terminated by explosive eruption. This lower- *T* limit is consistent with the presence of the phase $Ca_4Al_6F_2O_{12}$ in the hibonite-grossite-spinel aggregates (Kim, 2011; Griffin et al., 2018a). As noted above, the higher temperatures probably are maximum values, due to the solution of carbon, hydrogen and other elements.

Other Occurrences

The metallic melts described here are not unique; they have been observed worldwide in a variety of contexts. They are common in Kamchatka volcanoes and in mineral separates from ophiolitic chromitites in Tibet and the Polar Urals, where they may

be related to pre- or syn-emplacement magmatism (Griffin et al., 2018d; and references therin; Xiong et al., 2020; Xiong et al., 2017). Mantle-derived corundum from kimberlites of the East Azov area of the Ukrainian Shield, from the Karpinskaya pipe in the Arkhangelsk kimberlite province, and the Siberian Udachnya kimberlite, contains an inclusion assemblage similar to the Mt Carmel ones: tistarite, carmeltazite, TiN, native Fe, hibonite and a range of Fe-Ti silicides similar to those described here (Tatarintsev et al., 1987; Yatsenko et al., 2002; Yatsenko, 2016; Yatsenko et al., 2017; our unpublished data). Yatsenko and coworkers have drawn attention to the wider distribution of mantle-derived corundum and defined an "explosive mantle-derived mineral association (EMMA)". The assemblage of corundum, carbides (TiC, SiC), Fe-Ti silicides and native elements (Fe, V) has also been documented in volcaniclastic layers ("visherites" or miaskitic lamproites) at several localities in the western Urals (Chaikovskii and Korotchenkova, 2012). Similar associations of metallic spherules requiring reducing conditions have been described in placers interpreted as related to the impact of a proposed "Yanshan meteorite" in the Yan mountains of Hebei Province, China, and in the Is River in the Middle Urals region of Russia (Yu, 1984). Nodules (mm- to cm-size) comprising Fe-Ti silicides, SiC and TiC have been found in soils of the Alpine foreland over an area of ca 3000 km^2; these nodules also have been interpreted as fragments of meteorites (Hiltl et al., 2011), despite the lack of Fe-Ni alloys in the deposits. Such occurrences may instead be related to explosive volcanism (the EMMA of Yatsenko et al., 2017). It seems probable that similar associations will be found in the ejecta of other explosive volcanoes, using detailed studies of fine-grained heavy minerals from pyroclastic deposits.

Implications

The silicides, carbides and phosphides described here represent a series of melts and their crystallization products, trapped within aggregates of skeletal- to hopper-shaped corundum crystals. Microstructures indicate that the Fe-Ti-Zr-Si-P melts were immiscible with the Ca-Al-Mg-silicate melts trapped in the same aggregates. Reconstructed metallic melts fall on or near cotectic curves in the Fe-Ti-Si system and were precipitating FeTiSi and $FeTiSi_2$ during cooling. The Si-C rich melts found as inclusions in SiC crystals from the same volcanic ejecta may represent a conjugate immiscible component. Ti-Si and Zr-Ti-(P-Si)

694 melts appear to have become immiscible with the Fe-Ti-Si melts as T and fO_2 declined from
695 ca ΔIW-6 to ΔIW-9 during the crystallization process.
696 All of these coexisting melts were carbon-saturated, leading to the continuous
697 precipitation of TiC and minor SiC during cooling. The saturation of the melts in carbon is
698 consistent with the observed abundance of amorphous carbon in the final eruption
699 products, and is a strong argument for the role of $CH_4 + H_2$ in the fluid phase that generated
700 the low fO_2. This in turn implies that the deeper mantle from which such fluids might
701 ascend is metal-saturated, with fO_2 buffered near IW; this implication needs to be factored
702 into partial-melting models used to explain the genesis of common magmas such as MORB.
703 These observations indicate that sequential liquid immiscibility plays an important role
704 in the evolution and diversification of melts at low fO_2 in the uppermost mantle; it leads
705 directly to the desilication of oxide melts, oversaturation in Al_2O_3 and the crystallization of
706 abundant corundum. Similar processes probably occur in the deeper parts of cratonic roots,
707 as illustrated by the overall similarity of melt inclusions in SiC from kimberlites and from Mt
708 Carmel (Huang et al., 2020). They can also be recognized in the occurrence of similar silicide
709 alloys and inclusion-rich corundum in a range of explosive volcanic environments (Xiong et
710 al., 2017; Yatsenko et al., 2017), implying that reduced mantle-derived fluids may play a
711 little-recognized role in the genesis of such magmas.
712
713 **Acknowledgements**
714 WLG and SYO'R acknowledge the research funds for the TARDIS Project provided by
715 the ARC Centre of Excellence for Core to Crust Fluid Systems and geochemical laboratory
716 support through NCRIS AuScope and NSW Government Research Attraction and
717 Acceleration Program grants. This study used instrumentation funded by ARC LIEF and DEST
718 Systemic Infrastructure Grants, Macquarie University and industry. We especially thank
719 Manal Bebbington for her dedication to the preparation of difficult samples for in-situ
720 analysis, over many years, and Luca Bindi and Fernando Camara their encouragement and
721 incisive comments on earlier versions of the manuscript. The authors acknowledge the
722 scientific and technical assistance of Microscopy Australia at the Centre for Microscopy,
723 Characterization and Analysis, a facility funded by The University of Western Australia, and
724 State and Commonwealth Governments. This is contribution xxx from the ARC Centre of

Excellence for Core to Crust Fluid Systems (www.ccfs.mq.edu.au) and xxx from the GEMOC Key Centre (www.gemoc.mq.edu.au).

References

Uncategorized References

Apter, D.B., (2014). High pressure indicator minerals from the Rakefet magmatic complex (RMC), Mt.Carmel, Israel, Kimberley Diamond Symposium, Kimberley, South Africa.

Ben-Avraham, Z., Hall, J.K., (1977). Geophysical survey of Mount Carmel structure and its extension into the eastern Mediterranean. Journal of Geophysical Research, 82(5): 793-802.

Bindi, L., Cámara, F., Huang, J.-X., O'Reilly, S.Y., Griffin, W.L., Gain, S.E.M., Toledo, V., (2019). Discovery of the first natural hydride. American Mineralogist, 104(4): 611-614.

Chaikovskii, I.I., Korotchenkova, O.V., (2012). Explosive mineral phases of diamondiferous pyroclastites of Western Urals. Lithosphere, 2: 125-140 (in Russian).

Corgne, A., Keshav, S., Wood, B.J., McDonough, W.F., Fei, Y., (2008). Metal–silicate partitioning and constraints on core composition and oxygen fugacity during Earth accretion. Geochimica et Cosmochimica Acta, 72(2): 574-589.

Di Pierro, S., Gnos, E., Grobety, B.H., Armbruster, T., Bernasconi, S.M., Ulmer, P., (2003). Rock-forming moissanite (natural α-silicon carbide). American Mineralogist, 88(11-12): 1817-1821.

Esperança, S., Garfunkel, Z., (1986). Ultramafic xenoliths from the Mt. Carmel area (Karem Maharal Volcano), Israel. Lithos, 19(1): 43-49.

Frost, D.J., McCammon, C.A., (2008). The Redox State of Earth's Mantle. Annual Review of Earth and Planetary Sciences, 36: 389-420.

Fukai, Y., (2006). The metal-hydrogen system: basic bulk properties, 21. Springer Science & Business Media.

Garfunkel, Z., (1989). Tectonic setting of phaneroozoic magmatism in Israel. Israel journal of earth-sciences, 38(2-4): 51-74.

Gessmann, C.K., Wood, B.J., Rubie, D.C., Kilburn, M.R., (2001). Solubility of silicon in liquid metal at high pressure: implications for the composition of the Earth's core. Earth and Planetary Science Letters, 184(2): 367-376.

Goldsmith, J.R., (1980). The melting and breakdown reactions of anorthite at high pressures and temperatures. American Mineralogist, 65(3-4): 272-284.

Griffin, W., Gain, S., Adams, D., Huang, J., Saunders, M., Toledo, V., Pearson, N., O'Reilly, S., (2016a). First terrestrial occurrence of tistarite (Ti2O3): Ultra-low oxygen fugacity in the upper mantle beneath Mount Carmel, Israel. Geology: G37910. 37911.

Griffin, W., Gain, S., Huang, J., Saunders, M., Shaw, J., Toledo, V., O'Reilly, S., (2019a). A terrestrial magmatic hibonite-grossite-vanadium assemblage: Desilication and extreme reduction in a volcanic plumbing system, Mt Carmel, Israel. American Mineralogist, 104: 207-219.

Griffin, W., Howell, D., Gonzalez-Jimenez, J., Xiong, Q., O'Reilly, S., (2018a). Comment on "Ultra-high pressure and ultra-reduced minerals in ophiolites may form by lightning strikes". Geochemical Perspectives Letters, 7: 1-2.

Griffin, W.L., Afonso, J.C., Belousova, E.A., Gain, S.E., Gong, X.-H., Gonzalez-Jimenez, J.M., Howell, D., Huang, J.-X., McGowan, N., Pearson, N., (2016b). Mantle recycling: Transition zone metamorphism of Tibetan ophiolitic peridotites and its tectonic implications. Journal of Petrology, 57(4): 655-684.

Griffin, W.L., Gain, S.E., Saunders, M., Bindi, L., Alard, O., Toledo, V., O'Reilly, S.Y., (2020a). Parageneses of TiB2 in corundum xenoliths from Mt. Carmel, Israel: Siderophile behavior of boron under reducing conditions. American Mineralogist, 105(11): 1609-1621.

Griffin, W.L., Gain, S.E.M., Bindi, L., Toledo, V., Cámara, F., Saunders, M., O'Reilly, S.Y., (2018b). Carmeltazite, ZrAl2Ti4O11, a New Mineral Trapped in Corundum from Volcanic Rocks of Mt Carmel, Northern Israel. Minerals, 8(12): 601.

Griffin, W.L., Gain, S.E.M., Cámara, F., Bindi, L., Shaw, J., Alard, O., Saunders, M., Huang, J.X., Toledo, V., O'Reilly, S.Y., (2020b). Extreme reduction: Mantle-derived oxide xenoliths from a hydrogen-rich environment. Lithos, 358-359: 105404.

Griffin, W.L., Gain, S.E.M., Camara, F., Bindi, L., Sparta, D., Toledo, V., O''Reilly, S.Y., (2020c). Cr2O3 in Corundum: Ultra-high contents under reducing conditions. American Mineralogist (In press).

Griffin, W.L., Gain, S.E.M., Huang, J.X., Belousova, E.A., Toledo, V., O'Reilly, S.Y., (2018c). Permian to quaternary magmatism beneath the Mt Carmel area, Israel: Zircons from volcanic rocks and associated alluvial deposits. Lithos, 314-315: 307-322.

Griffin, W.L., Huang, J.-X., Thomassot, E., Gain, S.E.M., Toledo, V., O'Reilly, S.Y., (2018d). Super-reducing conditions in ancient and modern volcanic systems: sources and behaviour of carbon-rich fluids in the lithospheric mantle. Mineralogy and Petrology, 112(1): 101-114.

Griffin, W.L., Toledo, V., O'Reilly, S.Y., (2019b). Discussion of "Enigmatic super-reduced phases in corundum from natural rocks: Possible contamination from artificial abrasive materials or metallurgical slags" by Litasov et al. (Lithos, 340–341, p.181–190). Lithos, 348-349: 105122.

Gu, T., Stagno, V., Fei, Y., (2019). Partition coefficient of phosphorus between liquid metal and silicate melt with implications for the Martian magma ocean. Physics of the Earth and Planetary Interiors, 295: 106298.

Gvirtzman, G., Klang, A., Rotstein, Y., (1990). Early Jurassic shield volcano below Mount Carmel: new interpretation of the magnetic and gravity anomalies and implication for Early Jurassic rifting. Israel journal of earth-sciences, 39(2/4): 149-159.

Hiltl, M., Bauer, F., Ernstson, K., Mayer, W., Neumair, A., Rappenglück, M., (2011). SEM and TEM Analyses of Minerals Xifengite, Gupeiite, Fe2Si (Hapkeite?), Titanium Carbide (TiC) and Cubic Moissanite (SiC) from the Subsoil in the Alpine Foreland: Are they Cosmochemical?, Lunar and Planetary Science Conference, pp. 1391.

Huang, J.-X., Xiong, Q., Gain, S.E.M., Griffin, W.L., Murphy, T.D., Shiryaev, A.A., Li, L., Toledo, V., Tomshin, M.D., O'Reilly, S.Y., (2020). Immiscible metallic melts in the deep Earth: clues from moissanite (SiC) in volcanic rocks. Science Bulletin, 65(17): 1479-1488.

Ishimaru, S., Arai, S., Shukuno, H., (2009). Metal-saturated peridotite in the mantle wedge inferred from metal-bearing peridotite xenoliths from Avacha volcano, Kamchatka. Earth and Planetary Science Letters, 284(3–4): 352-360.

Kaminchik, J., Segev, A., Katzir, Y., (2014). The origin of intraplate alkaline mafic magmatism in continental shelves: lavas and xenoliths from the Upper Cretaceous volcanos of Mt Carmel. Unpublished MSc thesis, Beer Sheva University, Israel.

Kawanishi, S., Yoshikawa, T., Tanaka, T., (2009). Equilibrium phase relationship between SiC and a liquid phase in the Fe-Si-C system at 1523–1723 K. Materials Transactions, 50(4): 806-813.

Laws, E.D., Wilson, M., (1997). Tectonics and magmatism associated with Mesozoic passive continental margin development in the Middle East. Journal of the Geological Society, 154(3): 459-464.

Litasov, K.D., Bekker, T.B., Kagi, H., (2019a). Reply to the discussion of "Enigmatic super-reduced phases in corundum from natural rocks: Possible contamination from artificial abrasive materials or metallurgical slags" by Litasov et al. (Lithos, v.340–341, p.181–190) by W.L. Griffin, V. Toledo and S.Y. O'Reilly. Lithos, 348-349: 105170.

Litasov, K.D., Kagi, H., Bekker, T.B., (2019b). Enigmatic super-reduced phases in corundum from natural rocks: Possible contamination from artificial abrasive materials or metallurgical slags. Lithos, 340-341: 181-190.

Liu, Y., He, D., Gao, C., Foley, S., Gao, S., Hu, Z., Zong, K., Chen, H., (2015). First direct evidence of sedimentary carbonate recycling in subduction-related xenoliths. Scientific Reports, 5: 11547.

Mittlefehldt, D.W., (1986). Petrology of high pressure clinopyroxenite series xenoliths, Mount Carmel, Israel. Contributions to Mineralogy and Petrology, 94(2): 245-252.

Nakamura-Messenger, K., Clemett, S.J., Rubin, A.E., Choi, B.-G., Zhang, S., Rahman, Z., Oikawa, K., Keller, L.P., (2012). Wassonite: A new titanium monosulfide mineral in the Yamato 691 enstatite chondrite. American Mineralogist, 97(5-6): 807-815.

Ohtani, H., Hanaya, N., Hasebe, M., Teraoka, S.-i., Abe, M., (2006). Thermodynamic analysis of the Fe–Ti–P ternary system by incorporating first-principles calculations into the CALPHAD approach. Computer Coupling of Phase Diagrams and Thermochemistry, 30: 147-158.

Oliveira, B., Griffin, W.L., Gain, S.E.M., Saunders, M., Shaw, J., Toledo, V., Afonso, J.C., O'Reilly, S.Y., (2020). Ti3+ in corundum: tracing crystal growth in a higbly reduced magma. Scientific Reports (In Press).

Ottonello, G., Attene, M., Ameglio, D., Belmonte, D., Zuccolini, M.V., Natali, M., (2013). Thermodynamic investigation of the CaO–Al2O3–SiO2 system at high P and T through polymer chemistry and convex-hull techniques. Chemical Geology, 346: 81-92.

Pujol-Solà, N., Proenza, J.A., Garcia-Casco, A., González-Jiménez, J.M., Andreazini, A., Melgarejo, J.C., Gervilla, F., (2018). An alternative scenario on the origin of ultra-high pressure (UHP) and super-reduced (SuR) minerals in ophiolitic chromitites: A case study from the Mercedita deposit (eastern Cuba). Minerals, 8(10): 433.

Putter, R., Steenstra, E., Seegers, A., Lin, Y., Matveev, S., Berndt, J., Rai, N., Klemme, S., van Westrenen, W., (2017). Effects of fO2 and Si on Metal-Silicate Partitioning of Refractory and Moderately Volatile Siderophile Elements: Implications for the Si Content of Mercury's Core. LPI(1964): 1055.

Sass, E., (1980). Late Cretaceous volcanism in Mount Carmel, Israel. Israel Journal of Earth Sciences, 29(1-2): 8-24.

Schmidt, M., Gao, C., Golubkova, A., Rohrbach, A., Connolly, J., (2014). Natural moissanite (SiC) – a low temperature mineral formed from highly fractionated ultra-reducing COH-fluids. Progress in Earth and Planetary Science, 1: 1-14.

Segev, A., (2005). Phanerozoic Magmatic Activity Associated with Vertical Motions in Israel and the Adjacent Countries. In: Hall, J.K., Krasheninnikov, V.A., Hirsch, F., Benjamini, C., Flexer, A. (Eds.), Geological Framework of the Levant Vol II the Levantine Basin and Israel, pp. 553-574.

Segev, A., Rybakov, M., (2011). History of faulting and magmatism in the Galilee (Israel) and across the Levant continental margin inferred from potential field data. Journal of Geodynamics, 51(4): 264-284.

Shiryaev, A.A., Griffin, W.L., Stoyanov, E., (2011). Moissanite (SiC) from kimberlites: Polytypes, trace elements, inclusions and speculations on origin. Lithos, 122(3-4): 152-164.

Sinmyo, R., Hirose, K., Ohishi, Y., (2019). Melting curve of iron to 290 GPa determined in a resistance-heated diamond-anvil cell. Earth and Planetary Science Letters, 510: 45-52.

Steenstra, E.S., Sitabi, A.B., Lin, Y.H., Rai, N., Knibbe, J.S., Berndt, J., Matveev, S., van Westrenen, W., (2017). The effect of melt composition on metal-silicate partitioning of siderophile elements and constraints on core formation in the angrite parent body. Geochimica et Cosmochimica Acta, 212: 62-83.

Stein, F., Palm, M., Sauthoff, G., (2005). Structure and stability of Laves phases part II—structure type variations in binary and ternary systems. Intermetallics, 13(10): 1056-1074.

Stein, M., Hofmann, A.W., (1992). Fossil plume head beneath the Arabian lithosphere? Earth and Planetary Science Letters, 114(1): 193-209.

Stein, M., Hofmann, A.W., (1994). Mantle plumes and episodic crustal growth. Nature, 372(6501): 63-68.

Takahashi, S., Ohtani, E., Terasaki, H., Ito, Y., Shibazaki, Y., Ishii, M., Funakoshi, K.-i., Higo, Y., (2013). Phase relations in the carbon-saturated C–Mg–Fe–Si–O system and C and Si solubility in liquid Fe at high pressure and temperature: implications for planetary interiors. Physics and Chemistry of Minerals, 40(8): 647-657.

Tatarintsev, V., Sandomirskaya, S., Tsumbal, S., (1987). First discovery of titanium nitride (osbornite) in terrestrial rocks, Dokl Russ Akad Nauk, pp. 1458-1461 (in Russian).

Toledo, V., Griffin, W.L., Gain, S., O''Reilly, S.Y., Jacob, D., Pearson, N.J., (2015). Corundum, moissanite and super-reducing conditions in the upper mantle beneath the Lower (southern) Galilee (Israel), Abstracts Israel Geological Society Meeting, P145.

Ulmer, G., Grandstaff, D., Woermann, E., Gobbels, M., Schonitz, M., Woodland, A.B., (1998). The redox stability of moissanite (SiC) compared with metal-metal oxide buffers at 1773 K and at pressures up to 90 kbar. Neues Jahrbuch Mineralogie, Abhandlungen, 172: 279-307.

Vander Kaaden, K.E., McCubbin, F.M., Ross, D.K., Draper, D.S., (2017). The role of carbon in core formation under highly reducing conditions with implications for the planet mercury, Lunar and Planetary Science Conference.

Weitzer, F., Schuster, J.C., Naka, M., Stein, F., Palm, M., (2008). On the reaction scheme and liquidus surface in the ternary system Fe–Si–Ti. Intermetallics, 16(2): 273-282.

Xiong, F., Xu, X., Mugnaioli, E., Gemmi, M., Wirth, R., Grew, E.S., Robinson, P.T., Yang, J., (2020). Two new minerals, badengzhuite, TiP, and zhiqinite, TiSi2, from the Cr-11 chromitite orebody, Luobusa ophiolite, Tibet, China: is this evidence for super-reduced mantle-derived fluids? Eur. J. Mineral., 32(6): 557-574.

Xiong, Q., Griffin, W.L., Huang, J.-X., Gain, S.E.M., Toledo, V., Pearson, N.J., O'reilly, S.Y., (2017). Super-reduced mineral assemblages in "ophiolitic" chromitites and peridotites: the view from Mount Carmel. European Journal of Mineralogy, 29(4): 557-570.

Xu, X., Yang, J., Robinson, P.T., Xiong, F., Ba, D., Guo, G., (2015). Origin of ultrahigh pressure and highly reduced minerals in podiform chromitites and associated mantle peridotites of the Luobusa ophiolite, Tibet. Gondwana Research, 27(2): 686-700.

Yang, J., Meng, F., Xu, X., Robinson, P.T., Dilek, Y., Makeyev, A.B., Wirth, R., Wiedenbeck, M., Cliff, J., (2015). Diamonds, native elements and metal alloys from

chromitites of the Ray-Iz ophiolite of the Polar Urals. Gondwana Research, 27: 459-485.

Yatsenko, G.M., Gurskii, D.S., Slivko, E.M., (2002). Diamondiferous formations and structures of south-west frame of East-European Platform. In Minerageny of diamond. UkrGGRI, Kiev, 331 pp.

Yatsenko, I.G., (2016). Silicate-metal spherules from explosive-sedimentary diamondiferous formations (genetic and prospect aspects). PhD Autoreferat Thesis, Lviv State University, 280 pp.

Yatsenko, I.G., Skublov, S.G., Bilyk, N.T., Poberezhskaya, I.V., (2017). Inclusions in mantle corundum: Osbornite (TiN), silicides, native Iron, Proceedings of 200th Anniversary Meeting of the Russian Mineralogical Society, Saint Petersburg, Russia, Vol 1, P364-366, pp. 364-366.

Yaxley, G.M., Berry, A.J., Kamenetsky, V.S., Woodland, A.B., Golovin, A.V., (2012). An oxygen fugacity profile through the Siberian Craton — Fe K-edge XANES determinations of Fe3+/∑Fe in garnets in peridotite xenoliths from the Udachnaya East kimberlite. Lithos, 140–141: 142-151.

Yu, Z., (1984). Two new minerals gupeiite and xifengite in cosmic dusts from Yanshan. Acta Petrologica Mineralogica et Analytica, 3(3): 230-237 (in Chinese with English abstract).

Zhan, Y., Jiang, J., Sun, Z., Ma, J., Li, C., Hu, Z., (2009). Phase equilibria of the Zr–Ti–Si ternary system at 773K. Journal of Alloys and Compounds, 475: 131-133.

Zhang, R.Y., Yang, J.-S., Ernst, W.G., Jahn, B.-M., Iizuka, Y., Guo, G.-L., (2016). Discovery of in situ super-reducing, ultrahigh-pressure phases in the Luobusa ophiolitic chromitites, Tibet: New insights into the deep upper mantle and mantle transition zone. American Mineralogist, 101(6): 1285-1294.

Figure Captions

Figure 1. Cathodoluminescence (CL) images showing skeletal/hopper forms of corundum crystals in the NGC aggregates. The true colour in the lighter portions would be red to pink; darker tones correlate with higher Ti contents. (a) cross section of a hopper/skeletal corundum crystal; (b) section subparallel to growth direction showing aggregate structure and oriented growth; note zoning of crystals and skeletal structure in cores of grains.

Figure 2. FE-SEM image of sphere of native Fe^0, rimmed by $TiAl_2O_5$, in a Ca-Al-Si oxide glass that has crystallized tistarite (Ti_2O_3). The tiny bright needles are a Ti-Zr oxide phase. The microstructures suggest that the Fe^0 melt was immiscible in the Ca-Al-Si oxide melt, but in equilibrium with $TiAl_2O_5$ that was crystallizing from the oxide melt.

Figure 3. (a) Ball and irregular masses of FeTiSi, enclosed in corundum (Crn), surrounded by Ca-Al-Mg silicate glass and rimmed by an unknown oxide $MgTi_2Al_4(Si,Zr)O_{10}$ intergrown with carmeltazite (Ctz), TiS and Ti(N,O). (b) TEM-HAADF image of foil across boundary between

FeTiSi and $MgTi_2Al_4(Si,Zr)O_{10}$ along white line in (a). Note euhedral crystal of TiB_2 (zoned in Ti) in silicide, and TiS and an amorphous Ca phase along the boundary. (c) The FeTiSi (bulk composition) appears to be unmixing into three distinct phases.

Figure 4. Fe_3Si-TiC relationships. (a) BSE image of pool of Fe_3Si (white) trapped between euhedral crystals of corundum (Crn, dark). Grey areas are both TiC and Ti_3C (fcc, a = 0.25nm); note euhedral crystal outlines. The microstructures suggest that growing corundum crystals trapped and overgrew early TiC crystals, while expelling the more mobile Fe_3Si melt into smaller interstitial pockets. (b) Element maps of the area outlined in (a). (c) TEM-HAADF image across Fe_3Si-Ti_3C contact (red line in (a), showing an intermediate zone of $(Zr, Ti)_2P$. Dark curved line is a vein of vesicular amorphous carbon.

Figure 5. BSE image: Grain of Fe_3Si in corundum (Crn) with exsolved or included blebs of $(Fe,Ti)_2Si$ and $(Fe,Ti)_3Si$, surrounded by grains of Ti(N,O) and TiB_2. Straight edges on parts of the Fe_3Si suggest crystal forms.

Figure 6. FE-SEM BSE image: Fe_5Si_3 enclosed in a pocket of CaO-Al_2O_3-SiO_2 glass in corundum, together with carmeltazite, TiN and TiC.

Figure 7. FE-SEM BSE images. (a) Composite inclusion of FeTiSi and $(Fe,Ti)_2(Si,P)$ that appears to have crystallized Mg-Al spinel, TiC and an unknown phase $(Ca,Mg,Fe)_2(Al,Ti)_{10}O_{17}$. In an adjacent inclusion the assemblage is the unknown phase + carmeltazite + Ca-Al-Mg oxide glass. (b) Another inclusion in the same grain of corundum shows wavy contacts between spinel and FeTiSi and $(Fe,Ti)_2(Si,P)$; the spinel has inclusions of TiC and FeTiSi.

Figure 8. Silicide-phosphide relationships. (a) Phase map and element maps showing rhombohedral crystals and irregular blebs of $(Fe,Ti)_3(Si,P)$ in an interstitial grain of $(Fe,Ti)_2Si$. High-Ti rim on the silicide grain comprises crystals of TiC. (b) TEM-HAADF image and element maps of the zoned euhedral grain of $(Fe,Ti)_3(Si,P)$ in the silicide grain shown in Figure 6a.

Figure 9. (a) BSE image of Fe_5Si_3 in the core of an alloy inclusion in corundum; exsolved blebs are $(Fe,Ti)_2(Si,P)$ and $(Fe,Ti)_{11}Si_5$. (b) BSE image, phase map and element maps showing vermicular areas of $(Fe,Ti)_5(Si,P_2)$ in composite interstitial grain of $(Fe,Ti)_3Si$ and $(Fe,Ti)_3Si_2$.

Figure 10. Immiscible silicide-phosphide melt? (a) BSE image of bright porous (?) spheres of Fe-Ti-Zr silicides and phosphides in pocket of CaO-SiO_2-Al_2O_3 glass enclosed in hibonite; crystalline phases are Mg-Al-V spinel and hibonite ($CaAl_{12}O_{19}$). (b) enlargement showing crystalline structure, and apparent voids. Red line in (a) shows trace of FIB foil. (c) TEM-HAADF image and element maps of the ball, a granular intergrowth of (1),$(Zr,Ti,U)_5(P,Si)_3$; (2), $(Ti,Zr,Fe)Si_2$; (3), $(Ti,Zr)_3Si_7$.

Figure 11. (a) FE-SEM BSE images showing relationships among Zr-Ti phosphides and TiC. (b) 30-µm inclusion in corundum, with large crystal of SiC, and blobs of Zr-Ti-Si-P phases, in a matrix of $(Ti,Zr)Si_2$. Red line marks location of TEM FIB foil shown in (c) and (d). (c) TEM-HAADF image and (d) element maps across the silicide-phosphide boundary, showing a fluidal contact between Zr-Ti phosphide and Ti silicide. Note grain of $(Zr,Ti,U)_5(P,Si)_3$ among silicide crystals.

Figure 12. (a) BSE image of a melt inclusion in corundum, containing a large crystal of TiC and a lath-shaped crystal of Ti_3SiC_2 in a matrix of Fe-Ti silicides. Note rim on Ti_3SiC_2 crystal. (b) and (c), TEM-HAADF images of FIB foil taken along red line in (b). The rim on the Ti_3SiC_2 crystal is a mixture of euhedral SiC crystals (dark in Ti map below) and $Ti_{1-x}Si_{2+x}$. SiC crystals are smaller adjacent to corundum host; light spots in $Ti_{1-x}Si_{2+x}$ are Ti_3SiC_2. Lower panel: element maps of the area shown in (b). After Huang et al. (2020).

Figure 13. Fe-Ti-Si system at 1 atm pressure, after Weitzer et al. (2008). (a) Liquidus projection with analyses of individual alloy grains shown by points. Fields are labelled with the phase that crystallizes first from a melt in that field. For purposes of plotting, minor Mn and Ni are grouped with Fe; minor V, Cr and Al are grouped with Ti, and minor P is grouped with Si. Stars, inclusions in SiC, from Huang et al. (2020); b) Isothermal section at 900-1000 °C, plotted as described for (a). Tie lines represent coexisting phases; grey areas are fields of

solid solution. Enclosed numbered fields show clusters of points described in the text. (c) As in (a), with important points on the liquidus surface labelled with temperature in °C.

Figure 14. BSE images: Unmixing of Fe-Ti-Si-P melts. (a) Light phase is $FeSi_3$, dark phase is $(Fe,Ti)_2(Si,P)$. See Table 1 for analytical data. (b) intergrowth of TiC, FeTi(Si,P) and two Fe-Ti-(Cr-V) silicides. Both grains are included in corundum.

Figure 15. Ternary plots showing compositions of Zr-Ti-Si-P phases. Subsolidus fields in (a) and (b) are from Oliynyk et al. (2012) at 800 °C and Colinet and Tedenac (2012) at 1050 °C, respectively. Numbered populations correspond to clusters in Table 1.

Figure 16. Analytical data and subsolidus phase relationships in the Fe-Ti-Si system at 1150 °C.

Figure 17. Tie lines between apparently coexisting phases in several melt pockets, plotted on the subsolidus phase diagram at 900-1000 °C and 1 atm. Green lines correspond to possible subsolidus equilibria. Red tie lines cross the tie-lines between subsolidus phases, and probably connect mutually immiscible liquids, or a liquid and a solid phase.

Figure 18. Phase relations in Fe-Si-Ti-C system. (a) Ti-Si-C at 1200 °C, 1 atm and >0.25 GPa, after Sambasivana and Petuskey (1992); (b) Fe-Si-C liquidus showing compositions of coexisting phases; 1450 °C compositions (red stars) after Huang et al. (2020). Red-shaded fields show observed three-phase assemblages.

Figure 19. Compositions of reconstituted melts, plotted on the Fe-Ti-Si liquidus diagram. Red circles in upper half of the plot are reconstructed melt inclusions in SiC crystals (Huang et al., 2020).

Figure 20. Experimental solubility of Si in Fe melts, as a function of P, T and fO_2 (after Gessmann et al., 2001). Star indicates maximum observed Si content in Mt Carmel Fe melts (8%) at its estimated T, showing the very low fO_2 required to stabilize this composition.

Figure 21. Schematic evolution of the melts by repeated immiscibility and fractional crystallization. The initial melt is shown as "syenitic" in origin; it is suggested that these melts had differentiated from basaltic precursors within the crust-mantle underplate, producing more felsic starting points for the proposed evolution. Circled numbers mark stages of immiscibility discussed in the text.

Supplementary Data

Figure SD1. Location maps. (a) structural framework of the Levant-Sinai region; red box marks area of (b) Geological framework of northern Israel, showing the location of Cretaceous magmatic centers in the Mt Carmel area.

Figure SD2. (a) 2-mm crystal of corundum showing depressed faces typical of hopper growth; (b) section of a grain of Carmel Sapphire, showing the 3D network of melt pockets around and within skeletal/hopper crystals. After Xiong et al., 2017; (c) 3D-μCT image of a fragment of Carmel Sapphire ca 2 mm across. Colours correspond to silicate melts (orange), metallic melts (white) and voids, presumably fluid-filled (green). Black areas are corundum.

Appendix: Sampling and Methods

Table 1 — Fe-Ti Silicides

Number	0		1		2		3		4		5		6		7	
Phase	Fe		Fe_3Si_2		$(Ti,Fe)_5Si_3$		Fe Ti Si_2		$(Fe,Ti)_5Si_2$		$(Fe,Ti)_5Si_3$		Fe_3Si_2		Fe$_2$Si	
mineral	native iron						zangboite				xifengite		perryite analog		gupeiite	
interpretation	melts		melt incl in SiC		liquidus		liquidus ↔ in Weitzer		melts		subsolidus		subsolidus		liquidus	
analysis	EMP		*SEM-EDS*		*SEM-EDS*		*SEM-EDS*	*EMP*	*SEM-EDS*	*EMP*	*SEM-EDS*	*EMP*	*SEM-EDS*	*EMP*	*SEM-EDS*	*EMP*
wt%	n=5	stdev	n=3	stdev	n=6	stdev	n=8	stdev	n=3	stdev	n=9	stdev	n=6	stdev	n=4	stdev
Si	1.99	2.19	54.7	0.8	48.6	3.4	31.9	2.6	32.2	2.4	27.7	2.3	28.6	1.9	21.8	1.6
Zr					1.1	0.8	1.9	2.2	0.1	0.1			0.2	0.1		
Ti	0.24	0.27	0.2	0.3	42.6	2.2	27.3	1.7	29.0	3.7	18.7	2.9	22.1	3.4	4.1	1.2
Al	0.08	0.02	0.2	0.2	0.4	0.2	0.7	0.8	0.1	0.1			0.6	0.7	0.3	0.2
Cr	0.26	0.23			1.4	0.5	1.3	0.5	4.2	4.7	0.8	0.2	1.5	0.9	0.5	0.4
P	0.52	0.59			0.3	0.2	0.7	0.5	0.3	0.2	0.8	1.4	0.3	0.2	0.1	0.2
V	0.02	0.01	0.2	0.4	1.7	0.4	0.7	0.3	1.1	1.0	0.6	0.1	0.8	0.2	2.0	4.2
Mg																
Fe	95.91	2.10	41.7	1.1	5.3	2.8	35.2	5.2	30.0	2.3	50.4	1.4	43.5	2.9	71.2	3.8
Mn			1.2	0.2			0.4	0.5	1.1	0.6	0.9	0.4	0.3	0.3	0.1	0.2
Ni			1.8	0.3												
C																
O																
sum	99.03		100.0		101.3		100.1		98.3	1.0	100.0		97.9	0.9	100.1	
at.%																
Si	3.84	4.15	70.6	0.7	62.2	2.8	47.6	3.1	47.2	2.5	41.9	3.3	43.5	2.2	35.8	2.0
Zr					0.5	0.4	1.1	1.0	0.1	0.0			0.1	0.1		
Ti	0.28	0.31			31.7	1.4	23.7	1.2	24.9	3.0	16.6	2.6	19.7	3.2	3.9	1.1
Al	0.15	0.03	0.3	0.2	0.5	0.3	0.7	1.2	0.1	0.1			0.9	1.0	0.5	0.4
Cr	0.28	0.25			0.9	0.3	1.1	0.4	3.4	3.9	0.7	0.2	1.2	0.7	0.5	0.3
P	0.93	0.88			0.3	0.2	1.1	0.6	0.5	0.3	1.1	2.0	0.4	0.3	0.1	0.2
V	0.02	0.01			1.0	0.5	0.5	0.3	0.9	0.9	0.5	0.1	0.6	0.1	0.2	0.2
Mg																
Fe	94.49	3.54	27.0	0.8	3.5	1.7	23.9	4.2	22.1	1.3	38.4	0.9	33.3	2.4	58.9	2.4
Mn			0.8	0.1			0.3	0.4	0.8	0.5	0.7	0.3	0.2	0.2		
Ni			1.1	0.2												
C																
O																
crystallography*																

Table 1 (cont.) — Fe-Ti Silicides

Number	8				9				10		11				12		13				14		15		
Phase	$(Fe,Cr)_3(Si,P)$				$(Fe,Ti)_3(Si,P)3$				$(Fe,Ti)_3(Si,P)$		FeTi(Si,P)				ce $FeTi_3Si_2$		$(Ti,Fe)_5Si_3$				$Ti_6(Si,P)_3$		Ti_5Si_3		
mineral	Cr-gupeiite										↔ in Weitzer				↔ in Weitzer										
interpretation	liquidus				subsolidus				liquidus?		liquidus				melt+ xls?		liquidus?				liquidus		subsolidus		
analysis	*SEM-EDS*		*EMP*		*SEM-EDS*				*SEM-EDS*		*SEM-EDS*		*EMP*		*SEM-EDS*	*EMP*	*SEM-EDS*		*EMP*		*SEM-EDS*		*SEM-EDS*		
wt%	n=7	stdev	n=13	stdev	n=3	stdev	UTAS (3)		n=5	stdev	n=6	stdev	n=16	stdev	n=12	stdev	n=5	stdev	n=4	stdev	n=3	stdev	n=3	stdev	
Si	13.8	0.9	13.78	2.1	15.2	0.4	14.60		12.8	2.5	20.0	0.4	15.7	2.9	23.8	2.1	30.5	27.4	2.6	27.1	3.7	15.4	1.40	15.55	0.88
Zr			0.01										0.1	0.1			1.14			0.4	0.5				
Ti	1.1	1.0	1.35	1.1	24.8	1.7	26.00		31.6	3.3	31.0	1.3	31.1	2.5	40.6	4.9	51.9	58.1	1.8	46.8	4.0	64.6	0.07	83.19	0.94
Al	0.4	0.2	0.69	0.9			0.2		0.2	0.1	0.1	0.2	0.1	0.1	0.1	0.2	0.08	2.0	2.1	0.1	0.0	0.3	0.6	0.5	0.1
Cr	4.6	0.8	0.95	1.4	0.3	0.2	1.3		2.3	1.7	3.9	0.6	2.7	2.8	6.5	2.6	2.24	2.9	0.3	5.0	2.8	2.3	0.1		
P	0.1	0.1	0.06	0.1	4.4	0.3	6.0		4.3	4.1	0.7	0.5	4.6	2.9	0.4	0.1	1.59	0.8	0.2	0.8	0.5	9.5	0.4	0.7	0.1
V	1.3	0.6	0.30	0.4	0.7	0.2	0.9		1.5	1.2	2.0	1.0	1.0	0.7	2.3	1.3	0.80	1.5	0.4	1.0	0.4	1.2	0.5		
Mg																									
Fe	78.8	0.7	82.81	2.7	53.9	1.4	51.5		42.8	2.5	41.2	0.8	41.1	3.2	24.2	6.9	7.93	5.5	1.9	12.2	4.7	5.2	2.0		
Mn	0.4	0.2	0.21	0.2					0.4	0.5	1.1	0.1	0.7	0.9	2.4	1.9	1.14	1.6	1.5	3.0	2.2	1.1	0.9		
Ni																									
C																									
O																									
sum	100.0		100.16		99.2		100.6		95.9		100.0		97.1	0.9	100.2		97.31	99.9		96.4	1.2	99.6		99.9	
at.%																									
Si	23.4	1.1	23.8	3.2	24.7	0.6	23.3		21.9	3.2	31.6	0.5	25.6	4.6	36.0	2.2	44.2	37.6	3.5	40.8	4.1	23.4	1.8	23.8	1.2
Zr													0.1	0.0			0.5			0.2	0.2				
Ti	0.8	0.8	1.4	1.1	23.6	1.6	24.3		31.8	13.0	28.7	1.1	29.7	2.4	35.7	3.6	44.1	49.3	3.5	41.3	3.1	55.9	0.7	74.6	1.2
Al	0.2	0.4	0.7	0.9			0.4		0.3	0.5	0.1	0.3	0.1	0.2	0.8	1.9	0.1	3.3	1.5	0.1	0.0	0.5	0.9	0.5	0.4
Cr	4.6	0.3	1.0	1.3	0.2	0.2	1.2		2.6	1.3	3.3	0.6	2.4	2.5	4.8	2.9	1.8	2.3	0.2	4.1	2.4	1.8	0.1		
P	1.0	0.9			6.5	0.4	8.7		2.6	3.2	1.0	0.8	6.9	4.3	0.3	0.3	2.1	1.0	1.5	1.1	0.7	12.7	0.6	1.0	0.2
V	0.3	0.5	0.4	0.7	0.6	0.1			1.3	0.3	1.7	1.0	0.9	0.6	2.1	1.1	0.6	1.2	0.2	0.9	0.4	1.0	0.4	0.2	0.4
Mg																									
Fe	68.8	1.4	70.4	0.8	44.0	1.1	41.3		39.5	9.2	32.7	0.9	33.7	2.7	18.6	5.1	5.8	3.5	3.0	9.2	3.5	3.9	1.5		
Mn			0.3	0.1							0.9	0.1	0.6	0.7	1.7	1.4	0.8	1.4	0.4	2.3	1.8	0.8	0.7		
Ni																									
C																									
O																									
crystallography*											Imm2 a=0.7nm, c=0.63nm														

Table 1 (cont.) — Ti Carbides

Number	16		
Phase	TiC	Ti_2C	Ti_3SiC_2
mineral	khamrabaevite		
interpretation	liquidus	liquidus	liquidus
analysis	EMP	TEM-EDS	TEM-EDS
wt%	n=18	stdev	n=1	stdev	n=1	stdev
Si			0.2	0.0	14.2	0.2
Zr	0.61	0.63	1.8	0.03	0.6	0.2
Ti	75.81	0.64	86.3	2.6	71.5	6.5
Al	0.13	0.30			0.3	0.1
Cr						
P						
V	0.87	0.16			0.3	0.1
Mg						
Fe	0.29	0.22	4.7	0.2	0.1	0.1
Mn						
Ni						
C	17.6	3.1	7.0	0.2	13.0	1.3
O	1.8	2.7				
sum	97.11		99.93		100.0	
at.%						
Si			0.26		16.2	
Zr	0.21	0.22	0.81		0.2	
Ti	48.72	1.86	72.3		48.1	
Al	0.14	0.33			0.3	
Cr						
P						
V	0.37	0.26			0.2	
Mg						
Fe	0.16	0.12	3.40		0.1	
Mn						
Ni						
C	44.93	6.65	23.20			
O	3.86	5.41				
crystallography*			FCC			

Fe-Ti Phosphides, Silicide/Phosphides

Number	17		18		19			
Phase	$(Cr,Ti,Fe)_3P$		$(Fe,Ti)_3P$		$(Fe,Ti)_3(Si,P)$			
mineral	Florenskyite?							
interpretation	liquidus?		melt?		melt?			
analysis	SEM-EDS		SEM-EDS		SEM-EDS		EMP	
wt%	n=1		n=4	stdev	n=11	stdev	n=4	stdev
Si	0.33		0.78	0.41	12.9	1.9	9.97	0.82
Zr							7.15	2.46
Ti	17.3		21.4	3.01	30.3	4.1	29.64	2.68
Al	0.2		0.2	0.1	0.2	0.3	0.13	0.17
Cr	30.4		3.2	0.5	0.9	1.6		
P	35.2		19.7	0.7	8.6	2.5	7.91	2.05
V					0.8	1.0	0.30	0.05
Mg								
Fe	11.6		53.4	2.9	46.2	3.0	41.68	1.00
Mn	0.8				0.2	0.4	0.16	0.03
Ni								
C								
O							1.06	0.41
sum	99.6		100.1		100.0		98.00	
at.%								
Si	0.5		1.3	0.8	20.1	2.8	17.14	1.47
Zr	0.0						3.81	1.40
Ti	15.0		20.6	3.3	28.6	3.4	29.87	2.87
Al	0.2		2.9	0.5	0.4	0.4	0.24	0.33
Cr	24.3		0.3	0.2	0.7	1.2		
P	47.1		29.4	1.2	12.5	3.3	12.25	2.84
V	3.0				0.7	0.8	0.28	0.05
Mg	0.1		1.2	0.2				
Fe	8.6		44.3	2.9	36.9	2.3	36.03	0.90
Mn	0.6				0.1	0.3	0.14	0.02
Ni								
C								
O								
crystallography*	6.8Å axis							

Zr-Ti Phosphides, Silicide/Phosphides

Number	20		21		22		23		24		25	
Phase	$(Zr,Ti)P$		(Zr,Ti) (P,Si)		Zr_5 Ti_5 $(Si,P)_6$		(Ti,Zr,Fe) $(Si,P)_2$		(Ti,Zr) Si_2		$TiZrSi_2$	
mineral												
interpretation	melt		melt?		?		melt?		melt?		melt?	
analysis	SEM-EDS		SEM-EDS		SEM-EDS		SEM-EDS		SEM-EDS		SEM-EDS	
wt%	n=1		n=4	stdev	n=1		n=3	stdev	n=13	stdev	n=3	stdev
Si	0.71	3.9	0.8	16.8			44.1	1.2	43.9	1.3	57.8	1.0
Zr	86.2	58.9	0.8	32.9	21.0	1.7	34.4	7.2	25.9	0.8		
Ti	5.9	11.8	1.1	37.4	24.3	0.5	19.0	4.3	13.3	0.9		
Al	0.2	0.2	0.2	0.3	0.4	0.1	0.2	0.2	0.3	0.1		
Cr	0.0	0.0		0.9	0.9	0.2			0.1	0.2		
P	26.0	24.6	1.0	10.4	1.6	0.6						
V				1.3								
Mg												
Fe	0.0	0.4	0.8		5.2	0.4	1.7	1.9	1.9	0.1		
Mn	0.0	0.0			2.5	0.2	0.5	1.0	0.5	0.4		
Ni	0.0	0.0										
C												
O												
sum	99.0	99.9		100.0	100.0		99.8		99.9			
at.%												
Si	1.5	7.5	1.4	28.0	62.0	1.2	65.4	1.0	77.0	1.9		
Zr	42.2	35.0	0.9	16.9	9.1	0.8	15.1	4.5	10.6	0.1		
Ti	7.2	13.3	1.3	36.7	20.1	0.3	17.4	4.4	10.4	0.7		
Al	0.3	0.3	0.4	0.6	0.6	0.1	0.3	0.3	0.3	0.3		
Cr				0.8	0.7	0.2						
P	48.8	43.0	1.6	15.8	2.1	0.8						
V				1.2								
Mg												
Fe					3.7	0.2	1.3	1.3	1.3	0.1		
Mn					1.8	0.1	0.4	0.7	0.3	0.3		
Ni												
C												
O												
crystallography*						Pmmm						

Table 2. TEM-EDS analyses of phases in FIB foils

Analysis	1		2		3	
	Spherical silicide-phosphide aggregates in glass (Fig. 10)					
	(Zr,Ti)3Si7		(Zr,Ti,U)5(P,Si)3		TiSi3	
	FIB A-1		FIB A-1		FIB A-1	
wt%	wt%	(3 Sigma)	wt%	(3 Sigma)	wt%	(3 Sigma)
Si	43.4	0.7	2.1	0.2	51.0	1.0
Zr	43.4	4.3	61.6	6.1	4.5	0.9
Ti	11.9	1.2	3.4	0.5	31.0	3.0
Al						
Cr					1.3	0.3
P			13.7	1.4		
V						
Fe	1.3	0.2	0.4	0.2	8.3	0.9
Mn					3.8	0.5
Nb						
C						
O						
U			18.0	5.7		
As			0.7	0.2		
S						
Pb						
at.%						
Si	67.4		5.4		65.9	
Zr	20.8		49.8		1.8	
Ti	10.8		5.3		23.5	
Al						
Cr					0.9	
P			32.6			
V						
Fe	1.0		0.5		5.4	
Mn					2.5	
Nb						
C						
O						
U			5.6			
As			0.7			
S						
Pb						

xlography | | |

3 phases in granular intergrowth xlized silicide-phosphide melt?

4		5		6		7
single inclusion in corundum -- Ti3SiC2 lath in silicides with SiC, TiC						
Ti3SiC2		**FeTiSi2**		**(Ti,Cr)2Si3**		**(Ti,Cr**
FIB A-2		FIB A-2		FIB A-2		FIB
wt%	(3 Sigma)	wt%	(3 Sigma)	wt%	(3 Sigma)	wt%
14.2	0.2	31.5	0.6	45.2	3.1	47.5
0.6	0.2	3.3	0.6			
71.5	6.5	27.7	2.6	50.9	5.8	49.2
0.3	0.1	0.2	0.1	0.4	0.4	0.3
		1.7	0.3	2.0	0.8	2.4
0.3	0.1					
0.1	0.1	35.6	3.3	1.5	0.7	0.5
13.0	1.3					
16.2		46.4		58.4		60.7
0.2		1.5		0.6		
48.1		24.0		38.6		36.9
0.3		0.3				0.5
		1.3		1.4		1.6
0.2						
0.1		26.4		1.0		0.3
34.8						

hexagonal central lath	good patttern matrix	good patttern unmixed in matrix	unmixed

Table 2 (cont.) TEM-EDS analyses of phases in

7 (Fig. 12)	8		Analysis	9		1 Fluidal m
)2 Si3	Ti1-x Si2+X			(Zr,Ti)2P		(Zr,Ti)3
A-2	FIB A-2			FIB A-3		FIB
(3 Sigma)	wt%	(3 Sigma)	wt%	wt%	(3 Sigma)	wt%
1.9	55.5	2.3	Si			1.9
			Zr	71.5	7.0	66.5
5.0	43.0	4.5	Ti	10.0	1.1	13.4
0.2			Al			
0.6	1.2	0.5	Cr			
			P	16.2	1.6	15.6
			V			
0.3	0.3	0.3	Fe	0.2	0.1	0.3
			Mn			
			Nb			
			C			
			O			
			U			
			As	1.2	0.3	1.0
			S			
			Pb	1.0	0.5	1.3
			at.%			
	68.1		Si			4.3
			Zr	50.9		45.4
	31.0		Ti	13.5		17.4
			Al			
	0.8		Cr			
			P	34.0		31.5
			V			
	0.2		Fe	0.2		0.3
			Mn			
			Nb			
			C			
			O			
			U			
			As	1.0		0.8
			S			
			Pb	0.3		0.4

in matrix	intergr w/ SiC		main phase	mixt

FIB foils

0	11		12		13	
ixture of silicides, phosphides (Fig. 11)						
(P,Si)2	(Zr,Ti)Si2		(Zr,Ti,U)5(P,Si)3		Fe3Si	
A-3	FIB A-3		FIB A-3		FIB A-4	
(3 Sigma)	wt%	(3 Sigma)	wt%	(3 Sigma)	wt%	(3 Sigma)
0.2	41.3	0.2	0.7	0.4	12.6	0.1
6.5	42.9	4.0	56.6	8.3	0.6	0.1
1.4	13.0	1.2	4.4	0.9	2.4	0.3
	0.2	0.1				
					0.3	0.1
1.6			12.9	1.8		
0.1	2.2	0.3			82.1	7.5
					2.0	0.3
			23.4	8.4		
0.3			1.0	0.6		
					0.1	0.1
0.6	0.4	0.2	1.1	0.9		
	65.0		1.9		22.2	
	20.8		48.9		0.3	
	12.0		7.2		2.5	
	0.3					
	0.1				0.3	
			32.8			
	1.7				72.8	
					1.8	
			7.8			
			1.0			
					0.1	
			0.4			

ure?	second phase, liquid	inclusion in 2nd phase	main phase

14		15		16		1
Fe3Si with unmixed phosphide phases (Fig. 9)						
Fe4Ti3(Si,P)3		**(Fe,Ti)7(Si,P)3**		**(Fe,Ti)3Si**		**(Zr,Ti)7**
FIB A-4		FIB A-4		FIB A-4		FIB
wt%	(3 Sigma)	wt%	(3 Sigma)	wt%	(3 Sigma)	wt%
11.3	0.4	13.3	0.2	13.4	0.3	
0.6	0.3	0.6	0.2	0.6	0.2	81.8
31.7	3.0	29.3	2.7	13.9	1.3	5.4
		0.1	0.1			0.2
0.2	0.1	0.3	0.1	0.2	0.1	
5.8	0.6	3.3	0.4			10.8
48.5	4.5	49.7	4.6	68.7	6.3	0.2
1.0	0.2	1.2	0.2	1.6	0.2	
0.8	0.1	1.8	0.3	1.4	0.3	
						1.4
		0.5	0.1			
18.5		22.1		23.3		
0.3		0.3		0.3		61.5
30.6		28.6		14.2		7.7
		0.1				0.4
0.2		0.2				
8.7		4.9				24.0
40.1		41.5		59.9		0.3
0.8		1.0		1.4		
0.4		0.9		0.8		
						5.9
		0.3				

adjacent phase	Core of inclusion in Fe3Si	rim of inclusion	inclusion

7		18	19	20	21	22
			Silicide-Boride relationships (Fig. 3b)			
'(P,O)3		TiB_2	Mg Silicate	silicide 1	silicide 2	TiS
A-5		n=3	n=3	$(Fe,Ti,Al)_2Si$	FeTiSi	n=3
(3 Sigma)	wt%		EMP	TEM-EDX	TEM-EDX	TEM-EDX
	Si	1.21	5	23.9	20.7	
7.5	Zr		4.32			
0.6	Ti	56.5	20.77	40.7	31.7	54.6
0.1	Al		21.29	8.3	4	
	Cr	2.1		3.2	2.3	
1.1	P			0.09	0.27	
	V	4.1				
0.1	Fe	1.31	0.02	22.6	40	
	Mn		0.03	1.2	1.1	0.7
	Mg		5.28			
	S					44.7
0.2	B	34.3				
	O		40.49			
	sum	99.5	97.2	100	100.1	100
	Si	0.95	4.24	34.04	31.7	
	Zr		1.13			
	Ti	26	10.32	34.01	28.34	48.4
	Al		18.78	12.31	6.34	
	Cr	0.89		2.46	1.89	
	P			0.12	0.37	
	V	1.77				
	Fe	0.52	0.01	16.19	30.65	
	Mn		0.01	0.87	0.86	
	Mg		5.18			
	S					51.6
	B	69.9				
	O		60.23			

ı in glass

Table 3. Reconstructed compositions of some complex melt inclusions

	41	9a	4	9b	42	44
T*	1600°C	1400 °C	1350°C	1300 °C	1200 °C	1100 °C
Si	7.8	13.6	24.6	15	19.4	17.6
Ti	33.3	17	18.7	7	8.6	9.5
Al	1.1					
Cr	0.2	0.3	2.5	3.5	0.6	0.2
P	0	2.4	0.4	0.2	2.6	1.5
V	0	0.4	0.8	0.6	0.5	0.4
Fe	48.1	65.4	52.6	71.9	67.8	70.4
Mn	0.2					
C	9.4	1.8	0.5	1.2	0.2	0.4

*estimated from Weitzer et al. (2008)

Figure 1

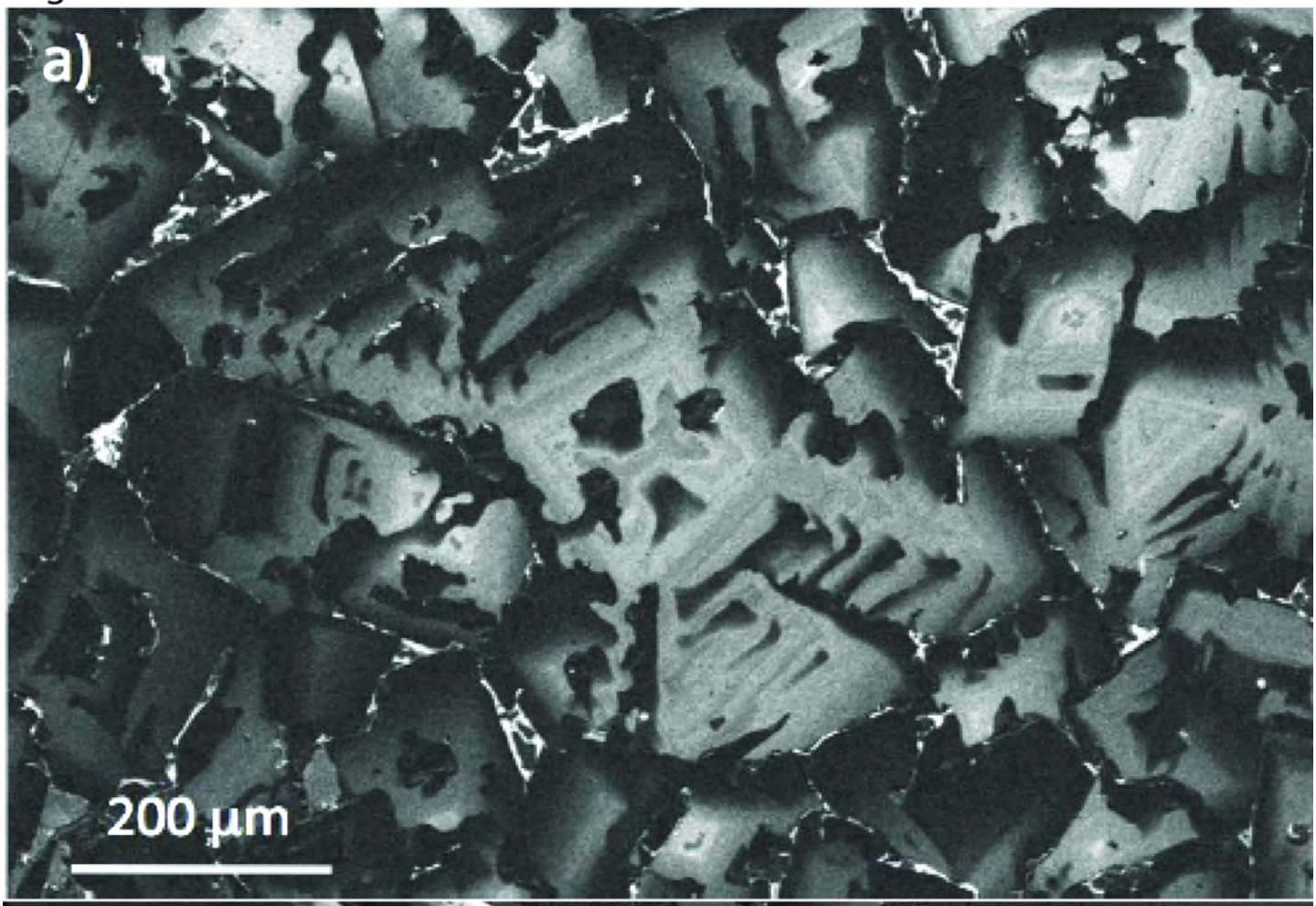

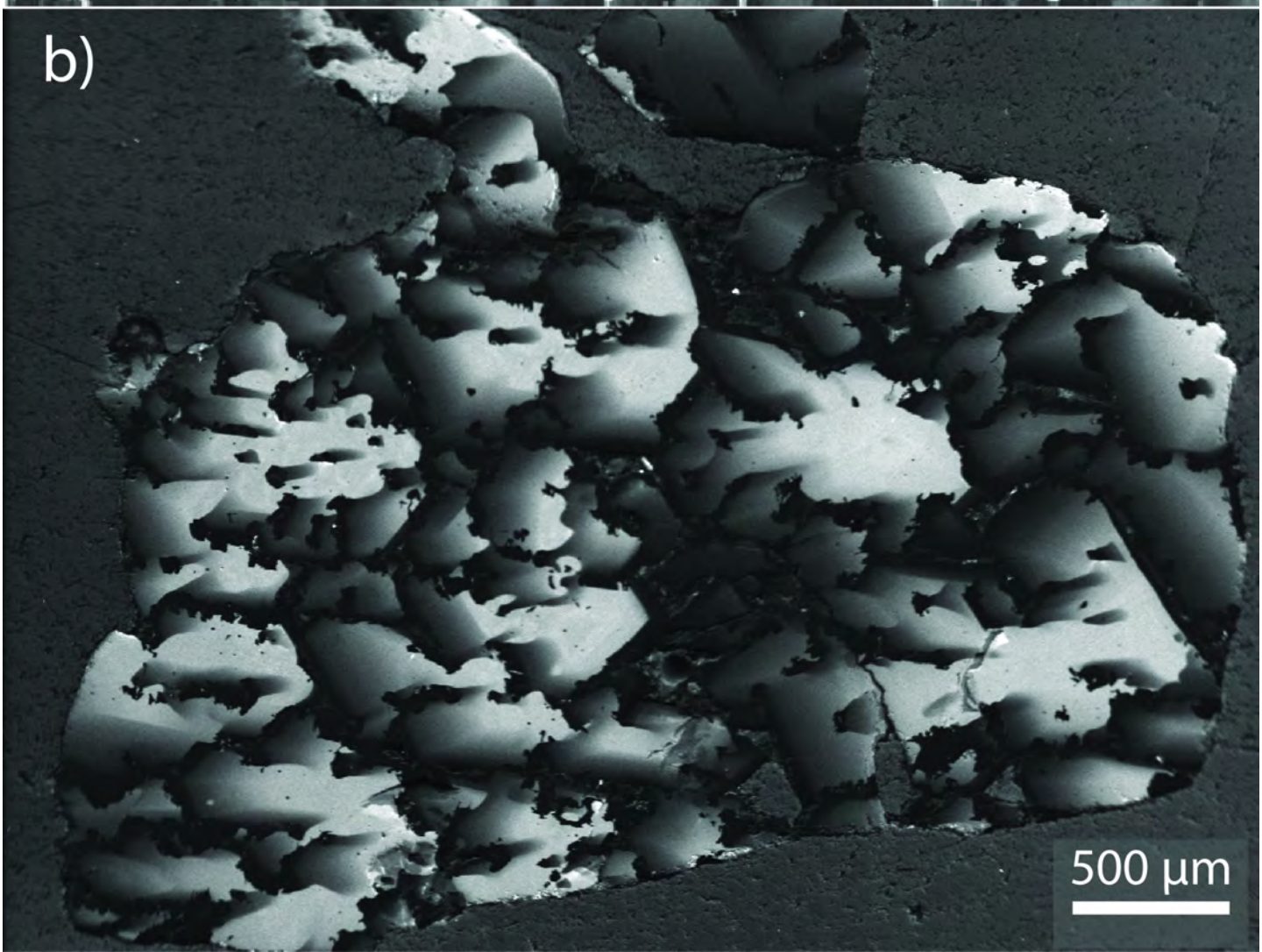

Figure 2

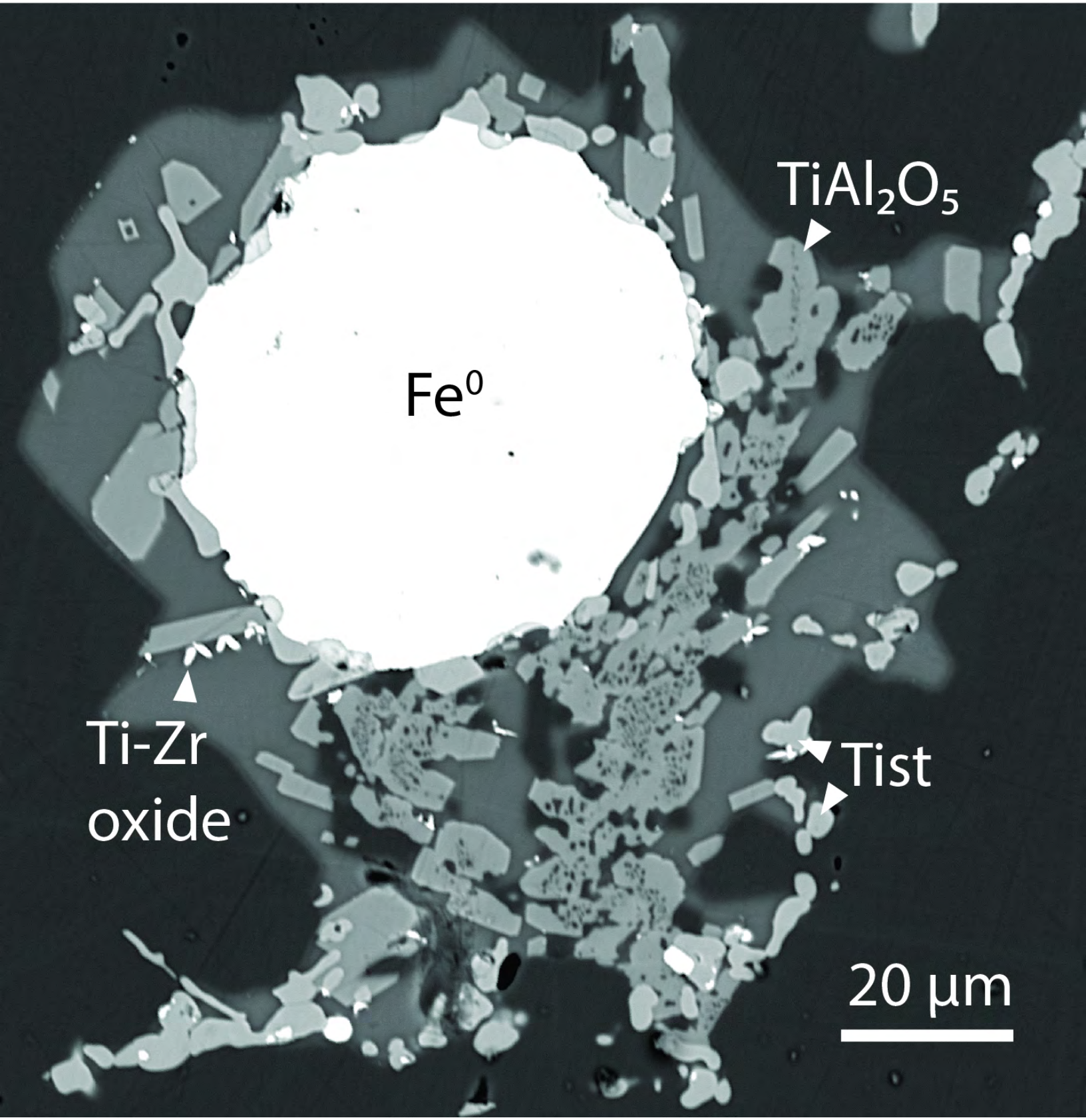

Figure 3

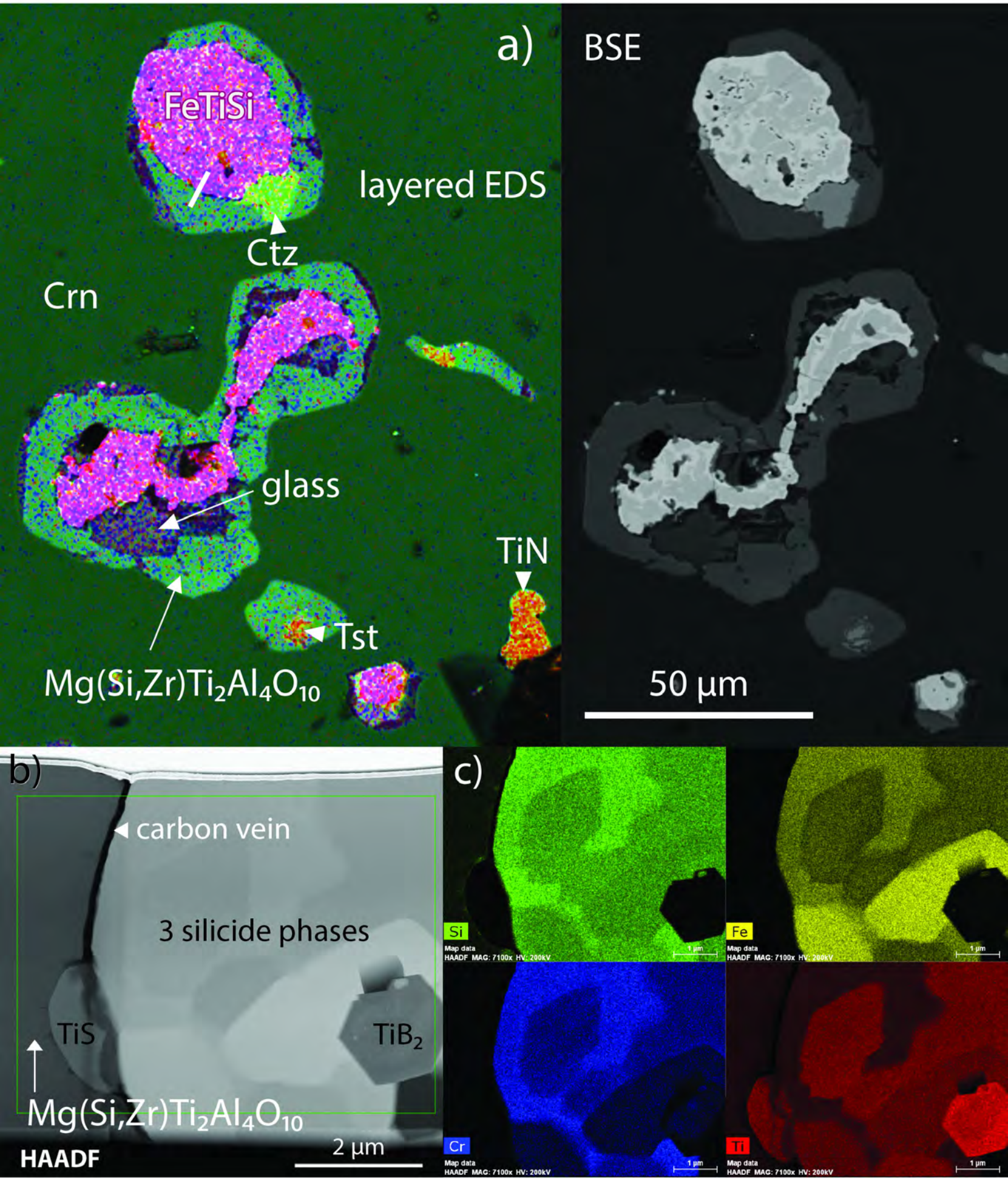
a)
FeTiSi
layered EDS
Ctz
Crn
glass
TiN
Tst
Mg(Si,Zr)Ti2Al4O10
BSE
50 µm
b)
carbon vein
3 silicide phases
TiS
TiB2
Mg(Si,Zr)Ti2Al4O10
HAADF
2 µm
c)
Si
Fe
Cr
Ti
Map data
HAADF MAG: 7100x HV: 200kV
1 µm

Figure 4

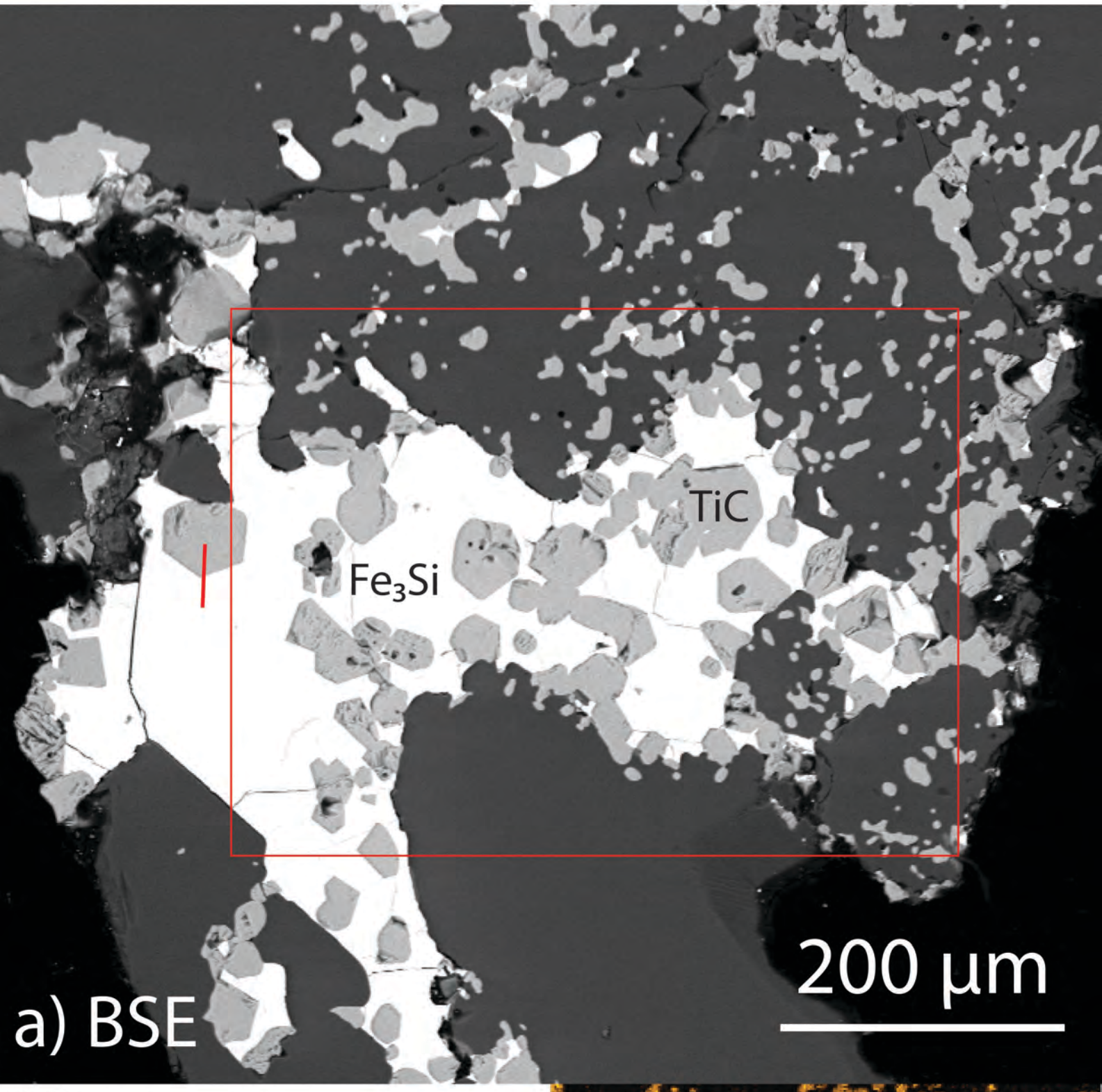

b) EDS element maps

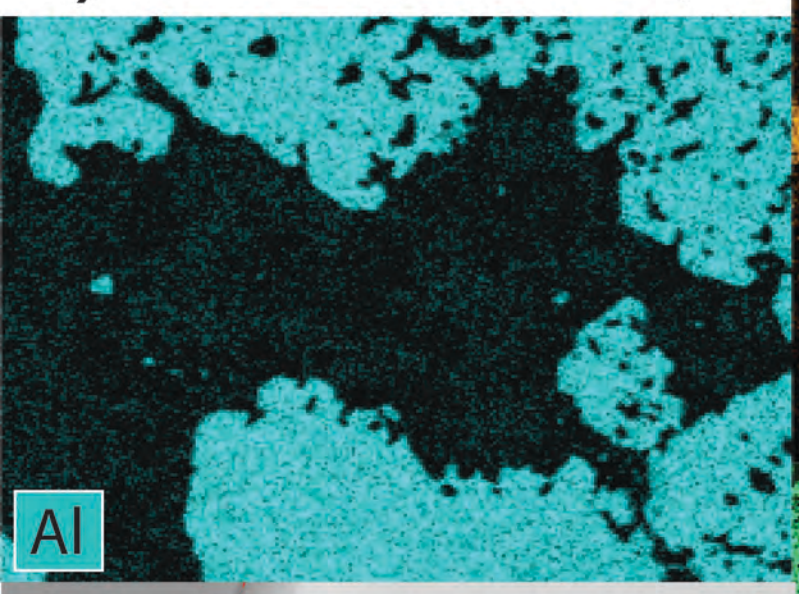

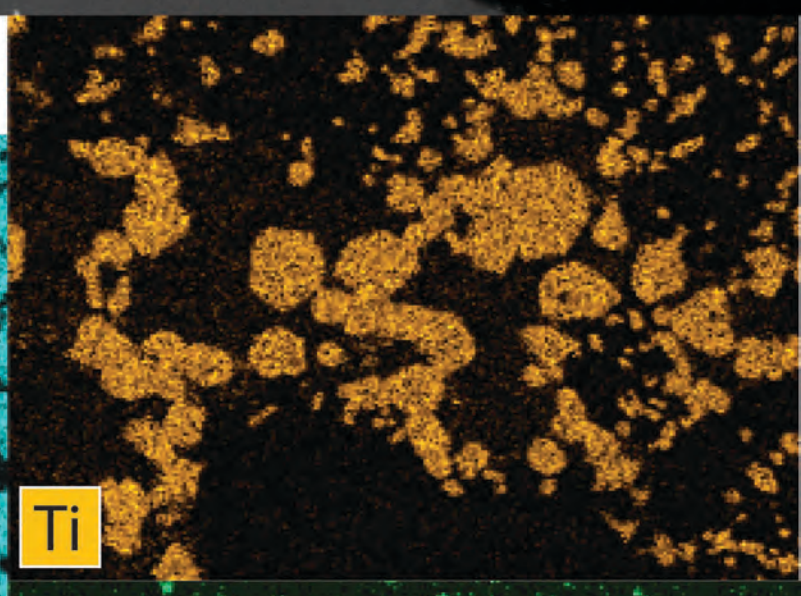

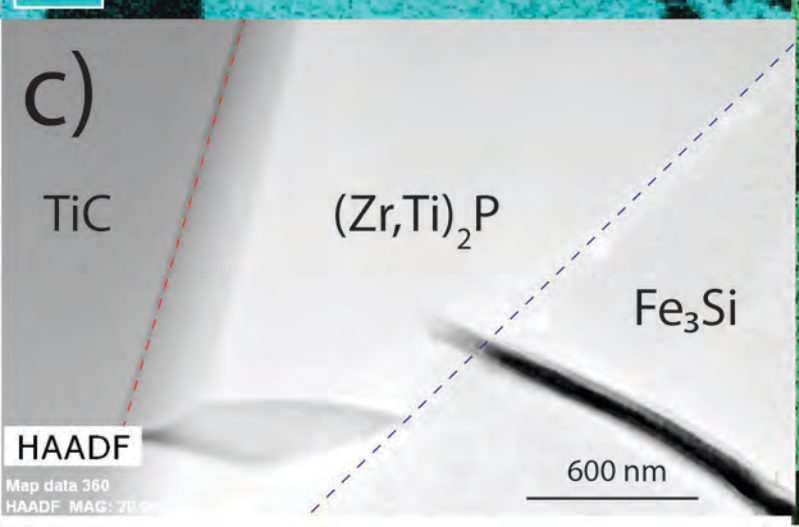

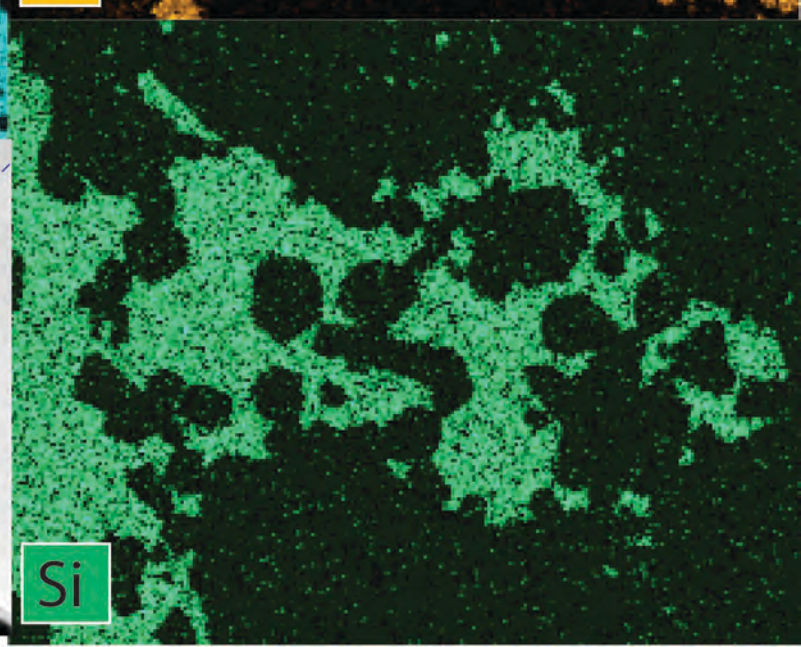

Figure 5

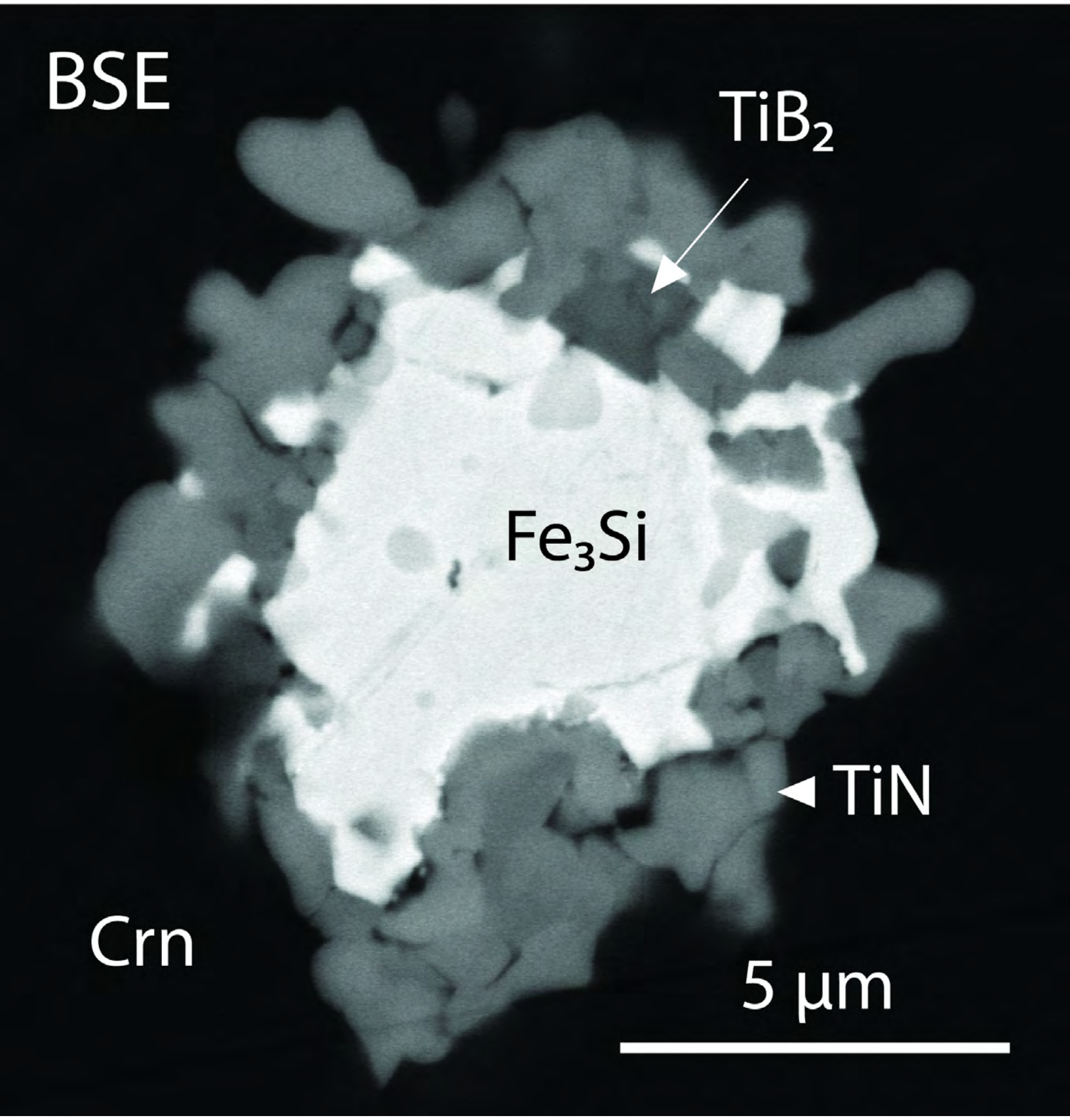

Figure 6

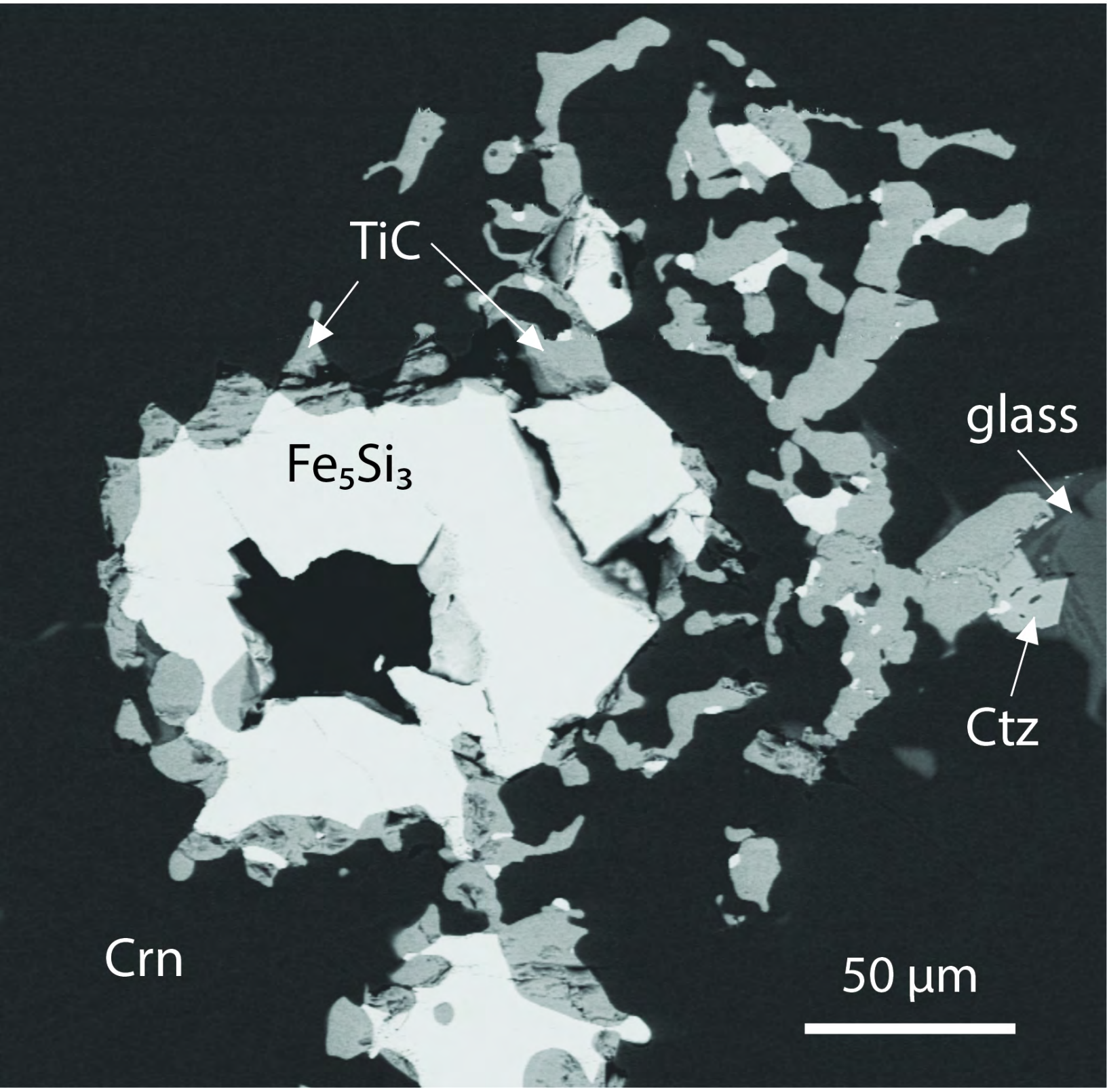

Figure 7

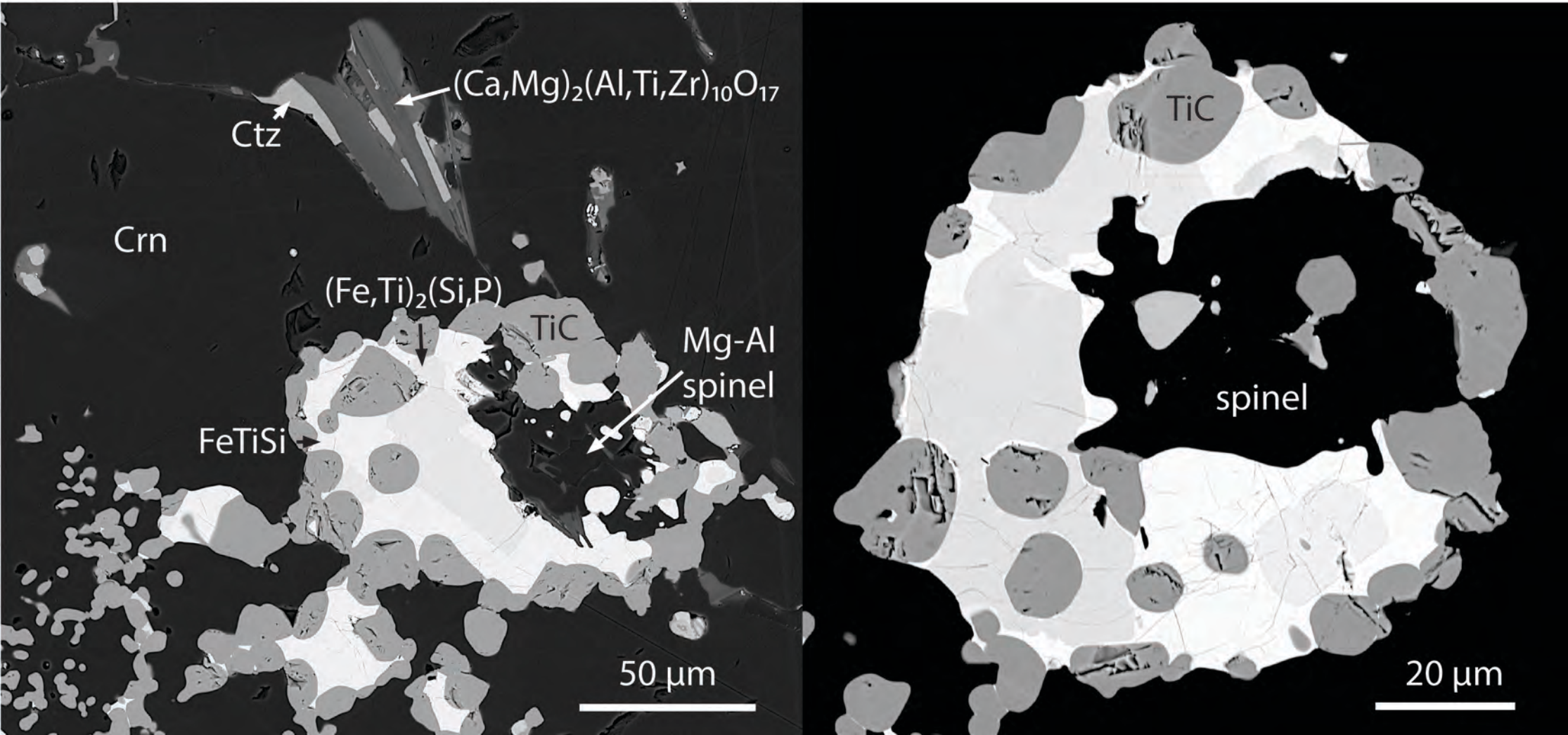
(Ca,Mg)2(Al,Ti,Zr)10O17
Ctz
Crn
(Fe,Ti)2(Si,P)
TiC
Mg-Al
spinel
FeTiSi
50 µm
TiC
spinel
20 µm

Figure 8

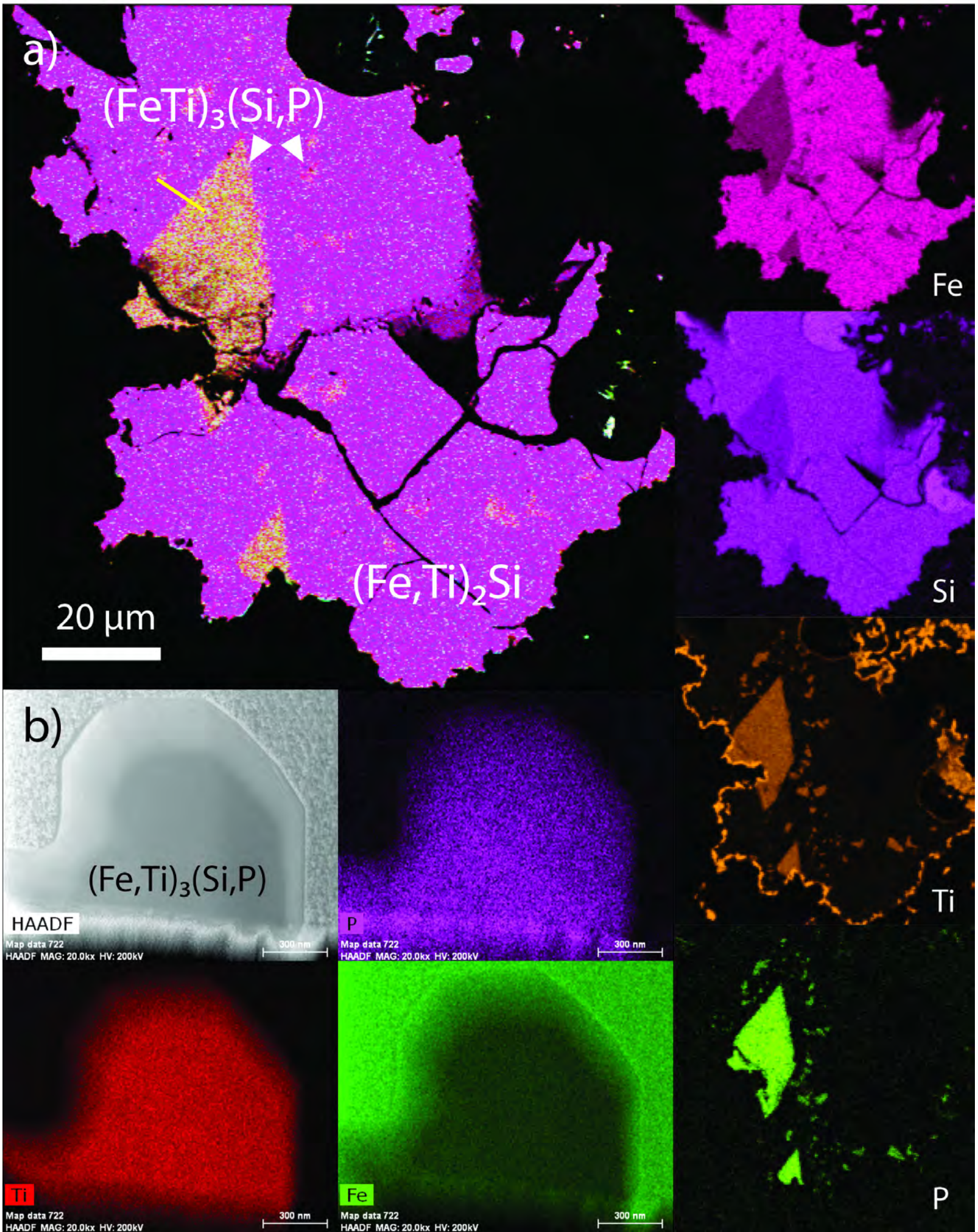
a)
(FeTi)3(Si,P)
(Fe,Ti)2Si
20 µm
Fe
Si
Ti
P
b)
(Fe,Ti)3(Si,P)
HAADF
Map data 722
HAADF MAG: 20.0kx HV: 200kV
300 nm
P
Map data 722
HAADF MAG: 20.0kx HV: 200kV
300 nm
Ti
Map data 722
HAADF MAG: 20.0kx HV: 200kV
300 nm
Fe
Map data 722
HAADF MAG: 20.0kx HV: 200kV
300 nm

Figure 9

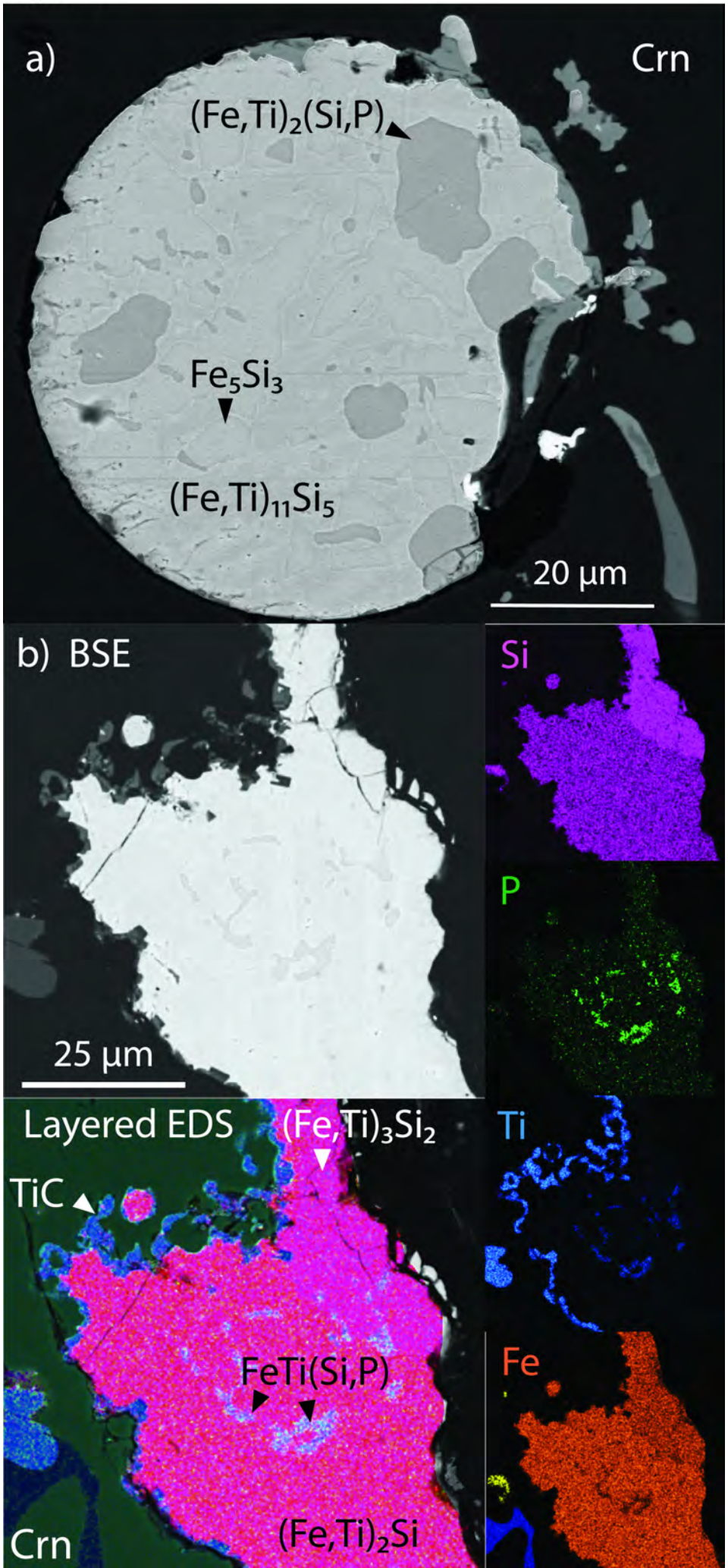
a)
Crn
(Fe,Ti)2(Si,P)
Fe5Si3
(Fe,Ti)11Si5
20 µm
b) BSE
25 µm
Si
P
Layered EDS
(Fe,Ti)3Si2
TiC
Ti
FeTi(Si,P)
Fe
Crn
(Fe,Ti)2Si

Figure 10

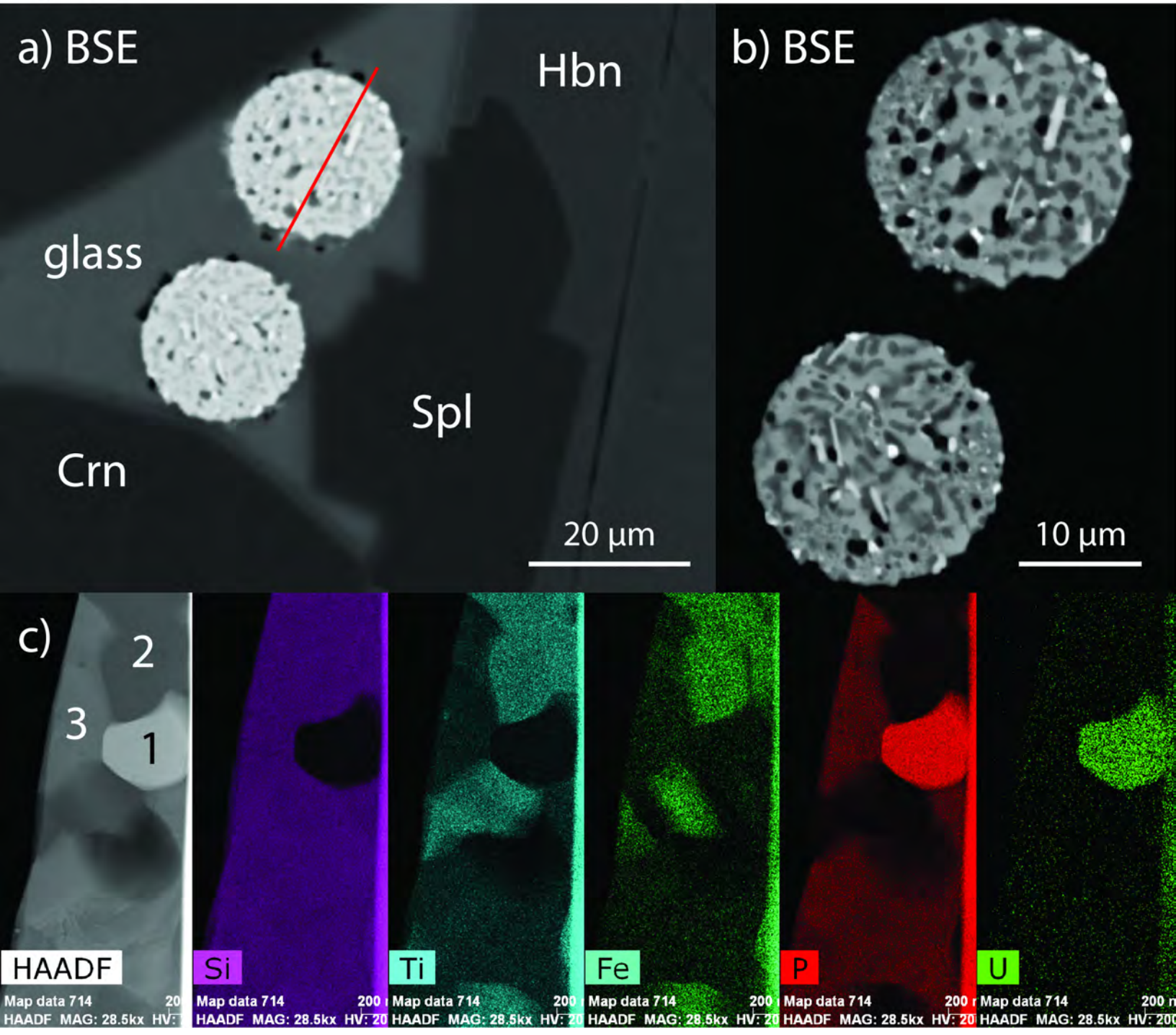
a) BSE
Hbn
glass
Spl
Crn
20 µm
b) BSE
10 µm
c)
2
3
1
HAADF
Si
Ti
Fe
P
U
Map data 714
HAADF MAG: 28.5kx HV:

Figure 11

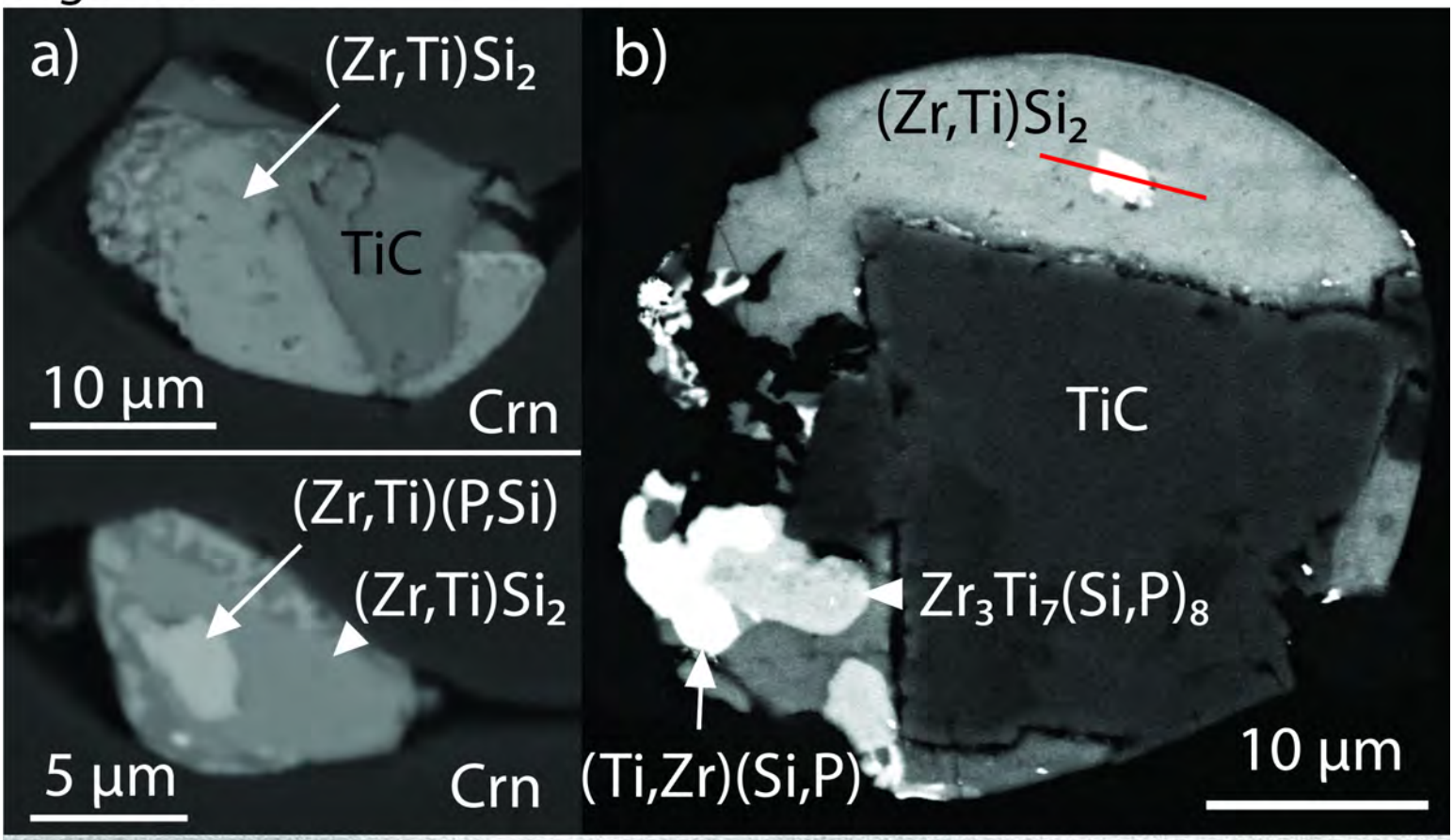
a)
(Zr,Ti)Si2
TiC
10 µm
Crn
(Zr,Ti)(P,Si)
(Zr,Ti)Si2
5 µm
Crn
b)
(Zr,Ti)Si2
TiC
Zr3Ti7(Si,P)8
(Ti,Zr)(Si,P)
10 µm

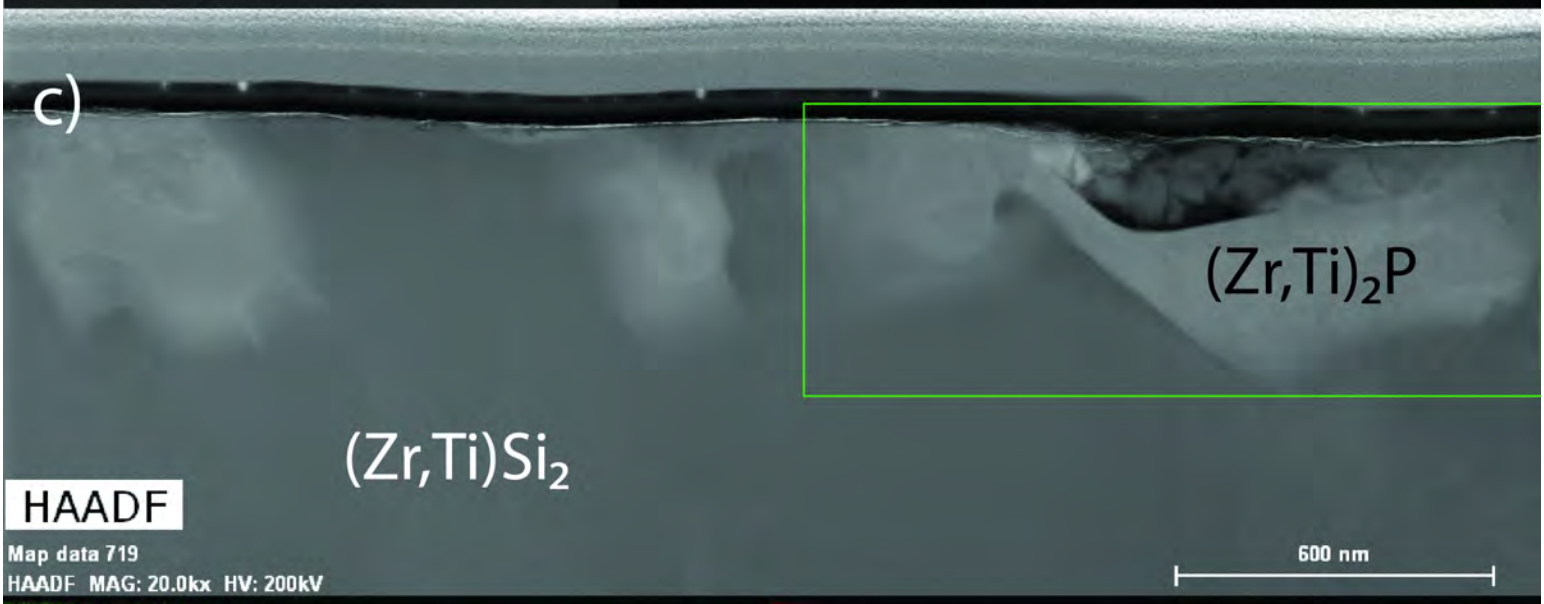
c)
(Zr,Ti)2P
(Zr,Ti)Si2
HAADF
Map data 719
HAADF MAG: 20.0kx HV: 200kV
600 nm

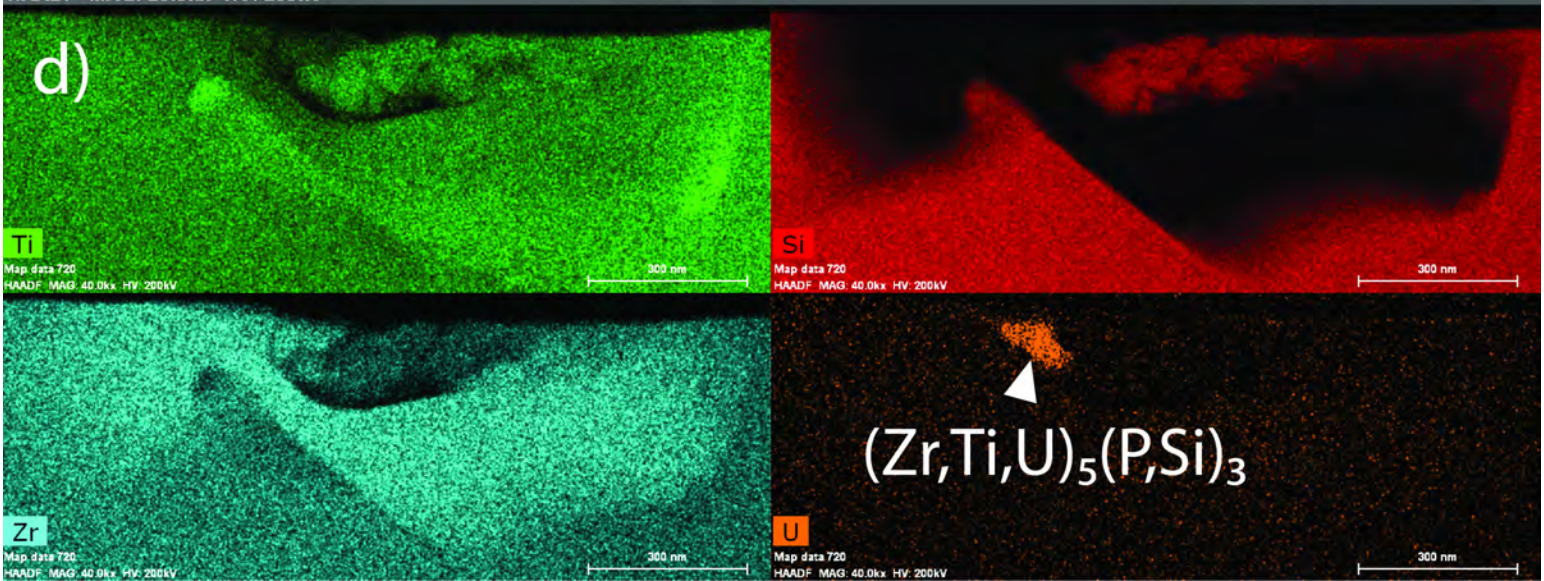
d)
Ti
Map data 720
HAADF MAG: 40.0kx HV: 200kV
300 nm
Si
Map data 720
HAADF MAG: 40.0kx HV: 200kV
300 nm
Zr
Map data 720
HAADF MAG: 40.0kx HV: 200kV
300 nm
(Zr,Ti,U)5(P,Si)3
U
Map data 720
HAADF MAG: 40.0kx HV: 200kV
300 nm

Figure 12

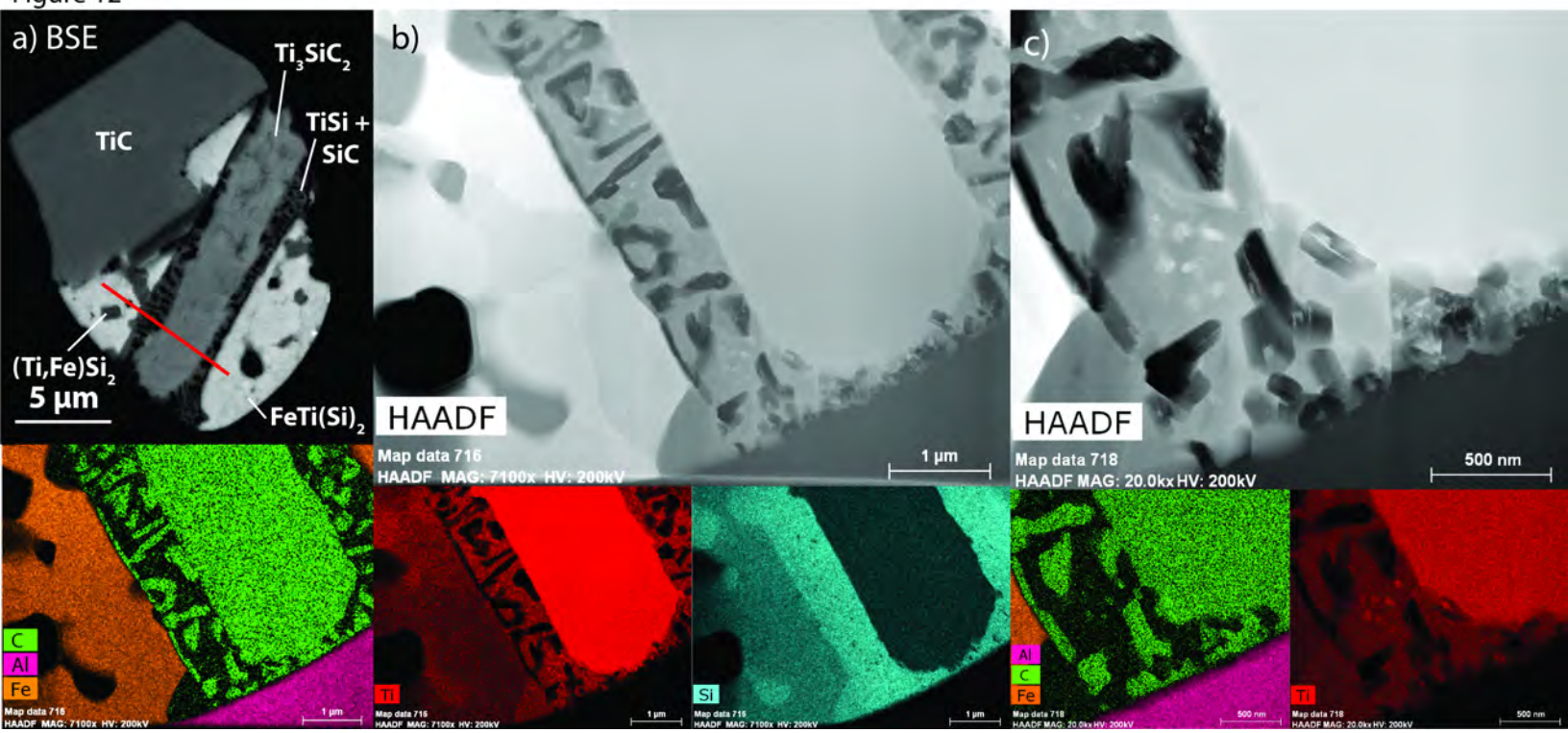
a) BSE
Ti3SiC2
TiC
TiSi +
SiC
(Ti,Fe)Si2
5 µm
FeTi(Si)2
b)
HAADF
Map data 716
HAADF MAG: 7100x HV: 200kV
1 µm
c)
HAADF
Map data 718
HAADF MAG: 20.0kx HV: 200kV
500 nm
C
Al
Fe
Ti
Si
Al
C
Fe
Ti

Figure 13

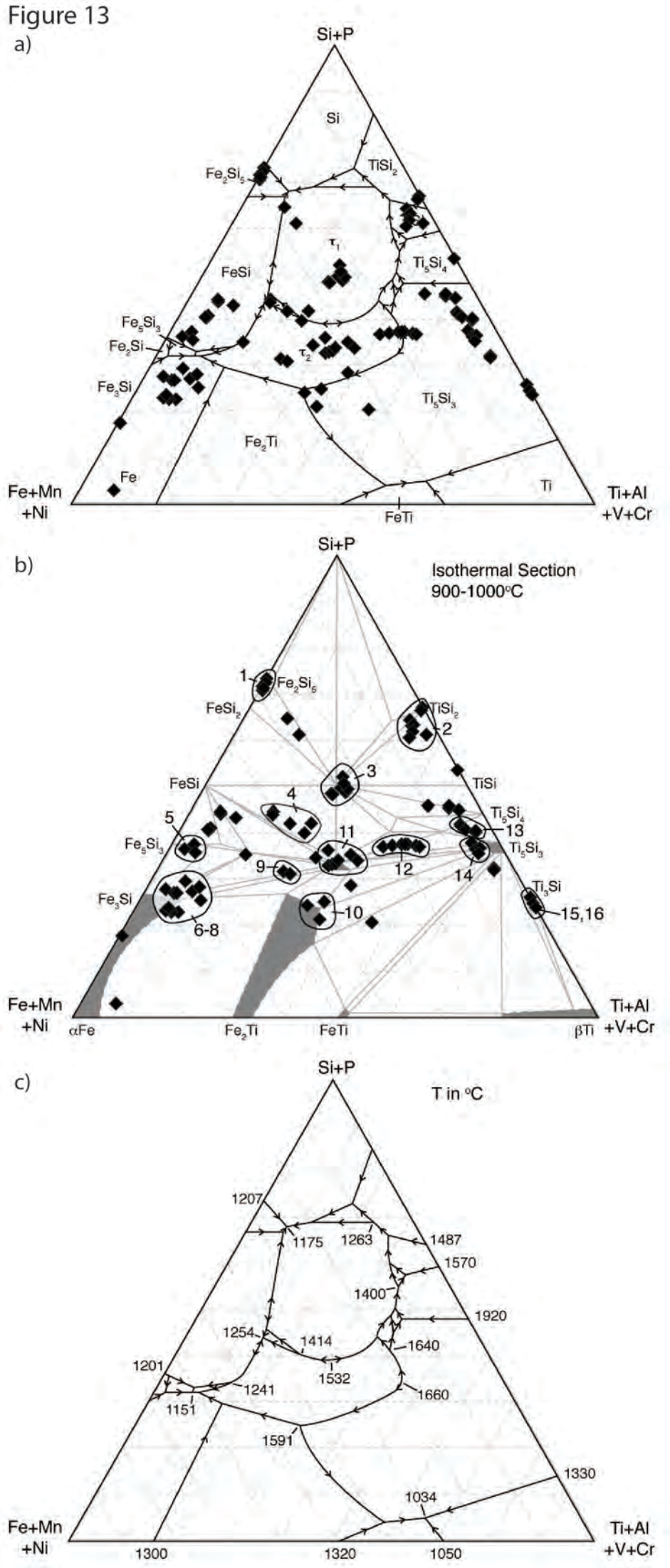
a)
Si+P
Si
TiSi2
Fe2Si5
τ1
FeSi
Ti5Si4
Fe5Si3
Fe2Si
τ2
Fe3Si
Ti5Si3
Fe2Ti
Fe
Ti
Fe+Mn
+Ni
FeTi
Ti+Al
+V+Cr
b)
Si+P
Isothermal Section
900-1000°C
1
Fe2Si5
FeSi2
TiSi2
2
3
FeSi
TiSi
4
5
Ti5Si4
13
11
Fe5Si3
Ti5Si3
9
12
14
Ti3Si
Fe3Si
10
15,16
6-8
Fe+Mn
+Ni
αFe
Fe2Ti
FeTi
βTi
Ti+Al
+V+Cr
c)
Si+P
T in °C
1207
1175
1263
1487
1570
1400
1920
1254
1414
1640
1201
1532
1241
1660
1151
1591
1330
1034
Fe+Mn
+Ni
1300
1320
1050
Ti+Al
+V+Cr

Figure 14

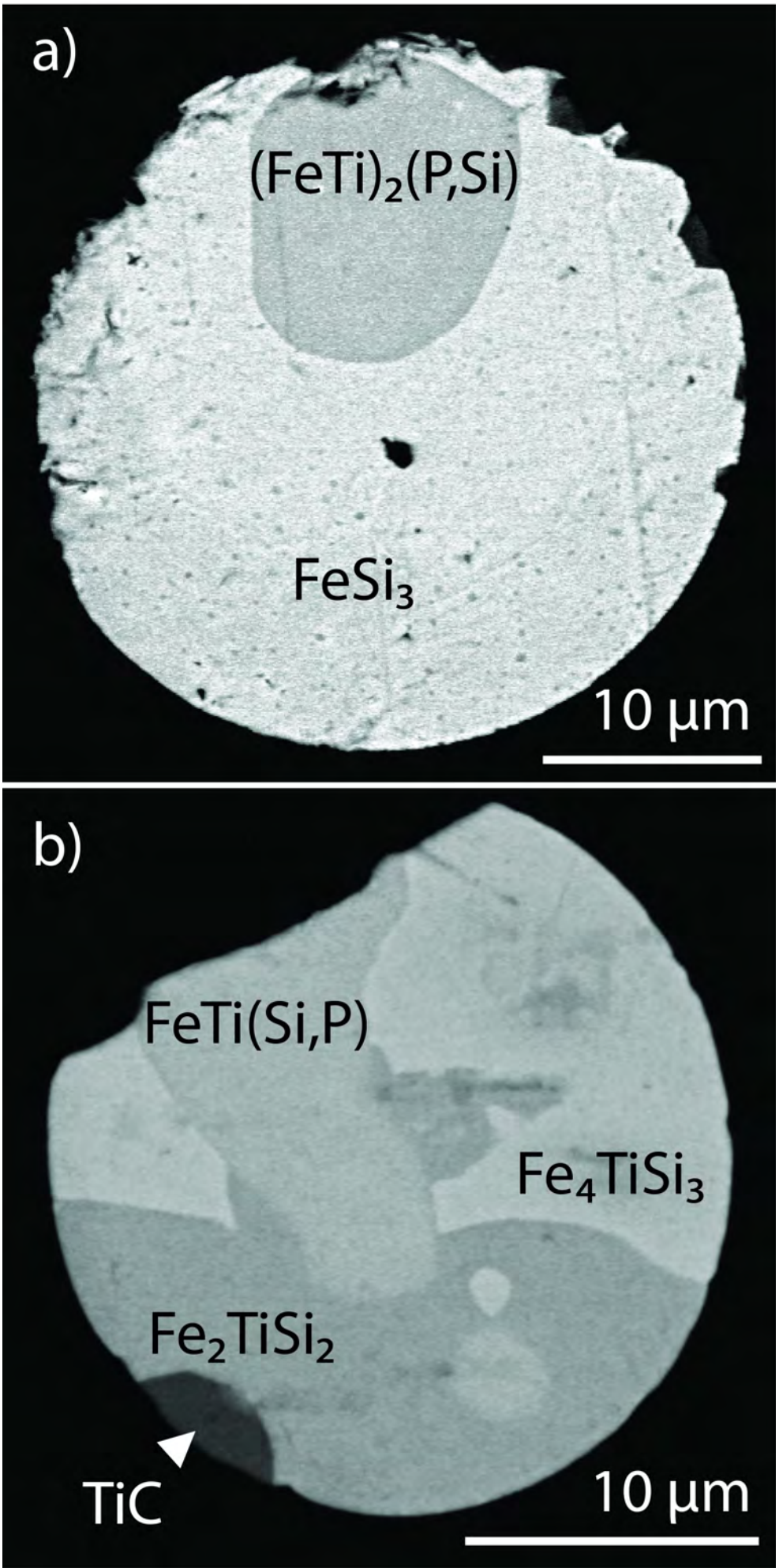

Figure 15

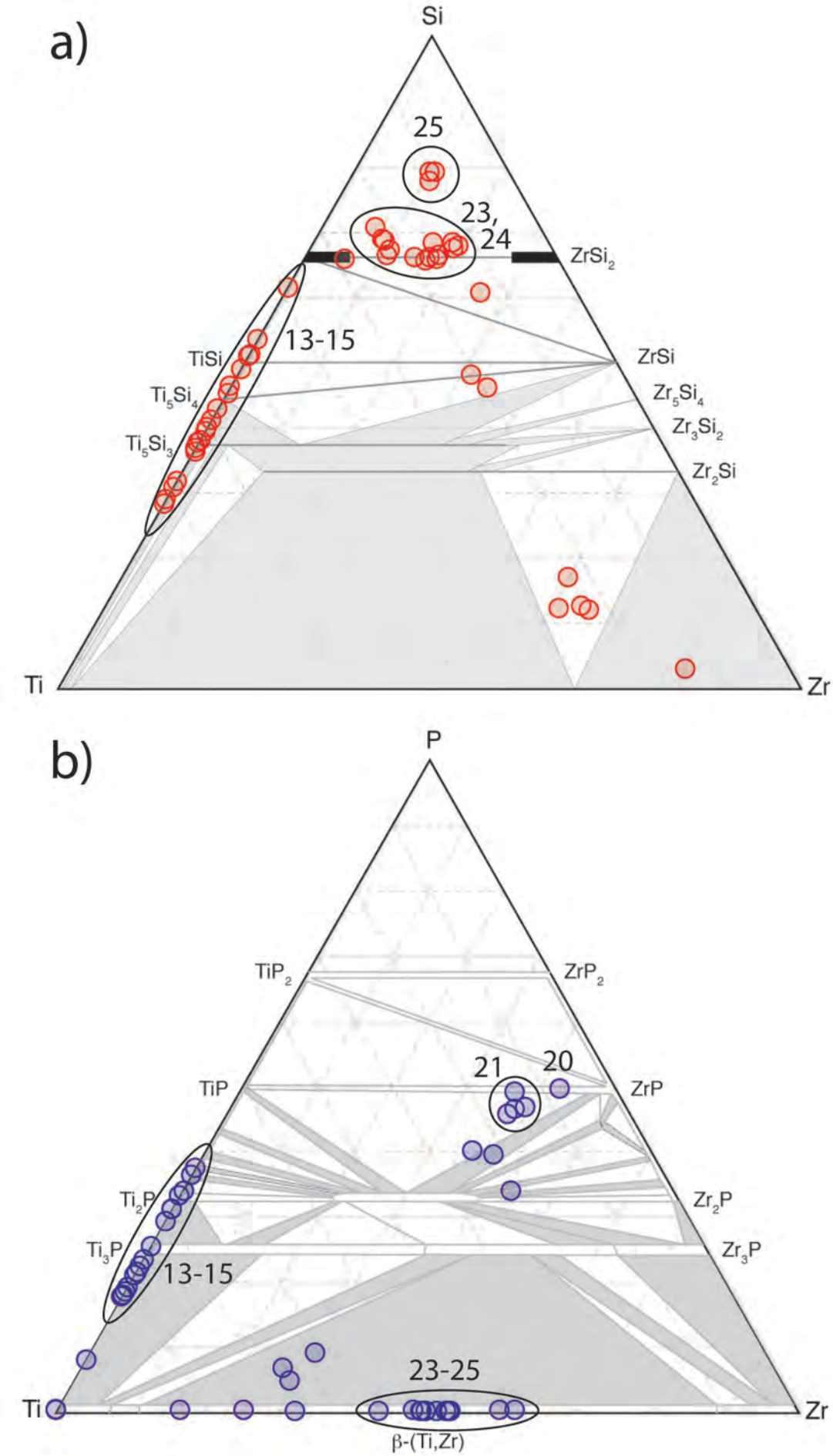
a)
Si
25
23,
24
ZrSi2
13-15
TiSi
Ti5Si4
Ti5Si3
ZrSi
Zr5Si4
Zr3Si2
Zr2Si
Ti
Zr
b)
P
TiP2
ZrP2
21
20
TiP
ZrP
Ti2P
Ti3P
13-15
Zr2P
Zr3P
23-25
Ti
Zr
β-(Ti,Zr)

Figure 16

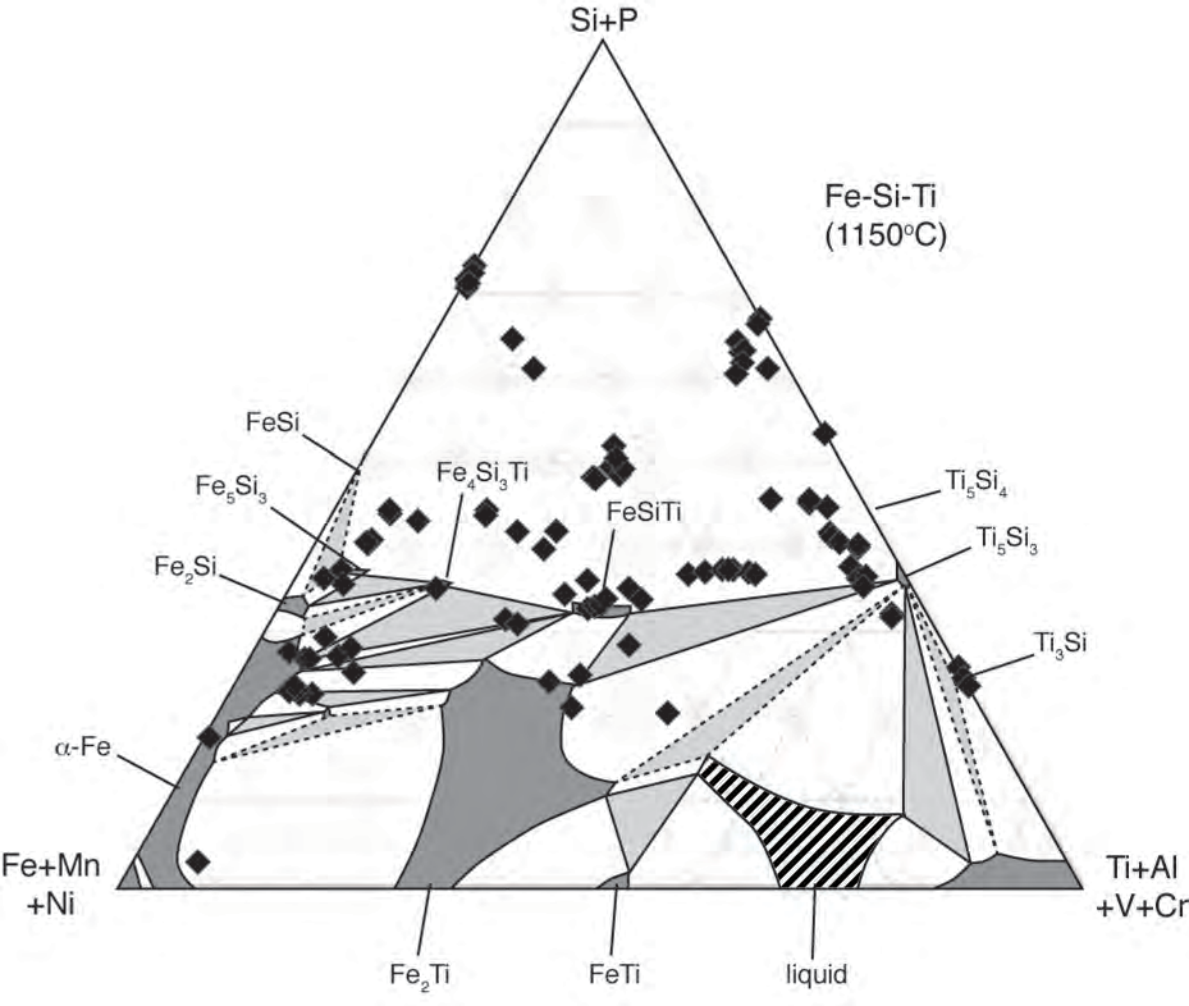
Si+P
Fe-Si-Ti
(1150°C)
FeSi
Fe5Si3
Fe4Si3Ti
FeSiTi
Ti5Si4
Ti5Si3
Fe2Si
Ti3Si
α-Fe
Fe+Mn
+Ni
Ti+Al
+V+Cr
Fe2Ti
FeTi
liquid

Figure 17

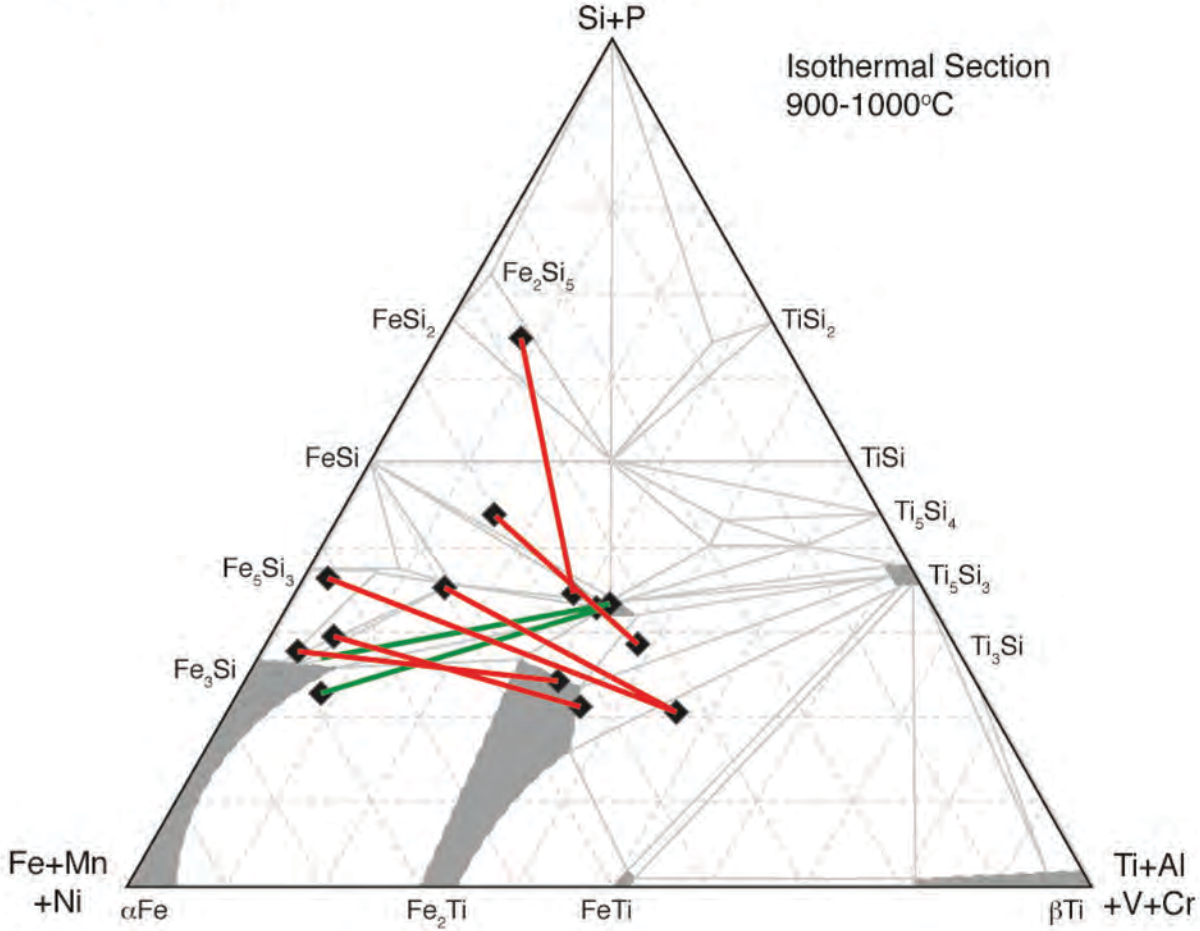
Si+P
Isothermal Section
900-1000°C
Fe2Si5
FeSi2
TiSi2
FeSi
TiSi
Ti5Si4
Fe5Si3
Ti5Si3
Ti3Si
Fe3Si
Fe+Mn
+Ni
αFe
Fe2Ti
FeTi
βTi
Ti+Al
+V+Cr

Fig. 18

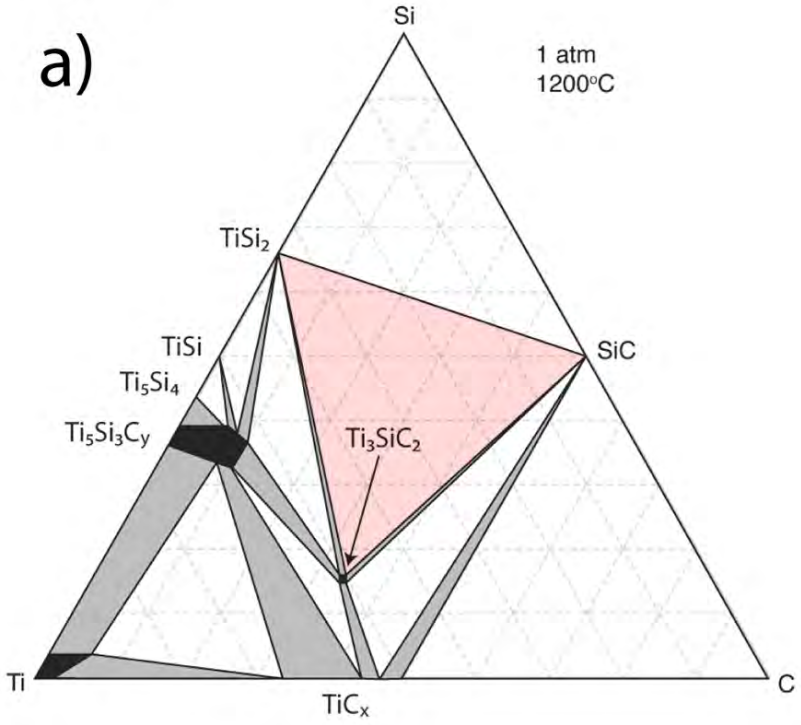
a)
Si
1 atm
1200°C
TiSi2
TiSi
Ti5Si4
Ti5Si3Cy
Ti3SiC2
SiC
Ti
C
TiCx

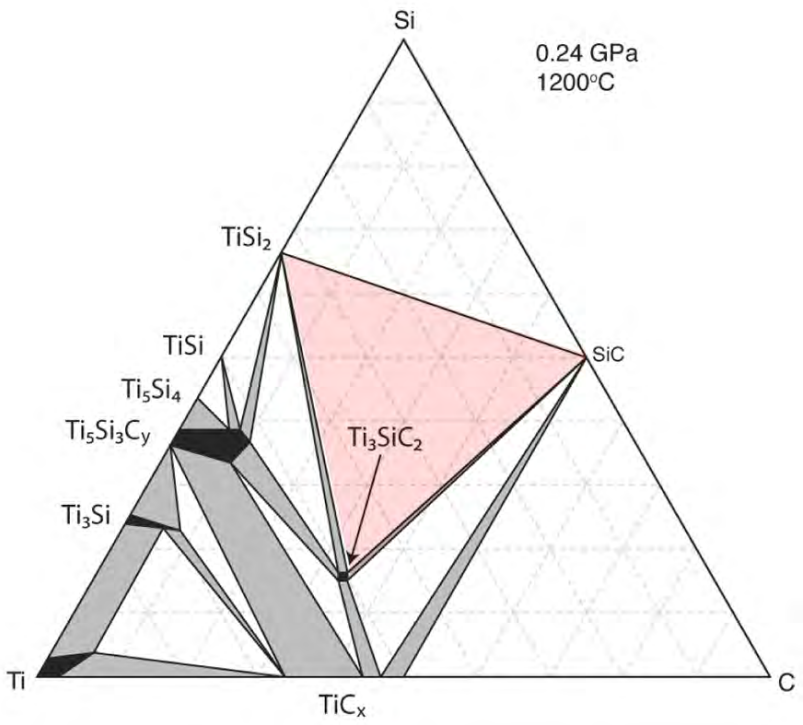
Si
0.24 GPa
1200°C
TiSi2
TiSi
Ti5Si4
Ti5Si3Cy
Ti3Si
Ti3SiC2
SiC
Ti
C
TiCx

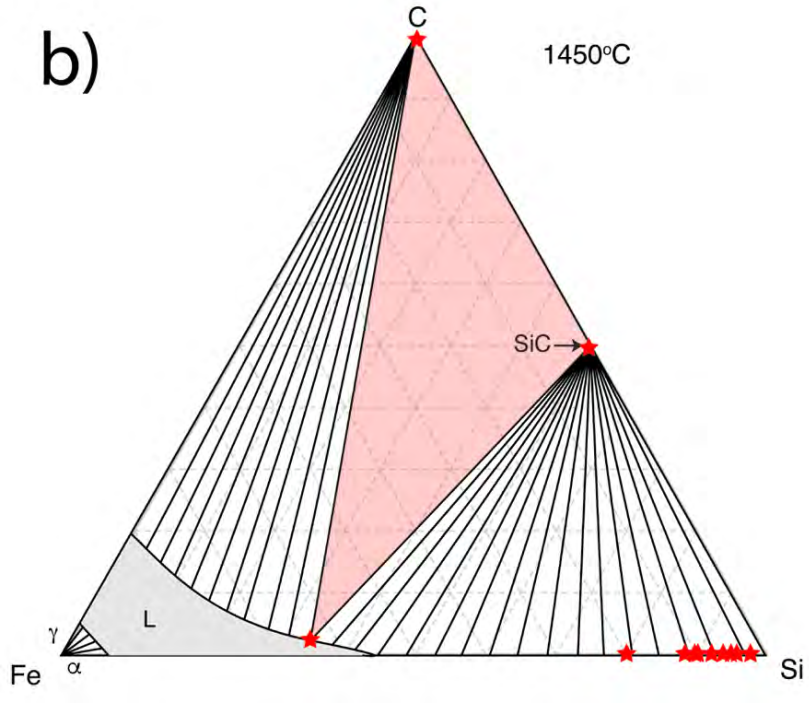
b)
C
1450°C
SiC
γ
L
α
Fe
Si

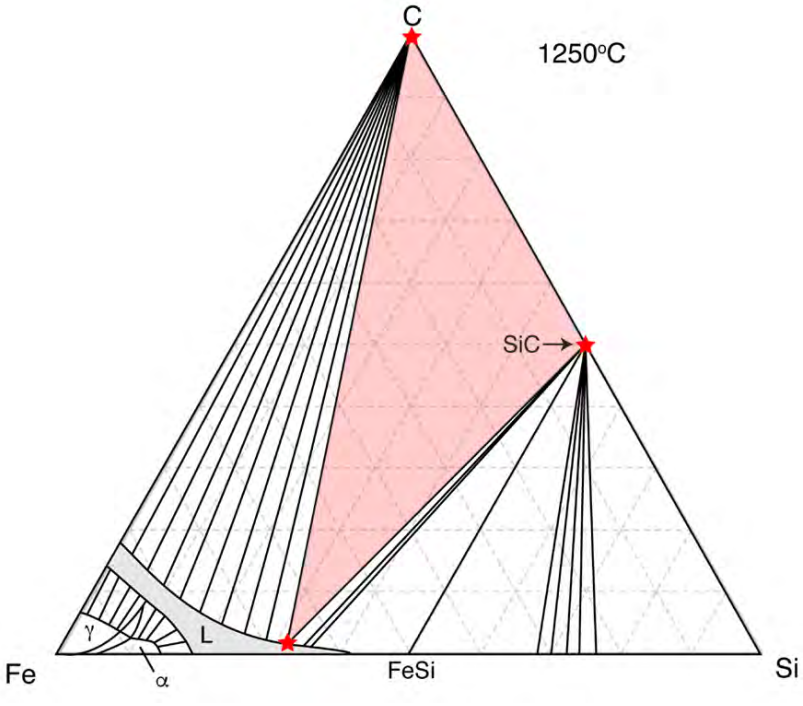
C
1250°C
SiC
γ
L
α
Fe
FeSi
Si

Figure 19

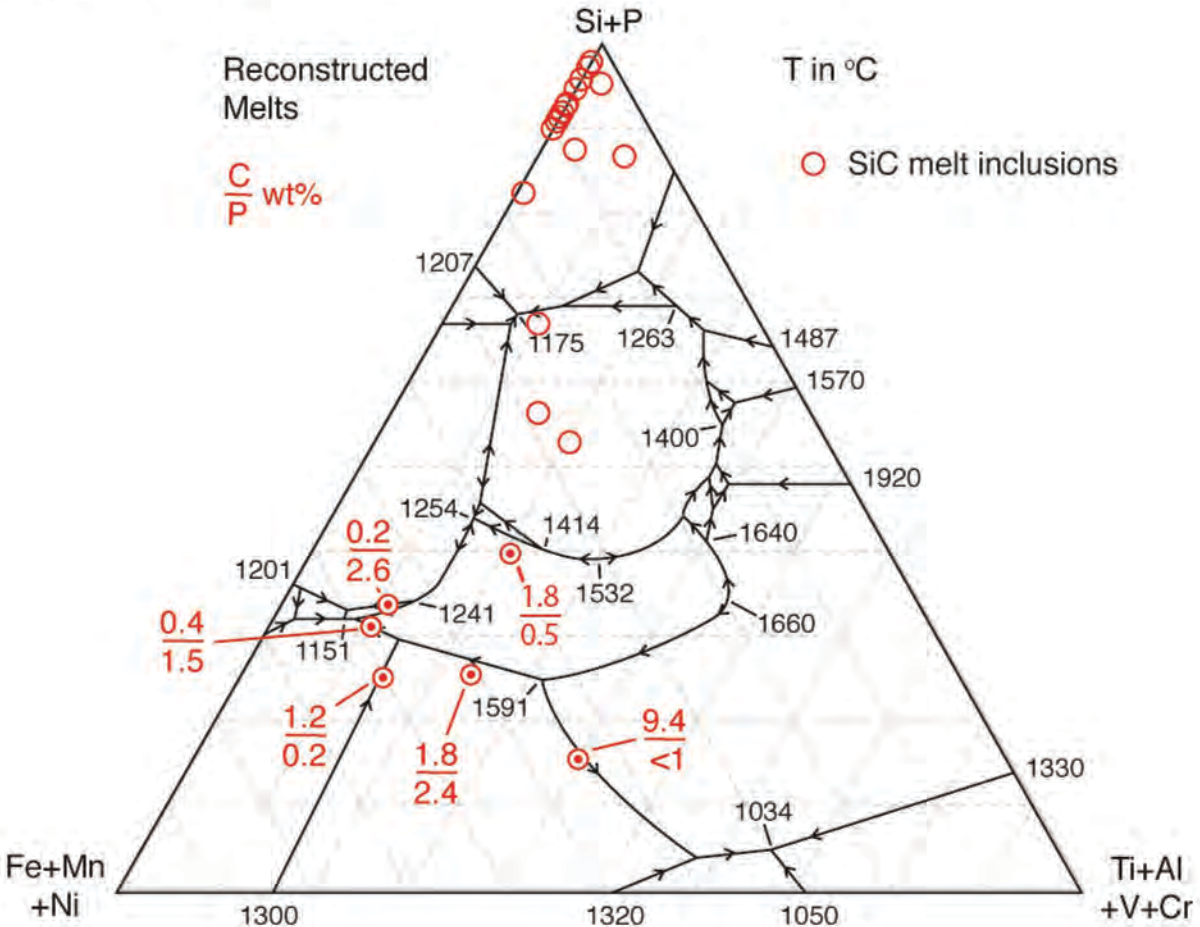
Si+P
Reconstructed Melts
C/P wt%
T in °C
SiC melt inclusions
1207
1175
1263
1487
1570
1400
1920
1254
1414
1640
1201
0.2/2.6
1241
1.8/0.5
1532
0.4/1.5
1151
1660
1.2/0.2
1591
1.8/2.4
9.4/<1
1330
1034
Fe+Mn +Ni
1300
1320
1050
Ti+Al +V+Cr

Figure 20

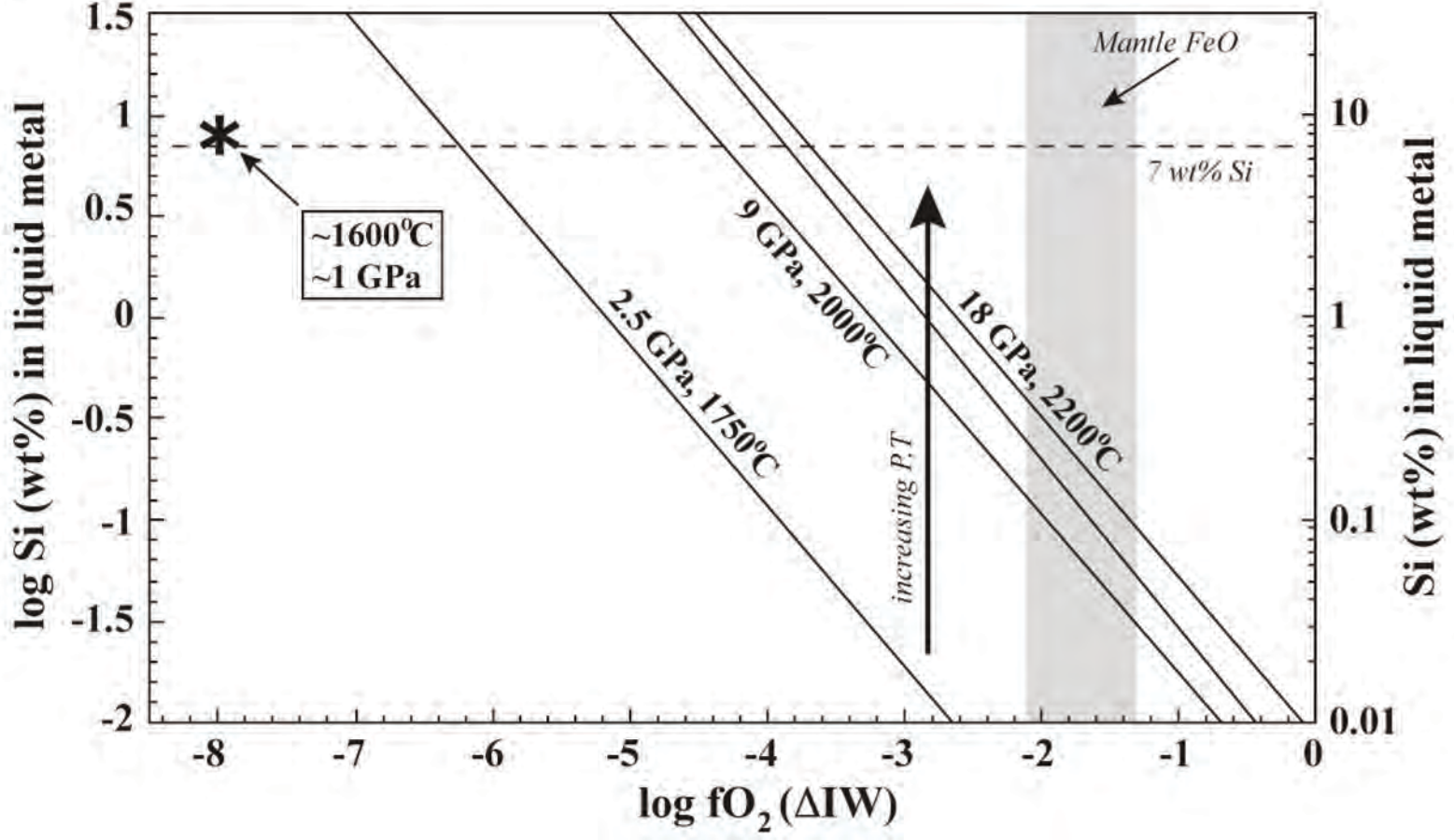
1.5
1
0.5
0
-0.5
-1
-1.5
-2
log Si (wt%) in liquid metal
10
1
0.1
0.01
Si (wt%) in liquid metal
-8
-7
-6
-5
-4
-3
-2
-1
0
log fO2 (ΔIW)
Mantle FeO
7 wt% Si
~1600°C
~1 GPa
2.5 GPa, 1750°C
9 GPa, 2000°C
18 GPa, 2200°C
increasing P,T

Figure 21

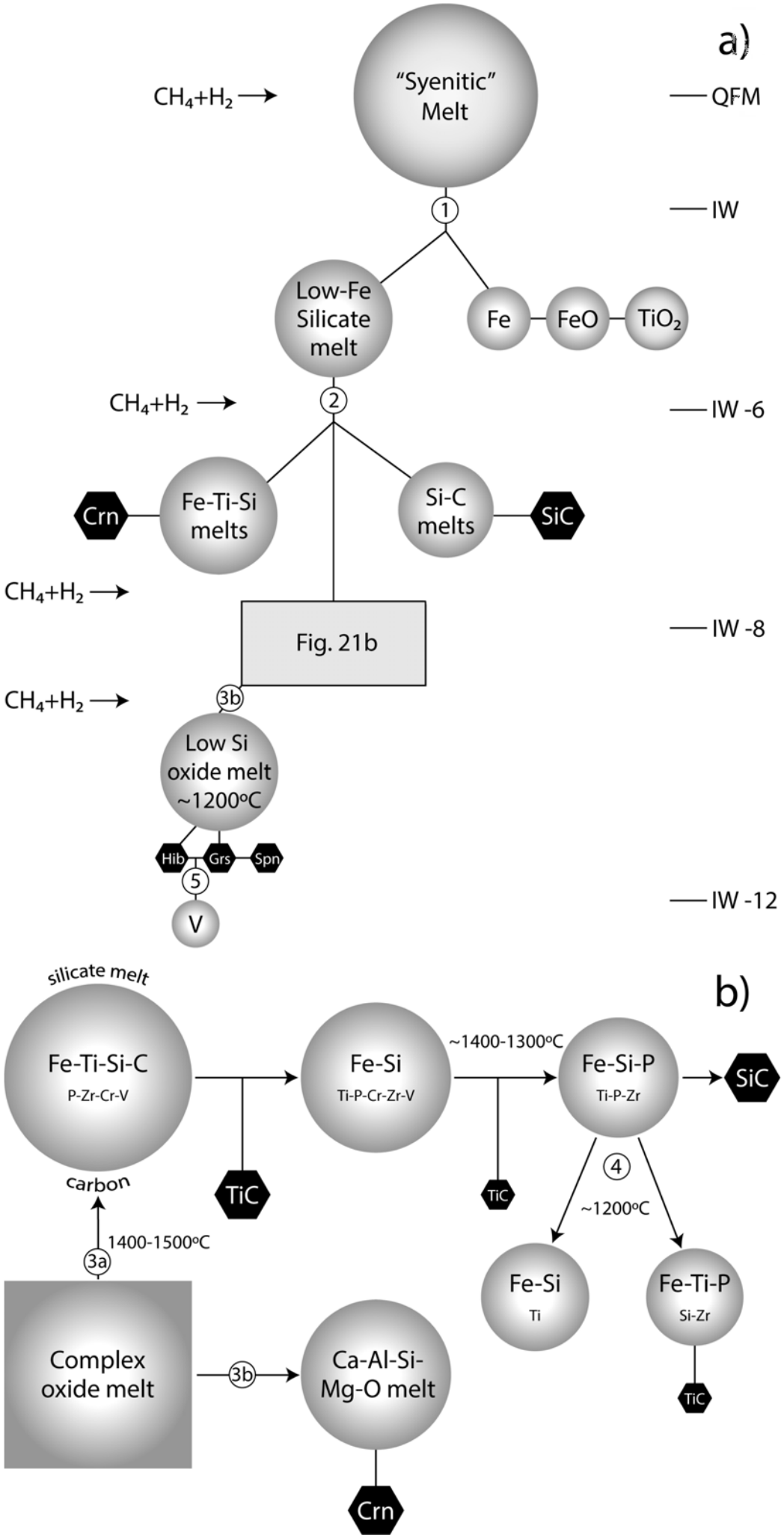
a)
CH_4+H_2
"Syenitic" Melt
QFM
1
IW
Low-Fe Silicate melt
Fe
FeO
TiO_2
CH_4+H_2
2
IW -6
Crn
Fe-Ti-Si melts
Si-C melts
SiC
CH_4+H_2
Fig. 21b
IW -8
CH_4+H_2
3b
Low Si oxide melt ~1200°C
Hib
Grs
Spn
5
V
IW -12
b)
silicate melt
Fe-Ti-Si-C
P-Zr-Cr-V
TiC
Fe-Si
Ti-P-Cr-Zr-V
~1400-1300°C
Fe-Si-P
Ti-P-Zr
SiC
TiC
4
~1200°C
carbon
1400-1500°C
3a
Fe-Si
Ti
Fe-Ti-P
Si-Zr
TiC
Complex oxide melt
3b
Ca-Al-Si-Mg-O melt
Crn